Final Technical Report

Optimization of Heat Treatments on Stainless Steel Castings for Improved Corrosion Resistance and Mechanical Properties

DOE Award No: DE-FC36-04GO14230

November 1, 2004 – June 1, 2012

John N. DuPont, (610)-758-4270, JND1@lehigh.edu – Principal Investigator

Jeffrey D. Farren, (610)-758-4270, JDF3@lehigh.edu – Author

Andrew W. Stockdale, (610)-758-4270, AWS3@lehigh.edu – Author

Brett M. Leister, (610)-758-4270, BML204@lehigh.edu – Author

Department of Materials Science and Engineering

Lehigh University

5 East Packer Avenue

Bethlehem, PA 18015

June 30, 2012

Acknowledgement: This report is based upon work supported by the U.S. Department of Energy under Award No. DE-FC36-04GO14230

Disclaimer: Any findings, opinions, and conclusions or recommendations expressed in this report are those of the authors and do not necessarily reflect the view of the Department of Energy.

Proprietary Data Notice: None in report.

Table of Contents

List of Acronyms

ASTM	American Society for Testing and Materials
CPT	Critical Pitting Temperature
DAS	Dendrite Arm Spacing
EBSD	Electron Back-scatter Diffraction
EPMA	Electron Probe Microanalysis
FIB	Focused Ion Beam
GTAW	Gas Tungsten Arc Welding
ICP	Inductively Coupled Plasma
LOM	Light Optical Microscopy
MAD	Mean Angular Deviation
WDS	Wavelength Dispersive Spectroscopy
XEDS	X-ray Energy Dispersive Spectroscopy

List of Tables

List of Figures

Executive Summary

It is commonly believed that high alloy castings have inferior corrosion resistance to their wrought counterparts as a result of the increased amount of microsegregation remaining in the as-cast structure. Homogenization and dissolution heat treatments are often utilized to reduce or eliminate the residual microsegregation and dissolve the secondary phases. Detailed electron probe microanalysis (EPMA) and light optical microscopy (LOM) were utilized to correlate the amount of homogenization and dissolution present after various thermal treatments with calculated values and with the resultant corrosion resistance of the alloys.

The influence of heat treatment time and temperature on the homogenization and dissolution kinetics were investigated using stainless steel alloys CN3MN and CK3MCuN. Autogenous welds were placed on the surface of the as-cast samples to determine the significance of the structural scale. Volume fraction measurements and EPMA confirm that enhanced homogenization and dissolution kinetics are achieved in the autogenous welds when compared to the cast structures due to the reduced dendrite arm spacing (DAS). In both alloys, near-complete homogenization and dissolution is achieved in the autogenous welds at 1150 °C after only one hour due to the reduced DAS. The cast materials on the other hand, require a four hour heat treatment at 1205 °C to achieve comparable levels of homogenization and dissolution. Finally, it was demonstrated that the corrosion resistance of alloys CN3MN and CK3MCuN can be improved to match the corrosion resistance of their wrought counterparts.

The influence of heat treatment time and temperature on the impact toughness and corrosion reistance of cast stainless steel alloys CF-3, CF-3M, CF-8, and CF-8M was also investigated. The impact toughness increased with increasing temperature and time due to a combination of spherodization and spherodization followed by dissolution of the continuous ferrite network in the castings. Heat treatment was observed to increase corrosion resistance in the CF-3-HF and CF-8-HF alloys, but corrosion testing in the other alloys did not result in a clear trend being formed with respect to the heat treatment. Corrosion began at the interface of the ferrite and austenite phases and continuously progressed through the ferrite network.

Introduction

Superaustenitic stainless steel castings are used in a variety of environments where good corrosion resistance and toughness are required. Mo is a key alloying element that is added for improved resistance to crevice and pitting corrosion. Recent work has suggested that Mo, in combination with N, promotes selective dissolution of iron at the surface and leads to Cr enrichment beneath the passive film,

thus increasing corrosion resistance [1]. A nitride layer has also been detected at the film-metal interface along with a ferrous molybdate ($FeMoO_4$) layer in the outer regions of the passive film. These phases have been proposed to provide secondary kinetic barriers for further enhancement in corrosion performance. In wrought alloys, where the Mo is homogeneously distributed, the protective surface film that develops provides excellent pitting and crevice corrosion resistance [2]. However, the stability of the protective film is adversely affected in regions of Mo depletion that is commonly observed in castings and welds. [3]

Mo segregates to the liquid during solidification because of the relatively low solubility of Mo in austenite. The inability of Mo to diffuse down the concentration gradient as a result of the low diffusivity of Mo in austenite leaves the dendrite cores depleted in Mo [4]. As a result, castings and welds are susceptible to preferential corrosive attack at the dendrite cores [3]. The Mo enrichment in the liquid also leads to the formation of brittle interdendritic σ phase that has a deleterious influence on impact toughness [5]. These deleterious effects potentially can be eliminated with a post-casting heat treatment designed to homogenize the Mo and dissolve the interdendritic σ phase. However, the influence of heat treatment time and temperature on the homogenization and dissolution behavior in these alloys has not yet been investigated. In addition, no reports are available that describe the influence of heat treatment on the corrosion behavior. The objective of this research was to determine the influence of heat treatment time and temperature on the microstructure and concomitant corrosion resistance of cast superaustenitic stainless steel alloys CN3MN and CK3MCuN. These alloys were selected because of their relatively high Mo concentrations and industrial experience that indicates significant differences in the corrosion performance of cast and counterpart wrought alloys. The results of this work are useful for designing industrial heat treatments that can be used to restore the corrosion resistance of cast alloys to a level similar to that of their wrought counterparts.

Chapter 1: Heat Treatment Optimization of High Alloy Stainless Steel Castings and Welds

1.1 Background

1.1.1 Corrosion Test Practices

Various ASTM documents describe laboratory test methods for determining the relative corrosion resistance of engineering alloys. These test methods were developed primarily to determine the relative corrosion resistance of engineering alloys within a single laboratory, although reasonable inter-laboratory reproducibility has been demonstrated. The results of the test method are often used as a material acceptance criteria. However, the tests were not originally developed for this purpose, and control of important test variables may not be described in enough detail to provide the high level of reproducibility needed for use as a material acceptance criteria. As a result, it is possible for two different casting vendors to offer an alloy with equivalent corrosion performance, but obtain different acceptance results due to variations within the test method. This can potentially create situations in which a vendor provides an "acceptable" casting that does not provide the level of corrosion resistance required for the intended application. Alternatively, a vendor may be excluded from an application in which the casting does provide the required level of corrosion resistance, but failed to meet the acceptance criteria due only to variability in the test procedure. Thus, the influence of ASTM corrosion test variables requires further investigation in order to determine if the reproducibility of these tests needs to be improved for alloy acceptance purposes.

ASTM G48-03 – Methods A & E

The purpose of ASTM G48 is to provide methods for determining the resistance of stainless steels and related alloys to pitting and crevice corrosion during exposure to oxidizing chloride bearing environments. Method A is a basic test practice designed to determine the relative pitting resistance of stainless steels and nickel-based alloys. Method E of ASTM G48 was designed specifically to determine the critical pitting temperature (CPT) for various types of stainless steels. Method E yields a ranking of engineering alloys by their minimum temperature to cause initiation of pitting corrosion of stainless steels in standard ferric chloride solutions. The use of ferric chloride is appropriate because it simulates the environment within a pit or crevice encountered by ferrous alloys in chloride bearing environments and because the relative performance of these alloys exhibits strong correlation to their performance in real environments such as ambient seawater.

Despite the usefulness of this standard for providing a ranking of engineering alloys in chloride containing environments, it is not known whether the results obtained using these methods are uniform across different laboratories due to potential deviations of test variables permitted within the specification. For instance, section 7 states "A test specimen 25 mm by 50 mm is recommended as a standard size, although various shapes and sizes can be tested by this method." The allowance of various shapes and sizes may be significant if it is determined that sample dimensions has a significant effect on the test results. There are several other instances where significant test variability is possible including polishing technique, surface finish, and cleaning procedure.

ASTM E 1169 – 02: Standard Guide for Conducting Ruggedness Tests

The purpose of ASTM E 1169 is to identify the experimental variables in a given test method which most strongly influence the results generated by the test. Determination of the influence of each individual experimental factor allows judgments to be made about how closely each variable needs to be controlled so that it does not falsely impact the results of the experiment. Ruggedness tests are conducted using a series of controlled experiments in which test variables are systematically varied in order to determine the effect of such variations. This methodology will be applied to the ASTM G48 test method to determine if tighter experimental control of testing variables will improve its use as a material acceptance criterion across different laboratories.

Influence of Test Variables on Test Results

There are a wide range of test variables that can possibly influence the results obtained using the G48 test method including – test time, test temperature, sample dimensions, surface preparation, mass transport behavior, bulk solution environment, bulk solution composition, and sample geometry. Several of these topics will be discussed in detail in the following sections.

Sample Surface Preparation

A wide variety of surface preparation procedures have been developed to increase the corrosion performance of many types of materials. These surface preparation procedures, which include grinding, anodic polishing, and pickling, combine with alloy composition to determine the passive film characteristics for a particular alloy. For stainless steels, the critical importance of surface preparation and passive film characteristics are manifested in different ways for pitting and crevice corrosion. The

improvement in pitting corrosion resistance provided by different surface treatments is primarily associated with the removal of surface imperfections and inhomogeneities and only secondarily with the enrichment of chromium in the passive film. Conversely, surface treatments improve the crevice corrosion resistance of stainless materials primarily through a heavy enrichment of chromium in the passive film with only a minor improvement stemming from the removal of surface imperfections [6].

Electrochemical Reactions

The work of Oldfield et al. [7] clearly demonstrates that electrochemical reactions, namely oxygen reduction and hydrogen evolution, play a very important role in determining the rate and extent of corrosion propagation. Of the two electrochemical reactions, oxygen reduction plays a more significant role because it is strongly dependent upon the corrosion potential that develops in the test solution. In natural seawater a very high corrosion potential catalyzes the oxygen reduction reaction and therefore leads to rapid, diffusion-controlled corrosion propagation. On the other hand, synthetic sea water and analogous test solutions have comparatively low corrosion potentials that result in slow, activation-controlled corrosion propagation [7].

Bulk Solution Environment

The factors contributing to bulk solution environment include solution temperature, solution flow rate, and overall volume of the solution. The effect of solution temperature as related to crevice corrosion initiation, although this will be relevant to pitting corrosion initiation as well, is described in Table i for two stainless steel alloys [8,9]. Although there is no significant difference in the time to breakdown across alloys, there is a very large and noticeable increase in the time to crevice initiation when the temperature is decreased. The primary reason for this increase in time to crevice initiation is due to increased passive film stability with decreasing temperature. Therefore, at higher temperatures, the passive film breaks down more easily which leads to more rapid crevice corrosion initiation [8,9].

The influence of solution flow rate is demonstrated in Figure 1 for the same stainless steel alloys [8]. The relationship between crevice corrosion initiation and solution flow rate exhibits an interesting relationship where the time to breakdown initially decreases with increased solution velocity and then begins to increase. This behavior can be explained by a cathode limitation, which is a mass transport phenomenon caused by the low solubility of oxygen in aqueous media. The limitation is present when the solution is stagnant and begins to be eliminated as the solution velocity is increased to 0.04 m/s. After this, further increases in the solution velocity causes convection to occur inside of the crevice which, in

turn, prevents the formation of the overly aggressive solution that is typically present inside the crevice area. This leads to increased times to crevice initiation or breakdown. The behavior from 0.04 m/s upward can also be explained electrochemically because increasing the solution flow rate initiates an anodic shift in the corrosion potential which lowers the resulting current and creates a less aggressive environment, leading to increased times to breakdown [8].

The importance of volume effects on pitting and crevice corrosion is derived from the idea of spatial scaling of a corrosion test. Spatial scaling is the choice of an appropriate laboratory test size to accurately simulate a situation which is occurring in a real environment. Therefore, spatial scaling describes whether a full scale process can be simulated by a reduced scale experiment. In most cases spatial scaling is not necessary for pitting and crevice corrosion tests since the controlling mechanisms (surface imperfections, crevice gaps) occurring in real environments are only on the order of a few millimeters [10]. It is recommended in G48 however, that the ratio of specimen surface area to bulk solution volume be kept constant to increase the uniformity of the test and reduce potential sources of error.

Bulk Solution Composition

Bulk solution composition is affected by several factors which include Cl- level and pH. The combination of these and other factors determine the basic corrosivity or aggressiveness of the test solution. As shown in Figure 2, the pH of the solution strongly affects the current that develops over time. All three pH levels initially exhibit a high current, but after a few hours the current in the less acidic solutions begins to decrease whereas the most acidic solution maintains a high level of current near the maximum. The influence of chloride concentration is shown in Figure 3 and Figure 4. In both cases, as the chloride concentration increases, the depth of attack in crevice corrosion tests increases. Increasing the Cl- concentration has a strong enough effect to cause greater depths of attack to be achieved during test exposures that are significantly shorter -- 28 vs. 90 day exposure. Therefore the general trend is somewhat obvious in that increasing the aggressiveness of the solution by lowering the pH or increasing the chloride level causes elevated corrosion levels [11].

Sample Geometry

Sample geometry plays a significant role in crevice corrosion initiation and propagation. The three main factors that contribute to the geometrical dependence are the outside to inside crevice area ratio, the crevice gap, and the crevice depth.

The outside to inside crevice area ratio is the proportion of bulk surface area away from the crevice to the surface area of the crevice itself. The effect of this ratio is demonstrated in Figure 5 [8]. The data shows that at very small crevice ratios there is some cathodic limitation present which is similar to that seen at very low solution velocities. This leads to relatively high times to breakdown. As the ratio is increased the cathodic limitation is eliminated and, in turn, the times to breakdown decrease. The behavior exhibited at very high outside to inside crevice area ratios is not well understood but it is suspected that at very high ratios high current results, which then leads to the reoccurrence of the cathodic limitation that causes long times to breakdown [8].

The effect of crevice gap is shown clearly in Figure 6 [12]. The crevice gap is varied by systematically increasing the torque applied to the crevice assembly which effectively makes the gap smaller/tighter, thus leading to more aggressive testing conditions. As the torque is increased from 3 N-cm to 10 or 20 N-cm the critical crevice temperature decreases significantly. A secondary effect of increasing the torque is that it also increases the reproducibility of the test procedure. The error bars shown in Figure 6 are larger by an order of magnitude for the low torque assembly than for the high torque assembly. This result is beneficial because it increases the reproducibility in the test procedure and allows for a better assessment of the overall performance of the materials that are being tested [12].

After consideration of the above experimental factors it was determined that the variables that would be investigated include: passivation time, passivation type, surface finish, sample orientation, and the ratio of solution volume to sample area. These variables were selected for investigation based on their potential impact on the corrosion test results.

1.1.2 Heat Treatment Optimization of CN3MN and CK3MCuN

Microstructural Development

The microstructures of as-cast CN3MN and CK3MCuN exhibit the typical segregation profiles and cellular/dendritic morphologies that are seen in a number of high alloy castings as a result of non-equilibrium (i.e. Scheil) solidification and constitutional supercooling.

Scheil conditions describe “non-equilibrium solidification” or the solidification of an alloy under the assumption that there is no diffusion in the solid, complete diffusion in the liquid, no growth undercooling, and that equilibrium exists at the solid-liquid interface[13-15]. At the instant that solidification finishes, these conditions result in a cored microstructure exhibiting a minimum concentration in the dendrite core and a maximum concentration in the interdendritic region. In certain alloy systems, back-diffusion can reduce or eliminate the extent of the concentration gradients that are

present at the end of solidification. The back-diffusion potential can be assessed using the alpha parameter which is defined as:

$$\alpha_{Mo} = \frac{D_S * t_f}{L^2} \quad (1)$$

where D_S is the solute diffusivity in the solid, t_f is the solidification time, and L is half the dendrite arm spacing. When $\alpha << 1$, back-diffusion is insignificant and the cored microstructure that existed at the end of solidification will be retained down to room temperature. Therefore, in order to calculate the alpha parameter and determine the importance of solid state diffusion during solidification, appropriate values need to be obtained for each of these variables. Solidification begins when the temperature of the liquid drops below the liquidus temperature and does not end until all liquid has solidified. This process occurs over a range of temperatures and, since diffusivity changes as a function of temperature, the diffusivity changes as well. Molybdenum is the critical element for this calculation due to its slow diffusion in austenite and its role in providing localized corrosion resistance. Therefore, in order to bound the estimate, both the high and low extremes of Mo diffusivity at the beginning (liquidus temperature) and end of solidification (eutectic temperature) were used in the calculation. The solidification time is also related to the temperature range over which the alloy solidifies. Calculated pseudo-binary phase diagrams, which will be discussed in detail later, were used to approximate the solidification temperature range of the alloys. Industrially relevant cooling rates were then combined with the solidification temperature range to determine the solidification time. For example, solidification over a 30°C temperature range at a rate of 1°C/second produces a solidification time of 30 seconds (assuming a linear cooling rate over the solidification temperature range). Diffusivity values were taken from the literature and were found to be on the order of 10^{-15} to 10^{-14} m^2/s for the solidification temperature range [16]. Finally, the dendrite arm spacing can be approximated using empirical relationships that are widely available in the literature for alloys with very similar chemistry and processing conditions. Figure 7 shows the α values for Mo in austenite as a function of cooling rate for two constant values of Ds determined at the liquidus and solidus temperatures. The alpha parameter is clearly << 1 for both instances where the high and low extremes of Mo diffusivity were used. Therefore Scheil conditions will always prevail for this solidification scenario. A list of the values used in this calculation can be seen in Table ii.

The governing equation for this solidification scenario has been described by Scheil among others and is given as:[13,15,17,18]

$$C_S^* = kC_0(1 - f_S)^{k-1} \quad (2)$$

where C_S^* is the composition of the solid at the solid/liquid interface, k is the equilibrium partition coefficient, C_0 is the initial alloy composition, and f_S is the weight fraction of the solid. At the onset of solidification $f_S = 0$ and the first solid to form is of composition kC_0 as shown in Figure 8a [18]. As solidification proceeds the liquid composition tracks along the liquids line, becoming enriched with increasing solute, leading to new solid forming with ever higher solute content then the previous solid - Figure 8b. This situation continues until the composition of the liquid is enriched with solute to C_E, which is the eutectic composition, where all the remaining liquid freezes as a terminal eutectic in the intercellular or interdendritic regions - Figure 8C. It is worth noting that, even though CN3MN and CK3MCuN are much more complex than the simple binary eutectic system that is modeled (Figure 8d) in the previous discussion, it is a reasonable first approximation that they be modeled by Scheil conditions. Susan et al. [19] have shown that multi-component alloys can be modeled as simple binaries when the following criteria are met: (1) the as-solidified microstructure contains primary γ dendrites with a eutectic type constituent where the secondary component is solute (Mo) rich; (2) the amount of eutectic increases with increasing solute content (Mo); and (3) the eutectic temperature is relatively insensitive to changes in the nominal solute content. Microstructural characterization of these alloys confirms that CN3MN and CK3MCuN do exhibit primary γ dendrites with a Mo rich sigma phase in the eutectic. Perricone et al. have shown that the eutectic fraction increases with increasing solute content and that the eutectic temperature is relatively insensitive to the nominal Mo content [20]. Therefore it is reasonable to model alloys CN3MN and CK3MCuN as simple binary systems.

Based on these observations, pseudo-binary phase diagrams were calculated using CALPHAD Thermo-Calc software with an Fe Database [21]. This software determines phase stability through free energy minimization calculations based on the published thermodynamic data that is compiled in the Fe Database. The pseudo-binary phase diagrams produced for these alloys using Thermo-Calc, Figure 9, are then used to estimate the solidification temperature range [17,18].

Homogenization Heat Treatment

Heat treatment procedures reported thus far have not been effective at improving the corrosion resistance of cast Mo bearing stainless steels to the level observed by wrought counterparts [22]. Assuming that any small changes in composition between the cast and wrought alloys are not significant and that the casting does not contain any gross defects, the difference in corrosion resistance can be attributed to one or a combination of the following factors: microsegregation, residual secondary phases that form at the end of solidification, microporosity and/or macrosegregation. Residual secondary phases can lower the corrosion resistance of an alloy by depleting the matrix of critical elements such as Cr and

Mo. Galvanic effects between the secondary phase and matrix may also exacerbate corrosion. Microsegregation and macrosegregation also can reduce the corrosion resistance by leaving areas of the alloy deficient in critical alloying elements such as Cr and Mo. Microporosity may provide sites for localized corrosion initiation.

During dendritic solidification of cast materials, solute redistribution occurs as the material solidifies, causing extensive microsegregation of the alloying elements. For typical alloys, where k (the equilibrium partition coefficient) < 1 , the segregation profile is such that the concentration of critical alloying elements is minimum at the dendrite cores and maximum in the interdendritic regions [23,24]. For molybdenum bearing austenitic stainless steels in corrosion applications, the most crucial alloying element is often Mo, which strongly segregates and leaves a composition profile characteristic of dendritic solidification. Figure 10 [4] shows an as-welded AL6XN structure and corresponding microprobe trace with the dendrite cores depleted in Mo and therefore susceptible to preferential corrosive attack. Further evidence that these segregation profiles are unavoidable comes from the fact that differential thermal analysis samples of AL6XN, which are cooled orders of magnitude slower than typical castings, still have the same dendrite core concentrations as their as-welded counterparts [4].

Segregation profiles are typically an undesirable remnant of the casting process, but they can be removed through homogenization heat treatments which promote chemical uniformity. A homogenization treatment entails exposing a casting to an elevated temperature for a prolonged period to allow segregated alloying elements to diffuse down the chemical gradient and eliminate the concentration profile [23-25]. The relative effectiveness of the homogenization heat treatment can be characterized by the index of residual segregation, which is a ratio of the amount of segregation after a homogenization treatment to the initial amount of segregation:

$$\delta_i = \frac{C_{M^\Theta} - C_{m^\Theta}}{C_M^o - C_m^o} \qquad (3)$$

where C_M^θ and C_m^θ represent the maximum and minimum concentration after a given homogenization time and C_M^0 and C_m^0 represent the maximum and minimum initial concentration [23-25]. Thus, in the as-solidified condition $\delta = 1$ and will decrease to zero for a fully homogenized alloy with no composition gradient.

Microsegregation is not the only remnant of solidification that can lead to inferior corrosion performance. Undesirable secondary phases often form during solidification that provide another site for preferential corrosive attack. These phases often form at the end of solidification as a terminal eutectic that can be found in the interdendritic regions. Therefore, in order to fully restore the corrosion resistance

of these alloys, the secondary phase needs to be dissolved and the chemical gradients need to be fully homogenized [26].

A simple diffusion model can be used to estimate the times and temperatures required to achieve varying levels of homogenization as defined by the index of residual segregation, δ_i. This diffusion model assumes a simple dendrite morphology where the dendrite arms are plates (Figure 11) with a sinusoidal composition profile across regions of maximum to minimum solute content. The initial segregation profile will then be similar to that shown in Figure 11 at t = 0. This assumed relation can be stated explicitly as:

$$\frac{C^0 - C_0}{C_M^0 - C_0} = \sin\frac{\pi x}{l_o} \tag{4}$$

where C^0 is concentration at a distance x at t = 0, C_0 is the mean alloy composition, C_M^0 is the maximum initial solute concentration, and l_0 is half the dendrite arm spacing. Using the solution of Fick's Second Law and substituting into equation 3 yields:

$$\delta_i = \exp\left[-\frac{\pi^2 D_S t}{l_0^2}\right] \tag{5}$$

This relationship is useful for estimating time-temperature combinations required to achieve the desired level of homogenization. The temperature range to be used for heat treatment of these alloys was selected using calculated phase diagrams – Figure 12. The single phase region, 1150 °C – 1315 °C, was chosen due to its potential to not only increase diffusivity and aid in homogenization, but also for its potential to completely dissolve any secondary phases present in the structure. Solute diffusivity data was acquired for the range of temperatures for use in the calculation of homogenization time [16]. The parameter L_0 ($L_0 = 0.5\lambda$) is simply measured or approximated from the empirical relationship below, which predicts dendrite arm spacing for austenitic 310 SS steel alloys with very similar compositions:

$$\lambda = 80\varepsilon^{-0.33} \tag{6}$$

where ε is the cooling rate (°C/s) and λ is the dendrite arm spacing (μm) [27]. The use of this equation is justified because the alloys of interest should have similar diffusion rates and thermal properties to the 310SS alloy for which the equation was developed. Figure 13 shows the variation in δ_i as a function of homogenization time for different temperatures. The results show that complete homogenization at 1150 °C would require approximately 4 hours while complete homogenization at 1315 °C would require only 1 hour [23]. These calculations form the basis for selection of effective heat treatment times and temperatures.

Dissolution Kinetics

Based on results from wrought alloys of similar composition, each of these alloys forms an inter-metallic sigma (σ) phase that reduces their mechanical properties and corrosion resistance [4]. Singh and Flemings [26] developed a dissolution model in which they assume an initial solute distribution across plate-like dendrite arms given as:

$$\frac{C_M - C}{C_M - C_m^0} = \cos\frac{\pi x}{2 l_0} \qquad (7)$$

where C_M is the maximum alloy content within the solid solution at the surface of the dendrite, C is the composition at a distance x, C_m^0 is the initial minimum alloy content, l_o is half the dendrite arm spacing, and x is the distance measured from the center of the dendrite arm - Figure 14. The additional assumptions of the model include: a divorced eutectic morphology with plate-like interdendritic secondary phase of constant composition Cσ, that the motion of the matrix/secondary phase boundary can be neglected, and that the rate-limiting diffusion occurs in the austenite matrix. The solution of the diffusion equation for the case of dissolution yields the following equation:[18]

$$V_t = [(V_0 + \frac{C_M - C_0}{C_\sigma}) * \exp[-\frac{\pi^2 D\, t}{4\, l_0^2}]] - \frac{C_M - C_0}{C_\sigma} \qquad (8)$$

where V_t is the volume fraction secondary phase after dissolution heat treatment time t, V_0 is the initial volume fraction secondary phase, C_M is the maximum solid solubility, C_0 is the nominal composition, C_σ is the composition of the interdendritic sigma phase, and D is the diffusivity of the solute (Mo) in the primary solid (austenite). The nominal volume fraction V_0 was directly measured from the as-cast structures, C_M and C_σ were measured previously by Banovic et al. [4], and C_0 is the nominal content of the alloys. Diffusivity values were obtained from the literature [16] and l_0 was approximated from microstructural observations. A list of the values used in this calculation can be seen in Table iii. Figure 15 shows the calculated normalized phase fraction (V_f/V_o) as a function of heat treating time and temperature. It is evident that the dissolution kinetics increase with increasing temperature due to the increased solute diffusivity at higher temperatures. Alloys CN3MN and CK3MCuN were previously studied by Lundin et al. [22] and the results of this effort were presented as Steel Founder's Society of America Research Report No. A95. This study investigated the corrosion resistance of the alloys after one hour heat treatments in the range of 1150°C – 1260°C based on microstructural characterization and sigma phase content. The effect of heat treatment time on the kinetics of dissolution was not considered, and no quantitative measurements of the residual segregation index were conducted. Heat treatment time is a crucial parameter for reducing both sigma phase content and Mo segregation profiles; therefore

volume fraction measurements and microchemical analysis will be utilized in the present work to quantify the variations in sigma phase content and level of homogenization as a function of both heat treatment time and temperature. This information will then be correlated to the corrosion resistance to determine if alloys CN3MN and CK3MCuN can be optimally heat treated to bring the corrosion resistance to a level on par with their wrought counterpart materials.

1.1.3 Research Objectives

This research has three primary objectives:

1. To determine if tighter control of test variables is required within ASTM G48A and G48E test methods to generate more reproducible test results.
2. To determine the potential influence of microsegregation, residual secondary phase content, microporosity, and macrosegregation on the corrosion resistance of cast alloys CN3MN and CK3MCuN.
3. To optimize the heat treatment of cast alloys CN3MN and CK3MCuN to provide a level of corrosion resistance similar to that of the equivalent wrought alloys (AL6XN and 254SMO).

1.2 Experimental Procedure

1.2.1 Materials

Experiments conducted to assess the influence of ASTM G48 test variables used cast and wrought 2205 duplex stainless steel as well as wrought AL6XN. The cast 2205 was produced in bar form (1” x 1” x 12”) while the wrought 2205 and AL6XN were in strip form (0.25” x 1” x 36”). The materials that were investigated in the heat treatment portion of the study were alloys CN3MN and CK3MCuN, both of which were produced in bar form (1” x 1” x 12”). CN3MN and CK3MCuN are the cast equivalents of AL6XN and 254 SMO respectively. The chemical compositions of the duplex stainless steels, and the high alloy castings and wrought equivalents are listed in Table iv and Table v, respectively.

1.2.2 Corrosion Test Practices

ASTM G48 Corrosion Testing Using ASTM E 1169

The ASTM E 1169 – 02 ruggedness testing specification was used to investigate the effect of several corrosion test variables within ASTM G48 Methods A and E. The variables that were investigated include: passivation time, passivation type, surface finish, sample orientation, and the ratio of solution volume to sample area. These variables were fit into a Plackett-Burman testing matrix and each of the variables were varied systematically between a high and low condition as shown in Table vi. The high and low values for each variable were selected to span a reasonable range allowed by the ASTM G48 specification. Corrosion samples were prepared from both the 2205 duplex stainless steel and wrought AL6XN by milling to 1.5" x 0.75" x 0.1875". Final preparation was carried out for each test condition (1 – 8) using the appropriate combination of variables described in the ruggedness matrix. (i.e. Condition 1: 80-grit surface finish, horizontal sample orientation, 30 minute passivation time, passivation in air, high ratio of solution volume to sample surface area, and flat as-prepared edges and corners). The other conditions for each variable are: 600-grit surface finish, vertical sample orientation, 24 hour passivation time, passivation in a desiccator, low ratio of solution volume to sample surface area, and rounded edges and corners. The actual high and low solution to surface area ratios are 20.2 mL/cm^2 and 3.6 mL/cm^2 respectively. The edges were prepared by either grinding the as-milled edges or rounding the edges off until smooth using an 80 grit paper.

ASTM G48 Method A

Potential variability of results produced from the ASTM G48 Method A test was investigated using wrought AL6XN corrosion test samples. Before testing, the samples were weighed to the nearest 0.001 gram and measured to record the dimensions before testing. Samples were then immersed in the acidified ferric chloride solution (6 % $FeCl_3$ by mass 1 % HCl) at 75 °C for 72 hours. After corrosion testing the samples were scrubbed using a nylon brush, ultrasonically cleaned, and dried with ethanol to remove any debris from the pits. The samples were again weighed and the change in weight was recorded.

ASTM G48 Method E

Potential variability of results produced from the ASTM G48 Method E test was investigated using both the cast and wrought 2205 duplex stainless steel. The samples were immersed in an acidified ferric chloride test solution (6% $FeCl_3$ by mass and 1% HCl) for a 24 hour period. The process was repeated at various temperatures in 5° C intervals until the critical pitting temperature was determined. After corrosion testing the samples were scrubbed using a nylon brush, ultrasonically cleaned, and dried

with ethanol to remove any debris from the pits. The criterion used to define pitting was the minimum temperature which induces 0.001" deep pitting attack on the bold surface of the sample. Pit depth was measured using a calibrated microscope capable of determining the change in height when focused on the top and bottom surface of a pit.

1.2.3 Heat Treatment Optimization of CN3MN and CK3MCuN

Microporosity Calculations and Macrosegregation Measurements

Microporosity calculations were conducted at University of Iowa by Beckermann [28]. The calculations were carried out using the Niyama criteria which can be defined as Niyama = $G/\sqrt{\varepsilon}$, where G is the temperature gradient (K/mm) and ε is the cooling rate (K/s). The Niyama value is calculated at various locations within the sample and wherever the Niyama value exceeds 0.1 $K^{1/2}s^{1/2}cm^{-1}$ the casting should be free of microporosity.

Macrosegregation measurements were conducted by sectioning CN3MN and CK3MCuN bars at 1" intervals and then performing inductively coupled plasma (ICP) chemical measurements to determine how the composition of the alloys changes as a function of distance along the bar. The ICP measurements were conducted at Iowa State University.

Sample Preparation and Heat Treatment

Alloys CN3MN and CK3MCuN were received in bar form with no post casting heat treatment. Samples were extracted from the bars and milled to 0.75" x 0.75" x 0.25". Autogenous gas-tungsten arc welds were placed on the surface of each sample using an automated GTAW setup and a 100 A current, 9.5 V voltage, 0.110 arc gap, and 7.1 inch/min travel speed. The autogenous welds were placed on the sample in order to investigate the influence of dendrite arm spacing on homogenization and dissolution kinetics. Samples were then heat treated at 1150 °C, 1205 °C, 1260 °C, and 1315 °C for 1, 2, and 4 hours in a Lindberg laboratory tube furnace. Flowing argon was utilized during heat treatment to prevent oxidation of the surface at elevated temperature.

Microstructural Characterization

Metallurgical mounts were prepared for both the as-cast and heat treated samples of CN3MN and CK3MCuN. The samples were mounted in thermosetting epoxy using a Struers automated mounting

press and polished from 120 grit to 0.05 μm using standard metallographic techniques. Electrolytic etching was necessary to reveal the secondary phase and was accomplished using a 10% sodium cyanide (NaCN) solution at 3 -5 V volts for 5 – 10 seconds. Microstructural evaluation was performed on all samples using standard light optical microscopy (LOM) techniques. Secondary phase volume fraction measurements were conducted using a Reichert – Jung Metallograph in combination with Leco Image Analysis software. A minimum of ten fields were used to characterize the volume fraction secondary phase of each sample.

Positive identification of all phases present in the microstructure of CN3MN and CK3MCuN was conducted using electron back-scatter diffraction (EBSD) and x-ray energy dispersive spectroscopy (XEDS). The EBSD and XEDS analyses were conducted using an FEI focused ion beam (FIB) milling unit equipped with both back-scattered electron and XEDS detectors. HKL Flamenco and HKL Spirit software packages were used to collect and interpret the EBSD and XEDS raw data. A 20 kV accelerating voltage was used for both techniques and a 60° sample tilt was required for the EBSD analysis. The collected EBSD patterns were processed using a band detection technique that calculates the band spacings and angles to determine how closely the pattern matches known standard patterns. The mean angular deviation (MAD) is a measure of how well the experimental patterns agree with the standards and a MAD < 1° is generally considered confirmation of positive phase identification [29].

Electron probe microanalysis (EPMA) was performed using a JEOL 733 Superprobe with integrated wavelength dispersive spectrometers (WDS). Final polishing of all microprobe samples was conducted using 1 μm diamond polishing compound to prevent contamination. All measurements were made using a 20 kV accelerating voltage with a stabilized 35 nA beam current. The Fe, Ni, Cr, Mo, and Si concentrations were measured with this technique and a phi(ρz) correction scheme was used to correct for any absorption and fluorescence of x-ray that occurs during collection [30]. Approximately 100 – 150 individual EPMA measurements were made across the dendritic substructure of each sample that was investigated yielding a total of nearly 1250 individual EPMA measurements. A homogeneity criteria, which determines whether the raw, uncorrected x-ray intensities that are collected for each element fall within the statistical limits of a homogenous sample, was used to determine when complete homogenization was achieved. The details of this analysis will be discussed in the results section of this report.

ASTM G48A Corrosion Testing of Heat Treated Samples

After heat treating, samples for corrosion testing according to ASTM G48A were prepared to an 80 grit surface finish. The samples were then weighed (to the nearest 0.001 g) and measured to record the

dimensions before testing. Samples were then immersed in the acidified ferric chloride solution (6 % $FeCl_3$ by mass 1 % HCl) at 75 °C for 72 hours. After corrosion testing, the samples were scrubbed using a nylon brush, ultrasonically cleaned, and dried with ethanol to remove any debris from the pits. The samples were again weighed and the change in weight was recorded.

1.3 Results and Discussion

1.3.1 Corrosion Test Practices

ASTM G48E

The ASTM G48E corrosion testing results for the wrought 2205 duplex stainless steel are given in Table vii and show that the various test conditions produce CPT results which range from 25 °C to 40 °C. Each of the eight conditions in the ruggedness matrix was tested in triplicate and the results represent the range of CPT values that were generated for each test condition. It was necessary to report a range of CPT values for condition sets 3, 4, and 7 because the onset of pitting began at different temperatures across the three samples that were tested. When a range of CPT values were generated for a test condition, the average CPT value was used in the "effect" calculation. If all three samples for a given test condition produced the same CPT then only one value is listed. The CPT values that were determined for each test condition were then used to calculate the relative effect that each individual variable (surface finish, passivation time, etc.) had on the results of the test. For example, the relative effect (E) of surface finish is calculated using the following equation:

$$E = \frac{\sum Variable\ 1\ (600)}{\frac{N}{2}} - \frac{\sum Variable\ 1\ (80)}{\frac{N}{2}} = 4.4°C \qquad (9)$$

where the first term represents the average CPT value of all test conditions prepared with a 600-grit surface finish, the second term represents the average CPT value of all test conditions prepared with an 80-grit surface finish, 4.4 °C is the relative effect of surface finish and N is the number of test conditions. The practical relevance of this result is that changing the final surface preparation from an 80-grit step to a 600-grit step will, on average, cause a 4.4 °C increase in the CPT. The three variables that have the greatest effect on the resultant CPT values for the wrought 2205 testing matrix are surface finish, passivation time, and passivation type. Each of these variables plays an important role in the formation of the passive oxide layer that protects the surface of the material and affects the overall corrosion performance. Of the three variables with the largest effect, only passivation time (9.4 °C) had an effect

larger than 5 °C. This is significant since the inherent resolution of the test is on the order of 5 °C since three samples which are tested under identical conditions can produce a 5 °C variation in the CPT. Therefore, the results of the wrought 2205 testing matrix indicate that passivation time is the only statistically significant variable which has an effect on the results that is larger than the resolution of the test.

The results of the ASTM G48E cast 2205 ruggedness testing matrix can be seen in Table viii. The CPT values generated for the cast material range from 25 °C to 30 °C, which is significantly smaller than the 15 °C range generated for the wrought material. The reduction in the range of critical pitting temperatures generated in the matrix makes the extraction of any useful trends from the data difficult. The compression of the data into a smaller range of CPT values causes the calculated effects of the individual test variables to decrease significantly. The variables with the largest effect are sample orientation and solution volume to surface area ratio, but these variables only have a 2.5 °C impact on the results. As noted above, the resolution of the test method is on the order of 5 °C, which makes the impact of these two variables statistically insignificant. Therefore, any noteworthy effects of the test variables are thus indiscernible due to the relatively low corrosion resistance of the cast 2205 material.

ASTM G48A

The results of the ASTM G48A ruggedness testing matrix conducted using wrought AL6XN can be seen in Table ix. The ASTM G48A matrix is constructed in an identical fashion to the matrix used to investigate G48E and the same variables and condition sets are used. Each condition set has the normalized weight change (g/m^2) given for each of the three samples tested as well as the average normalized weight change and standard deviation. The normalized weight change is the change in weight in grams divided by the surface area of each sample in square meters. The effect of each variable was calculated using the average normalized weight changes and equation (9) as described in the previous section. The results of this matrix indicate, similar to the cast 2205 matrix, that the variability within a given test condition is generally larger than the effect of any particular test variable. This observation is supported by comparing the results of condition set 8 with the calculated effect of each variable. Sample 1 of condition set 8 exhibited a 666 g/m^2 normalized weight change whereas samples 2 and 3 of the same condition set showed 1.0 g/m^2 and 95 g/m^2 normalized weight change respectively. This represents a variability of over 600 g/m^2 within condition set 8 which is more than twice the effect of any of the individual test variables. Similar trends are also evident for several other condition sets. Thus, the inherent variability within the test will have a larger effect on the corrosion test results than any individual variable investigated in this experiment for the alloy used in these tests.

1.3.2 Heat Treatment Optimization of CN3MN and CK3MCuN

Microporosity and Macrosegregation Results

The results of the microporosity simulations can be seen in Figure 16 for CN3MN and CK3MCuN. The Niyama calculation for CN3MN shows that while the Niyama value approaches 0.1 $K^{1/2}s^{1/2}cm^{-1}$ in the riser (top portion of the structure), the Niyama value is << 0.1 in the actual casting. This indicates that the entire cast plate should be free of microporosity and that microporosity does not play a role in reducing the corrosion resistance of cast CN3MN. An identical simulation was produced for CK3MCuN and the same trend was observed. The results of the macrosegregation measurements performed on CK3MCuN can be seen in Figure 17. The individual chemical measurements show no significant difference along the length of the casting, which indicates that no appreciable macrosegregation has occurred. Therefore, on a macro-scale, the alloying elements that provide localized corrosion resistance are evenly distributed along the length of the casting and macrosegregation is not responsible for reducing the relatively low corrosion resistance of cast alloys CN3MN and CK3MCuN.

As-Cast Microstructures

The as-cast CN3MN and CK3MCuN microstructures were characterized using EBSD, XEDS, EPMA, and volume fraction measurements to determine a baseline for assessing the effectiveness of various heat treatment times and temperatures. EBSD was carried out for the as-cast structures as well as for the entire range of heat treatment times and temperatures. Figure 18 B-D shows EBSD patterns that were collected from the matrix, the secondary phase within the eutectic, and the primary phase within the eutectic of cast CK3MCuN. The patterns presented are for heat treated CK3MCuN samples, but the same trends were observed for the as-cast structures. Both the matrix phase and the primary phase within the eutectic were indexed as austenite while the secondary phase within the eutectic was identified as sigma (σ). The process of collecting and indexing EBSD patterns was carried out over the range of heat treatment times and temperatures for both CN3MN and CK3MCuN. In all cases the phases were identified in the same fashion as above in which was the secondary phase, and the MAD for the all patterns was less than 1°. Figure 19 B-D shows XEDS spectra, which were gathered from the same regions that the EBSD signal was generated from. The XEDS plots show enriched levels of Cr and Mo in the sigma phase when compared to the austenite in both the matrix and the eutectic. This result

qualitatively agrees with the EBSD findings since others [4] have shown that sigma phase is typically enriched in Cr and Mo concentrations.

Figure 20 shows the as-cast CN3MN and CK3MCuN microstructures as well as the as-welded microstructures present due to the autogenous welds that were placed on the surface. The microstructure of both alloys consists of an austenite matrix with an austenite + sigma eutectic type constituent.

The concepts of back-diffusion and the alpha parameter were discussed in previous sections and it was demonstrated that no significant back-diffusion of Mo is expected to occur in CN3MN and CK3MCuN since they exhibited alpha parameters << 1 for solidification conditions typical of castings - Figure 7. Figure 21 shows an EPMA trace across several dendrites in as-cast CK3MCuN showing the initial concentration profile that is present in the alloy. The severity of the Mo concentration profile that exists across the dendrites is obvious, ranging from about 4.2 wt% Mo to about 10 wt% Mo, and the minimums and maximums on the plot represent the dendrite cores and the interdendritic regions, respectively. This compositional data can be used to calculate k values for each alloy system via the Scheil equation. At the start of solidification $f_s = 0$, which reduces the Scheil equation to $C_S = k*C_0$. Therefore, k at the start of solidification can be determined using the dendrite core and nominal composition values. For example, using 4.2 wt% Mo as C_S and 6.3 wt% Mo as C_0, k is calculated to be 0.66, which is very close to value of 0.65 reported in the literature for AL6XN. Since no back-diffusion is expected, direct inspection of the k values for the critical alloying elements can be used to determine the final degree of microsegregation that should be present in the as-solidified structures. A list of the k values for CK3MCuN is given in Table x. The degree of microsegregation will increase with decreasing k-values (if $k < 1$) and therefore Mo ($k = 0.66$) would be expected to exhibit the most severe concentration profiles. Ni ($k = 0.98$) and Cr ($k = 0.99$) are reasonably close to 1.0, which signifies that they should exhibit a lesser degree of microsegregation with a small concentration gradient. Iron ($k = 1.04$) has a k value > 1 which indicates that it segregates in the opposite direction as Mo.

Sigma Phase Dissolution Kinetics

The reduced microstructural scale of the welded structures is obvious when compared with the cast material, and the effect of this reduced microstructural scale on the dissolution kinetics is elucidated by Figure 22 and Figure 23. These figures show the dissolution behavior of CN3MN and CK3MCuN after heat treatment at 1150°C for 1, 2, and 4 hours. The microstructure of cast CN3MN and CK3MCuN exhibit very little change after heat treatments at 1150°C from 1 to 4 hours with the exception of minimal spherodization of the eutectic islands. The best evidence of spherodization can be seen in the CK3MCuN 1150°C, 4 hour sample (Figure 23 C), where the long continuous sigma phase particles that were present

in the as-cast material have begun to separate into smaller spherical particles. The effect of microstructural scale on dissolution kinetics can be observed in the weld after a one hour exposure at 1150°C. The as-cast microstructure is essentially unaffected by the heat treatment while the weld microstructure has undergone complete dissolution and is free of sigma phase. This can be attributed to the reduced microstructural scale of the weld (~10 μm) compared to the as-cast structure (~35 μm). The microstructural evolution of CN3MN and CK3MCuN at 1205°C is shown in Figure 24 and Figure 25 respectively. Significant dissolution of the sigma phase occurs after a 2 hour heat treatment and dissolution is essentially complete after 4 hours. After heat treatment at 1260°C and 1315°C, partial melting of the alloy occurs without dissolution of the sigma phase. This is demonstrated in Figure 26 for heat treatment of both alloys at 1260 °C. Therefore, the 1260°C and 1315°C heat treatments were not considered further.

Quantification of the above observations was conducted using volume fraction measurements of the 1150°C and 1205°C heat treatments for alloys CN3MN and CK3MCuN. The results of the volume fraction measurements after 1150°C and 1205°C heat treatments in both alloys were compared to the predicted dissolution kinetics calculated using equation 8. A list of the parameters used for the calculation can be seen in Table iii. The values of V_0 and l_0 were measured from the as-cast structures. C_M was approximated from the pseudo-binary phase diagram, C_0 is the nominal Mo content in the alloys, and C_σ was determined in a previous study using EPMA [4]. Molybdenum concentrations are used because Mo diffusion is the rate-limiting step that controls the sigma phase dissolution kinetics. It is also worth noting that equation 8 was developed for use with binary alloys and that CN3MN and CK3MCuN are being treated as pseudo-binary alloys as was explained previously. Figure 27 and Figure 28 show reasonable agreement between the calculated and measured volume fraction sigma phase as a function of time at temperature for alloys CN3MN and CK3MCuN respectively. The volume fraction measurements confirm that only moderate dissolution of the sigma phase occurs after 4 hours at 1150°C while 4 hours at 1205°C completely dissolves the sigma phase. The observation that full dissolution occurs in the autogenous weld with a reduced dendrite spacing of 10μm was also compared with the calculated results. The calculation is in agreement with the experimental observations in that a 1 hour, 1150°C heat treatment is capable of fully dissolving the sigma phase in the weld microstructure of both alloys.

Homogenization Kinetics and Residual Segregation

The EPMA results for the two extreme conditions of residual segregation (as cast and 1205°C/4 hours) can be seen in Figure 21 and Figure 29 respectively, for CK3MCuN. An intermediate heat treatment, 1150 °C / 4 hours, is presented in Figure 30. (A full listing of all EPMA data can be found in

Figure 41 through Figure 50.) In Figure 29 there is very little variation in the alloy concentration as a function of distance across the dendritic substructure, which indicates that heat treatment at 1205 °C for 4 hours completely homogenized this alloy. Figure 30 shows an intermediate amount of residual microsegregation, which signifies that 1150°C, 4 hours does not provide an adequate combination of time and temperature to induce complete homogenization.

The electron microprobe data was used to calculate the index of residual segregation for each heat treatment condition using equation 3. The experimental index of residual segregation measurements are compared with calculated values in Figure 31 and Figure 32. The experimental results indicate that complete homogenization of the alloys is achieved after a 1205°C, 4 hour heat treatment while only minimal homogenization occurs in both alloys after heat treatment at 1150°C for up to 4 hours. Complete homogeneity was confirmed using a homogeneity criteria which determines whether the raw, uncorrected x-ray intensities that are collected for each element fall within the statistical limits of a homogenous sample. The homogeneity criteria is given as:[30]

$$\overline{N} - 3\sqrt{\overline{N}} \le N_i \le \overline{N} + 3\sqrt{\overline{N}} \qquad (10)$$

where N_i is the measured Mo x-ray intensity of a given measurement and $\overline{N}$ is the average Mo x-ray intensity of all measurements. Therefore, heat treatment conditions in which all x-ray intensity measurements fell within the sample homogeneity criteria are statistically homogenous and assigned a □ value of zero.

The measured homogenization kinetics are much slower than predicted by the previous model - Figure 13. This result is not unexpected since complete homogenization of these alloys requires that the sigma phase must first be dissolved. The homogenization model assumes a single phase microstructure and thus does not take the presence of a secondary phase (in this case sigma) into account. The presence of sigma phase is significant because it will pump Mo into the primary austenite as it dissolves. Therefore complete homogenization is not attainable until the sigma phase is completely dissolved. In order to account for the effect of a secondary phase, an additional model by Sinder et al. [31] was used to determine how much additional time was required for homogenization immediately following dissolution of the sigma particles. The model utilizes a supersaturation parameter, γ_{sin}, which is defined as:

$$\gamma_{\sin} \equiv \frac{C_I - C_0}{C_\sigma - C_I} \qquad (11)$$

where C_I is the interface composition (~8.5 wt % Mo), C_0 is the nominal composition (6.3 wt % Mo), and C_σ is the precipitate composition (~ 26 wt % Mo). The γ_{sin} parameter for alloys CN3MN and CK3MCuN range from approximately 0.10 - 0.15. The model also defines a dimensionless time parameter, τ, which represents the time required for dissolution (τ_{dis}) and various levels of homogenization ($\tau_{0.1}$ and $\tau_{0.5}$). The

values $\tau_{0.1}$ and $\tau_{0.5}$ represent the time required to reduce the concentration profile to $0.1(C_I - C_0)$ and $0.5(C_I - C_0)$ respectively. Therefore, $\tau_{0.1}$ and $\tau_{0.5}$ essentially represent the relative time required to eliminate 90% and 50% respectively of the initial composition profile present in the alloy. Figure 33 shows the values of τ_{dis}, $\tau_{0.1}$, and $\tau_{0.5}$ as a function of γ_{sin}. Note that the time required for nearly complete homogenization (i.e. $\tau_{0.1}$) is shorter than that required for complete dissolution (τ_{dis}). Therefore very little additional time would be required once dissolution is completed to finish homogenizing the alloy. This result was expected since homogenization kinetics are generally much more rapid than for dissolution. Figure 34 shows the calculated homogenization and dissolution kinetics expected during heat treatment at both 1150°C and 1205°C. For both heat treatment temperatures it is evident that the homogenization kinetics are much more rapid than for dissolution. This behavior can also be explained mechanistically since the sigma phase particles act as secondary sources of Mo. Therefore the chemical gradients in the alloy cannot be completely eliminated until the sigma phase has completely dissolved. The measured data is consistent with this since complete homogenization of the alloys is not observed until the sigma phase particles have been completely dissolved, which occurs between 2 and 4 hours at 1205°C. Therefore, complete homogenization and of the alloy is observed after a 1205°C, 4 hour heat treatment.

Based on the calculations and discussion above it is apparent that dissolution of the sigma phase is the rate limiting step during the heat treatment of alloys CN3MN and CK3MCuN. Therefore the dissolution kinetics can be used as a predictive tool to estimate the times and temperatures required for effective heat treatment of these alloys. Figure 35 and Figure 36 show master curves that were generated for alloys CN3MN and CK3MCuN. This information can be used to estimate when various levels of dissolution are achieved during heat treatment at various times and temperatures based on the cooling rate of the casting. The cooling rate is used with equation 6 to determine the dendrite arm spacing, which is then used to calculate the dissolution kinetics using equation 8 as discussed previously. This information is of practical importance since optimal heat treatment times can be deduced from the cooling rate, which is typically a known casting parameter. Similar curves can be generated for any heat treatment temperature, and this information could be used as a basis for selecting the most efficient heat treating schedules. Master homogenization curves could also be generated for various heat treatment temperatures. This information would be far less valuable since dissolution has been shown to be the rate-limiting step during the heat treatment process due to its slower kinetics. Therefore, using the dissolution kinetics as a guide allows for selection of optimal heat treatment times based on the heat treatment temperature and the cooling rate of the casting.

Corrosion Resistance of Heat Treated Alloys

The corrosion resistance of as-cast and heat-treated CN3MN as well as wrought AL6XN can be seen in Figure 37. It is clear that the corrosion resistance of the alloy improves drastically with heat treating when the as-cast material (22.3 % weight loss) is compared to the optimal 1205°C / 4 hour heat treatment (1.7 % weight loss). This indicates that the levels of dissolution and homogenization achieved after optimal heat treatment (1205 °C / 4 hour) are effective at restoring the corrosion resistance of the alloy. It is even more significant to compare the corrosion resistance of the 1205°C / 4 hour heat treatment with that of the wrought AL6XN sample (5.4 % weight loss). The optimally heat treated CN3MN casting is comparable to its wrought equivalent once the microsegregation and residual secondary phase are removed from the structure. Figure 38 shows the weight loss of CN3MN as a function of the index of residual segregation. These results support the idea that the corrosion resistance of the alloy dramatically improves as the critical alloying elements (Cr, Mo) are evenly redistributed throughout the structure. The same general trends are observed for as–cast and heat treated CK3MCuN. Figure 39 and Figure 40 show that the corrosion resistance improves as the index of residual segregation decreases and the optimally heat treated CK3MCuN exhibits corrosion resistance similar to its wrought counterpart material.

Chapter 2: Influence of Heat Treatment on Impact Toughness and Corrosion Resistance of CF-3, CF-3M, CF-8, and CF-8M

2.1 Procedure

Eight different stainless steel alloy compositions were cast to the compositions shown in Table xi. The alloys have systematic variations in the C and Mo contents as well as Ni_{eq}/Cr_{eq} ratios and ferrite contents. The molten steel was taken directly from the furnace and poured at a temperature of 2800-2850°F (1538-1566°C) into a non-bake organic mold. The castings then received one of four heat treatments: 1900°F (1038°C) for 1 or 4 hours or 2200°F (1204°C) for 1 or 4 hours. Following heat treatment, the bars were charpy tested at room temperature according to ASTM E23. Corrosion testing was performed according to ASTM G48A at a temperature of 167°F (75°C). Light optical microscopic examination was performed on the as-cast, heat treated, and corrosion tested samples. Samples were prepared using standard metallographic techniques for the as-cast and heat treated samples. A mixture of paraffin wax and kerosene was used as a lubricant during grinding, in lieu of water, in order to preserve any water soluble corrosion product that may have formed. In addition, all cleaning performed between steps was performed using only ethanol for the same reasons. The low ferrite alloys were electrolytically etched with a 10% oxalic acid solution using 2V for 30-60sec, and the high ferrite alloys were electrolytically etched with a 60%/40% HNO_3/H_2O solution using 5V for 5sec.

2.2 Results

Figure 51 shows the eight alloys used in this study with their Ni_{eq} and Cr_{eq} plotted on the WRC 1992 diagram. This shows that the LF alloys had an austenite or austenite-ferrite primary solidification mode, whereas the HF alloys had a primary ferrite solidification mode. Figure 52 through Figure 55 show the results of charpy impact testing for all 8 alloys in the as-cast as well as heat treated conditions. The impact toughness of alloys CF-3-LF (Figure 52) and CF-8-LF (Figure 54) remained relatively unchanged after heat treatment (232ft-lbs. and 239ft-lbs., respectively); the remaining alloys, by comparison, all showed an increase in impact toughness as the heat treatment time or temperature increased. The light optical photomicrographs for each of the alloys can be seen in Figure 56 through Figure 63. Depending on the extent of heat treatment, ferrite in the cast alloys will spherodize, or spherodize then completely dissolve. For comparison, Figure 64 shows the impact toughness for the wrought counterparts for these cast alloys.

Figure 65 through Figure 68 show the results of the corrosion testing for all eight alloys in the as-cast and the 2200°F heat treatment conditions. Only CF-3-HF (Figure 65) and CF-8-HF (Figure 67) showed a clear trend where amount of mass loss decreased with longer heat treatment. The trends seen in all other alloys and heat treatments were inconclusive due to testing of only two samples for each condition. Further testing of more samples could potentially generate more conclusive trends. Light optical photomicrographs were taken for the CF-8 and CF-8M alloys (both LF and HF) (Figure 69 through Figure 72). The photomicrographs show the corrosion beginning at the ferrite/austenite interface and continuing through the remainder of the ferrite network.

2.3 Discussion

There are two primary reasons for the increased charpy impact toughness due to the heat treatment of the alloys. A higher amount of austenite compared to ferrite leads to higher toughness because the face centered cubic (FCC) austenite has a lower Peierls-Nabarro stress compared to the body centered cubic (BCC) ferrite. Austenite, therefore, has more mobile dislocations compared to ferrite, which increases plasticity in the material and increases toughness. In cases where ferrite is not completely dissolved at the most intense heat treatment (e.g., CF-8M-HF), the ferrite spherodizes and breaks up the continuous network. This eliminates an easy path for crack propagation through the continuous ferrite network and increases toughness. It should be noted that full dissolution of ferrite in some alloys is not possible. Figure 73 shows a phase diagram generated in ThermoCalc using the compositions of CF-8M alloys. During heat treatment, the HF alloys, which have higher chromium content, still remain in a two phase region of austenite and ferrite, thus eliminating the possibility of full ferrite dissolution. In comparison, the LF alloys (lower chromium) are heat treated in the single phase austenite region, making full dissolution possible.

The mechanism for ferrite dissolution has been described by Kim et al. [32] During heat treatment, $M_{23}C_6$ carbides start to form at the austenite/ferrite interface which depletes the surrounding ferrite of chromium as the carbide grows at elevated temperature creating a twofold effect. First, by depleting the ferrite of chromium it starts to become unstable and eventually dissolves. Second, the chromium depleted region at the austenite/ferrite interface has a decreased corrosion resistance, leaving a susceptible phase for preferential corrosive attack. This effect can be seen in Figure 70B as the corrosive attack begins at the austenite/ferrite interface and progresses through the entirety of the ferrite. Decreasing the total amount of ferrite in the system is beneficial, however, since ferrite is known to decrease the corrosion resistance of materials [33].

Benefits Assessment

This development of high alloy steel heat treatment guidelines will provide the steel casting industry with enhanced process controls that will result in a reduction of scrapped castings and re-work/repair and improved energy efficiencies resulting from accurate heat treatment practices. This task was predicted to result in an average energy savings of 0.05 trillion BTU's/year over a 10 year period. Current (2012) annual energy saving estimates, based on initial dissemination to the casting industry in 2010 and market penetration of 99% by 2020, is 0.25 trillion BTU's/year.

The reduction of scrap and improvement in casting yield will also result in a reduction of environmental emissions associated with the melting and pouring of the steel. The average annual estimate of CO2 reduction per year through 2020 is 0.005 Million Metric Tons of Carbon Equivalent (MM TCE).

Commercialization

The results of this investigation have been presented at numerous professional meetings held by the Steel Founders Society of America (SFSA) in order to disseminate the technology to end users. In particular, the information was presented at several SFSA High Alloy Research Committee meetings and annual SFSA T&O Conferences. As a result of this research, SFSA has taken action to modify the existing specifications for these alloys in order to improve their performance in demanding applications on a more consistent basis. In addition, several foundry members of SFSA have already modified their heat treating schedules for these alloys.

Accomplishments

- Publications:

1. J. N. DuPont and J. Farren, The Influence of Heat Treatment Time and Temperature on the Microstructure and Corrosion Resistance of Cast Superaustenitic Stainless Steels, Corrosion, Vol. 67, No. 5, 2011.
2. J.D Farren and J.N. DuPont, Heat Treatment Optimization of High Alloy Castings, MS&T 2007, Detroit, MI. Sept. 17-20, 2007
3. J.D Farren and J.N. DuPont, Heat Treatment Optimization of High Alloy Stainless Steel Castings, SFSA T&O Conference, Chicago, IL, December 14th, 2007
4. J.D. Farren and J.N. DuPont, Heat Treatment Optimization of High Alloy Stainless Steel Castings and Welds, EPRI Welding and Repair Conference, Sanibel Habour Resort and Spa, Fort Myer, FL, USA, June 18-20, 2008.
5. J.N. DuPont and J.D. Farren, Heat Treatment of High Alloy Stainless Steel Castings and Welds, 61st Annual Assembly and International Conference of the International Institute of Welding, 6 - 11 July 2008, Graz, Austria.
6. J. D. Farren and J.N. DuPont, Heat Treatment and Corrosion Resistance of High Alloy Stainless Steel Castings and Welds, International Conference on Trends in Welding Research. June 2-8, 2008, Pine Mountain, GA.

7. A. Stockdale, J. Farren, and J.N. DuPont, Optimizing the Corrosion Resistance of Superaustenitic Stainless Steel Castings and Welds, SFSA T&O Conference, Chicago, IL, Dec. 10-100, 2009.
8. Jeff Farren and John DuPont, Heat Treatment Optimization of High Alloy Stainless Steel Castings and Welds, 88th Annual American Welding Society Conference, Chicago, IL, November 11-14, 2007.
9. W. Stockdale and J.N. DuPont, Optimizing Corrosion Performance of Welds on 6 wt% Mo Superaustenitic Stainless Steels, International Conference on Trends in Welding Research. June 2-8, 2008, Pine Mountain, GA
10. A. Stockdale and J.N DuPont, Corrosion Performance of Welds on 6 wt% Mo Superaustenitic Stainless Steels, MS&T Conference Proceedings, Pittsburgh, PA, October 26-28, 2009, ASM International, Materials Park, OH.
11. A. Stockdale and J.N. DuPont, Optimizing Corrosion Performance in Welds of 6 wt% Mo Stainless Steels, 89th Annual American Welding Society Conference, Las Vegas, NV, October 6-8, 2008.
12. A. Stockdale and J.N. DuPont, Fusion Welding and Corrosion Behavior of High Alloy Stainless Steel Welds, American Welding Society Conference, Chicago, IL, Nov. 16-18, 2009.
13. A. Stockdale and J. DuPont, Microstructural Evolution and Corrosion Resistance of Fusion Welds on Alloy CN3MN made with IN686 Filler Metal, Science and Technology of Welding and Joining, July, 2011, pp 426-432.

- Graduate student theses based on this project work:
    - Jeffrey D. Farren
    - Andrew W. Stockdale
    - Brett M. Leister

Conclusions

Corrosion Test Practices

- The wrought 2205 matrix used to investigate the ASTM G48E corrosion testing procedure indicates that a variation in passivation time from 30 minutes to 24 hours can induce a change in the critical pitting temperature of 9.4 ^{o}C, which is larger than the inherent variability of the test (approximately 5 ^{o}C). Variation of other test variables (passivation type, surface finish, gravity, edge preparation, and solution volume to surface area ratio) was observed to be insignificant because their effect on the critical pitting temperature was below the inherent variability of the test.
- The use of cast 2205 samples for ASTM G48E corrosion testing did not yield any significant trends because the CPT values were grouped between 25°C and 30°C for all condition sets. Therefore, no single test variable had a significant effect on the test results.
- The use of AL6XN wrought alloy samples for ASTM G48A corrosion testing showed that no test variable had an effect on the results that was larger than the inherent resolution of the testing procedure.

- Except for passivation time, tighter control of ASTM G48A and ASTM G48E corrosion test variables will not lead to better reproducibility of test results with the materials considered here because the variability produced using identical conditions is generally larger than the effect of any individual variable.

Heat Treatment and Corrosion Resistance of CN3MN and CK3MCuN

- The as-solidified microstructures of CN3MN and CK3MCuN consist of a cored austenite matrix with an austenite + sigma eutectic type constituent. These two phases persist during heat treatment and no new phases are observed.
- Partial dissolution of the sigma phase in cast CN3MN and CK3MCuN occurred during heat treatment at 1150°C while full dissolution was possible after a four hour heat treatment at 1205°C.
- The autogenous welds exhibited full dissolution after an 1150°C, 1 hour heat treatment due to the smaller dendrite spacing, 10 μm compared to approximately 35 μm, which reduces the diffusion distance and concomitant time required for dissolution.
- The dissolution model used to predict the times and temperatures required to achieve various amounts of sigma phase dissolution showed reasonably good agreement with the experimental data.
- EPMA showed that cast CN3MN and CK3MCuN underwent partial homogenization at 1150°C from 1 to 4 hours while complete homogenization occurred at 1205°C after 4 hours.
- EPMA performed on the autogenous welds showed complete homogenization of the weld structure after an 1150°C, 1 hour heat treatment which shows the influence of microstructural scale on the homogenization kinetics.
- The experimental homogenization kinetics were slower than those predicted by the homogenization model. This result is expected since full dissolution of the sigma phase must occur before complete homogenization is possible.
- The corrosion resistance of the cast alloys is controlled by the amount of secondary phase and extent of residual segregation. Macrosegregation and microporosity did not play a significant role in the corrosion resistance of the alloys considered in this work. The corrosion resistance of the cast alloys increases significantly as secondary sigma phase is dissolved and the index of residual segregation decreases.

The corrosion resistance of optimally heat treated (1205 °C/4 hours) CN3MN and CK3MCuN were shown to be comparable to the corrosion resistance of their wrought counterparts AL6XN and 254SMO.

Influence of Heat Treatment on Impact Toughness and Corrosion Resistance of CF-3, CF-3M, CF-8, and CF-8M

- Impact toughness is not improved by heat treatment for CF-3-LF and CF-8-LF alloys.
- Peak impact toughness for all other alloys was achieved after a heat treatment of 2200°F for 1 hour.
- Corrosion resistance was optimized for CF-3-HF and CF-8-HF alloys utilizing a heat treatment of 2200°F for 4 hours.
- More corrosion tests are needed for all other alloys in order to obtain more accurate results and trends.

Recommendations

- A heat treatment of 1205C for 4 hours for CN3MN and CK3MCuN is recommended to achieve corrosion resistance equivalent to wrought counterparts.
- A heat treatment of 2200F for 1 hour for CF-3, CF-3M, CF-8, and CF-8M is recommended in order to maximize charpy impact toughness.
- A heat treatment of 2200F for 4 hours for CF-3-HF and CF-8-HF is recommended to optimize corrosion resistance.
- Further corrosion testing is required for CF-3-LF, CF-3M, CF-8-LF, and CF-8M in order to gain a better understanding of the corrosion performance of these alloys.

Table i - Effect of Temperature on Time to Breakdown Using a Large Crevice Assembly

	Average Times to Breakdown (Hours)	
	Time	
	30°C	16°C
Type 316	136 +/- 91	566 +/- 104
UNS N08904	141 +/- 112	528 +/- 85

Table ii - List of parameters used in alpha calculation.

Solidification Temperature Range	1354 °C -1410 °C
Cooling Rate Range ε (°C/s)	0.1 - 20
Solidification Time Range (s)	2.8 - 560
Dendrite Arm Spacing Range λ (μm)	30 - 170
Diffusivity Range (m^2/s)	$2 \times 10^{-13} - 4 \times 10^{-13}$

Table iii - List of parameters used to calculate the sigma volume fraction expected after 1150°C and 1205°C heat treatments in alloy CN3MN and CK3MCuN

	CK3MCuN 1150°C	CK3MCuN 1205°C	CN3MN 1150°C	CN3MN 1205°C
C_M	10.5 wt% Mo	10.5 wt% Mo	10.5 wt% Mo	10.5 wt% Mo
C_0	6.3 wt% Mo	6.3 wt% Mo	6.4 wt% Mo	6.4 wt% Mo
C_σ	25.9 wt% Mo	25.9 wt% Mo	25.9 wt% Mo	25.9 wt% Mo
D_s	8.50×10^{-15} m^2/s	2.00×10^{-14} m^2/s	8.50×10^{-15} m^2/s	2.00×10^{-14} m^2/s
l_0	17.5 microns	17.5 microns	17.5 microns	17.5 microns
V_0	3.93 vol %	3.93 vol %	1.83 vol %	1.83 vol %

Table iv - Chemical composition (in wt %) of cast and wrought 2205 duplex stainless steel.

Element	Cast 2205	Wrought 2205
C	0.02	0.19
Cr	21.2	22.6
Cu	0.14	---
Fe	Bal.	Bal.
Mn	0.89	1.48
Mo	2.9	3.16
N	0.22	0.19
Ni	4.9	5.59
P	0.02	0.025
S	0.002	0.002
Si	0.73	0.37

Table v - Chemical compositions (in wt %) of alloys CN3MN and CK3MCuN.

Element	CN3MN	CK3MCuN	AL6XN	254 SMO
C	0.02	0.02	0.02	0.02
Cr	21.45	19.91	21.44	20.02
Cu	0.06	0.550	0.19	0.56
Fe	45.92	52.39	47.22	53.23
Mn	0.47	0.560	0.25	0.55
Mo	6.40	6.30	6.30	6.40
N	0.23	0.224	0.23	0.215
Ni	24.40	18.940	23.80	18.3
P	0.013	0.014	0.028	0.029
S	0.007	0.006	<0.001	<0.01
Si	0.99	1.080	0.30	0.67

Table vi - ASTM E1169 ruggedness testing matrix used to determine the effect of corrosion test variables in ASTM G48E

Test Variables						
Test Condition	Surface Grit	Gravity	Passivation Time	Passivation Type	Volume to Surface Area	Edge Preparation
1	80	Horizontal	30 min	Air	High	Flat
2	80	Horizontal	24 hrs	Air	Low	Rounded
3	80	Vertical	30 min	Desiccator	High	Rounded
4	80	Vertical	24 hrs	Desiccator	Low	Flat
5	600	Horizontal	30 min	Desiccator	Low	Flat
6	600	Horizontal	24 hrs	Desiccator	High	Rounded
7	600	Vertical	30 min	Air	Low	Rounded
8	600	Vertical	24 hrs	Air	High	Flat

Table vii - ASTM E1169 testing matrix showing the results of ASTM G48 E testing of wrought 2205 duplex stainless steel.

Wrought 2205							
Test Condition	Surface Grit	Sample Orientation	Passivation time	Passivation type	Solution Volume / SA Ratio	Edges Surfaces	CPT °C
1	80	H	30 mins	A	H	F	25 °C
2	80	H	24 hrs	A	L	R	35 °C
3	80	V	30 mins	D	H	R	25 - 30 °C
4	80	V	24 hrs	D	L	F	35 - 40 °C
5	600	H	30 mins	D	L	F	35°C
6	600	H	24 hrs	D	H	R	40 °C
7	600	V	30 mins	A	L	R	25 - 30 °C
8	600	V	24 hrs	A	H	F	40 °C
Effect	4.4 °C	0.6 °C	9.4 °C	3.1 °C	-0.6 °C	-1.9 °C	

Suface Grit - 80 Grit or 600 Grit

Sample Orientation - Horizontal alignment or Vertical alignment

Passivation Time - 30 minutes or 24 hours

Passivation Type - Air passivation or Desicator passivation

Solution Volume to Surface Area Ratio - High Solution Ratio (400 mL) or Low Solution Ratio (70 mL)

Edge / Surface Preparation - Rounded Edges or Flat Edges

Table viii - ASTM E1169 testing matrix showing the results of ASTM G48 E testing of cast 2205 duplex stainless steel.

Cast 2205							
Test Condition	Surface Grit	Sample Orientation	Passivation time	Passivation type	Solution Volume / SA Ratio	Edges Surfaces	CPT °C
1	80	H	30	A	H	P	30 °C
2	80	H	24	A	L	R	25 °C
3	80	V	30	D	H	R	25 °C
4	80	V	24	D	L	P	25 °C
5	600	H	30	D	L	P	25 °C
6	600	H	24	D	H	R	30 °C
7	600	V	30	A	L	R	25 °C
8	600	V	24	A	H	P	25 °C
Effect	0 °C	-2.5 °C	0 °C	0 °C	-2.5 °C	0 °C	

Surface Grit - 80 Grit or 600 Grit

Sample Orientation - Horizontal alignment or Vertical alignment

Passivation Time - 30 minutes or 24 hours

Passivation Type - Air passivation or Desicator passivation

Solution Volume to Surface Area Ratio - High Solution Ratio (400 mL) or Low Solution Ratio (70 mL)

Edge / Surface Preparation - Rounded Edges or Flat Edges

Table ix - Results of ASTM E1169 investigation into ASTM G48A corrosion test variables using wrought AL6XN.

Wrought AL6XN											
	Surface Grit	Sample Orientation	Passivation time	Passivation type	Solution Volume / SA Ratio	Edges Surfaces	Normalized Weight Change (g / m^2)	Normalized Weight Change (g / m^2)	Normalized Weight Change (g / m^2)	Average	Standard Deviation
1	80	H	30	A	H	F	847.8	396.1	797.4	680.4	247.5
2	80	H	24	A	L	R	3.2	64.5	17.0	28.2	32.2
3	80	V	30	D	H	R	488.8	641.4	419.8	516.6	113.4
4	80	V	24	D	L	F	459.5	546.3	499.2	501.7	43.4
5	600	H	30	D	L	F	9.7	302.1	11.9	107.9	168.2
6	600	H	24	D	H	R	47.1	90.3	0.4	45.9	45.0
7	600	V	30	A	L	R	361.4	487.2	409.0	419.2	63.5
8	600	V	24	A	H	F	666.0	1.0	94.7	253.9	360.0
Effect	-225	207	-224	-52	-110	-133					

Surface Grit - 80 Grit or 600 Grit
Sample Orientation - Horizontal alignment or Vertical alignment
Passivation Time - 30 minutes or 24 hours
Passivation Type - Air passivation or Desicator passivation
Solution Volume to Surface Area Ratio - High Solution Ratio (400 mL) or Low Solution Ratio (70 mL)
Edge / Surface Preparation - Rounded Edges or Flat Edges

Table x - List of k values for Fe, Cr, Ni, and Mo for CK3MCuN.

Alloying Element	K Value (Partition Coefficient)
Fe	1.04
Ni	0.98
Cr	0.99
Mo	0.66

Table xi - Composition (wt%) of cast stainless steel alloys used for toughness and corrosion studies

	Elemental Composition (wt%)											
Alloy	**C**	**Mn**	**Si**	**P**	**S**	**Cr**	**Ni**	**Mo**	**Cu**	**V**	**Co**	**W**
CF-3-LF	0.03	1.40	1.26	0.017	0.007	16.79	11.92	0.37	0.21	0.06	0.04	0.00
CF-3M-LF	0.03	1.21	1.21	0.018	0.004	16.48	12.81	2.41	0.27	0.09	0.09	0.09
CF-8-LF	0.07	1.21	1.12	0.014	0.003	18.05	11.09	0.22	0.28	0.07	0.09	0.03
CF-8M-LF	0.07	1.10	1.21	0.016	0.001	17.50	11.90	2.30	0.13	0.05	0.08	0.08
CF-3-HF	0.03	1.27	1.32	0.029	0.010	20.91	7.51	0.34	0.39	0.06	0.09	0.00
CF-3M-HF	0.03	1.31	1.42	0.020	0.005	20.10	9.85	2.96	0.30	0.08	0.09	0.06
CF-8-HF	0.07	1.30	1.46	0.021	0.002	21.11	7.50	0.37	0.37	0.07	0.10	0.00
CF-8M-HF	0.07	1.19	1.41	0.021	0.003	20.31	8.61	2.19	0.33	0.07	0.08	0.06

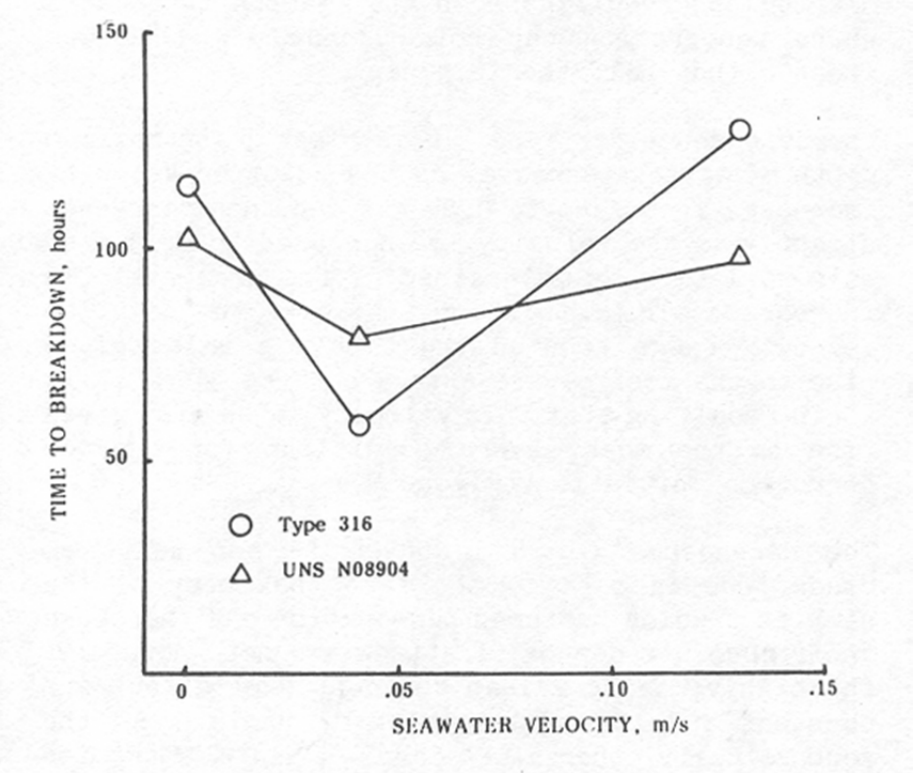

Figure 1 - Effect of solution velocity on times to breakdown

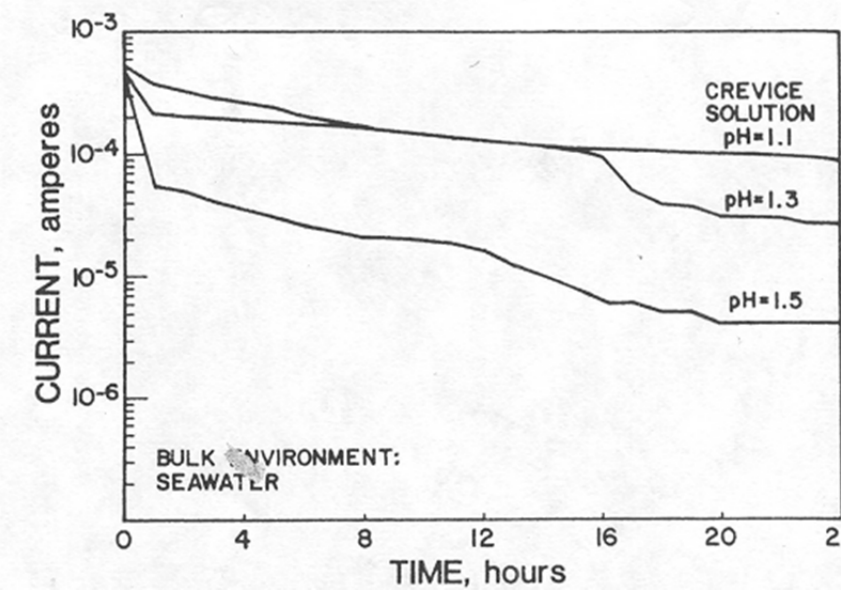

Figure 2 - Compartmentalized cell results for a 316 stainless steel showing the effect of crevice solution pH.

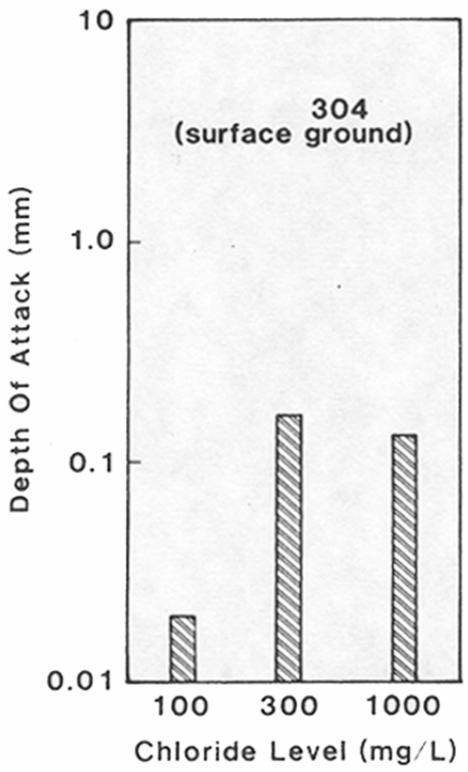

Figure 3 - Effect of chloride level in synthetic solutions for multiple crevice assembly.

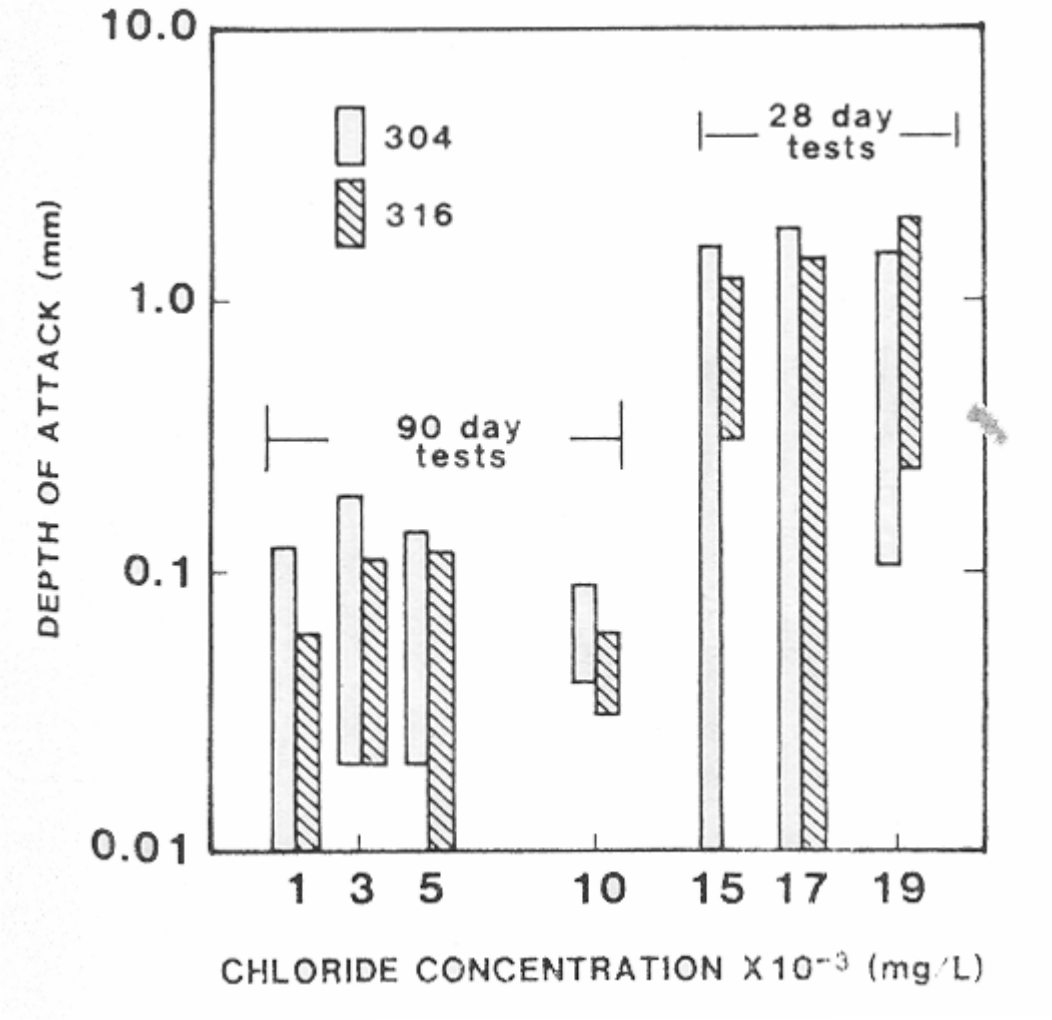

Figure 4 - Effect of chloride level in natural and dilute seawater for multiple crevice assembly.

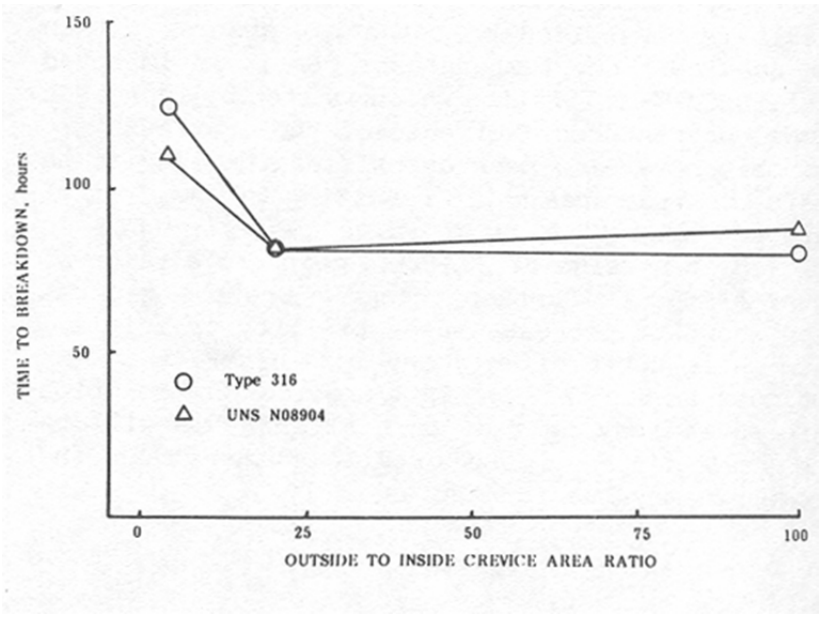

Figure 5 - Effect of outside to inside crevice area ratio on times to breakdown.

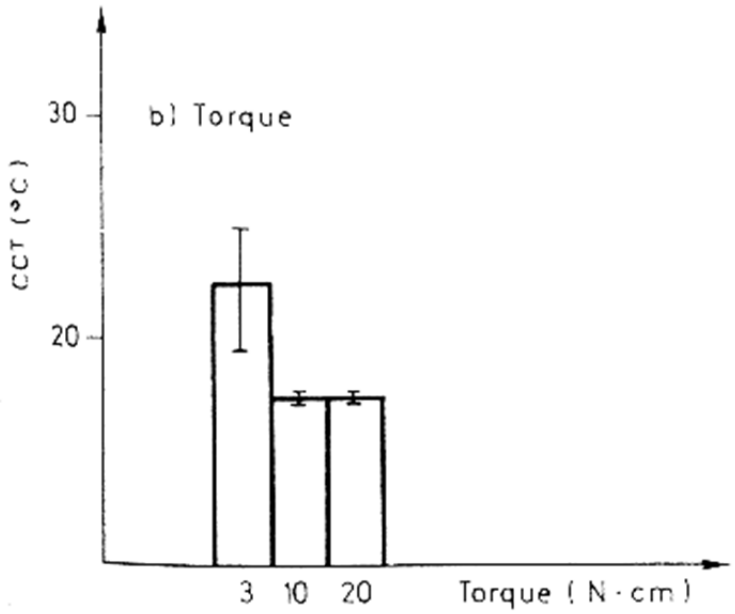

Figure 6 - Effect of torque and effective crevice gap on critical crevice temperature of an austenitic stainless steel.

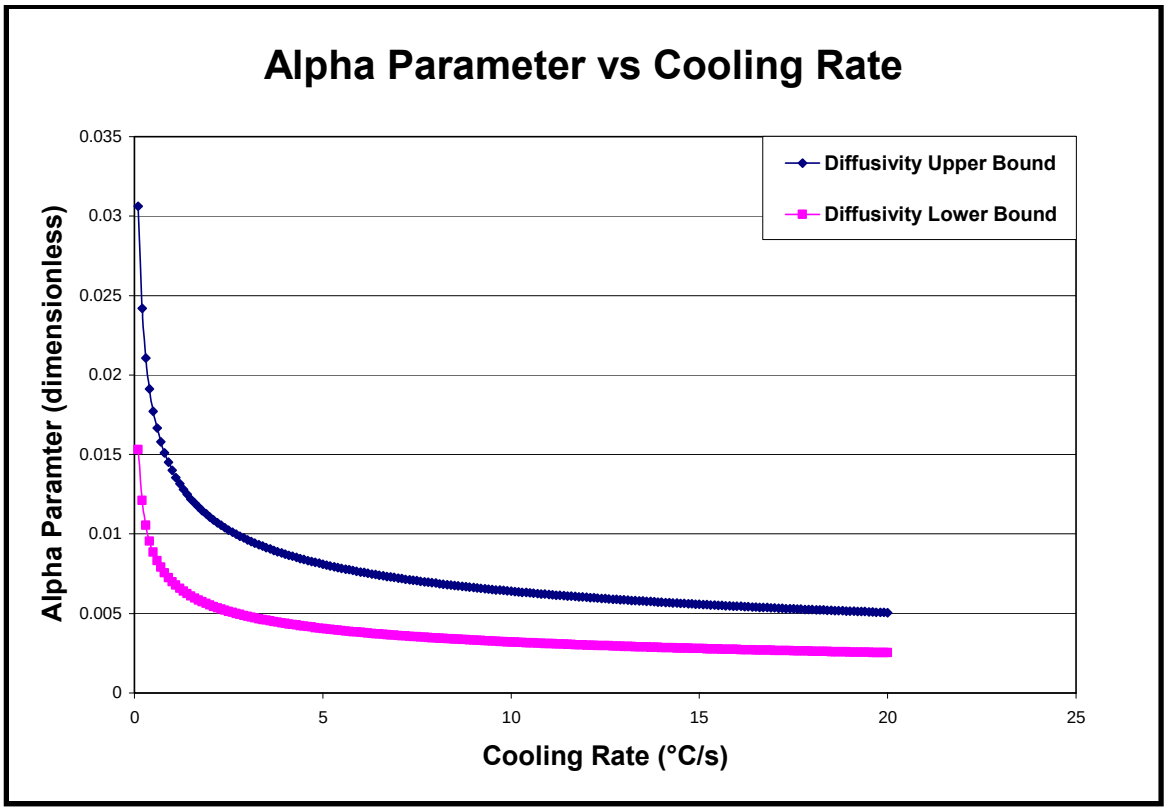

Figure 7 - Plot of alpha parameter for Molybdenum versus cooling rate for typical cooling rates used in industrial castings. The high and low extremes of diffusivity were used. The alpha parameter in both cases in << 1 and therefore Scheil conditions prevail.

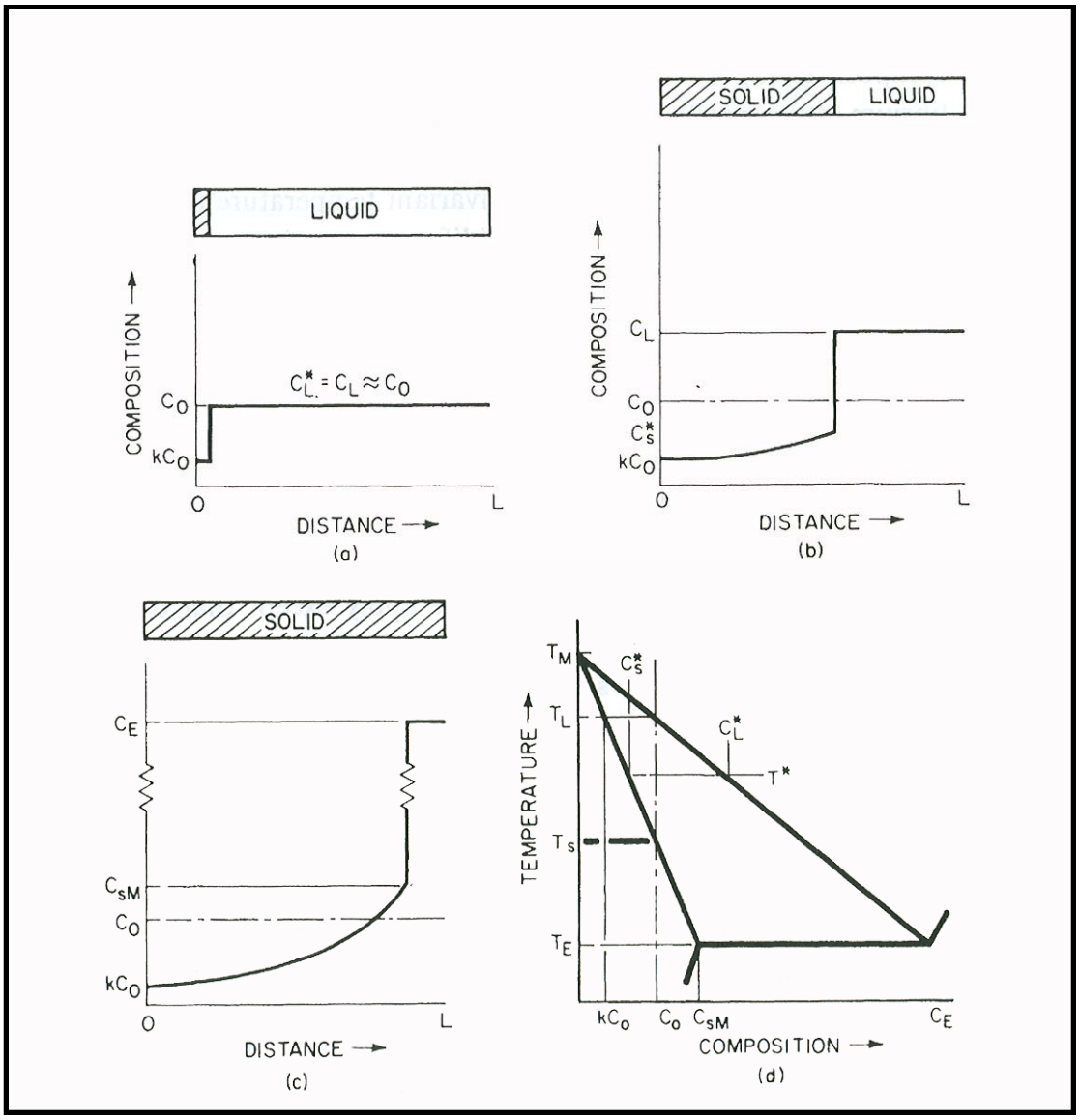

Figure 8 - Solute redistribution during Scheil solidification with no solid diffusion and complete liquid diffusion. A) onset of solidification; B) intermediate condition; C) end of solidification; and D) characteristic phase diagram.

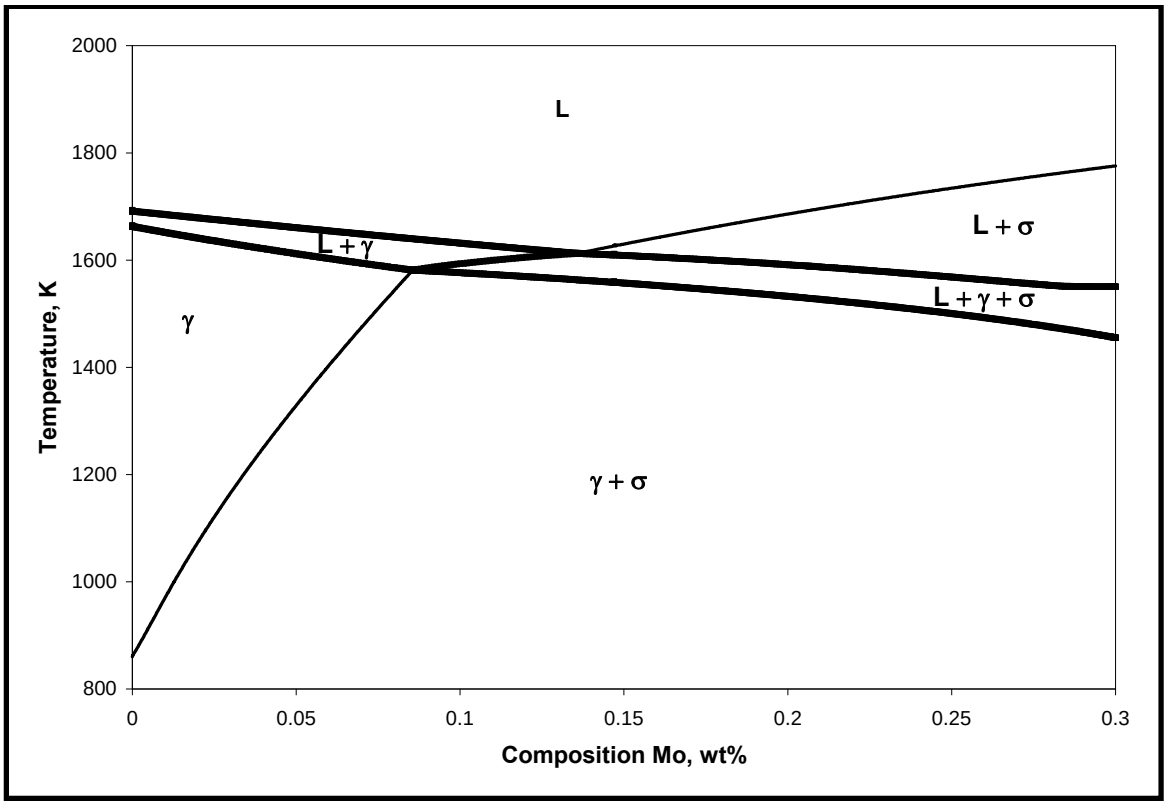

Figure 9 - Pseudo binary section of the Fe - Ni - Cr - Mo system showing characteristics similar to that of a typical binary eutectic diagram. Compositions to the left of the eutectic triangle would become enriched to the eutectic composition and form a terminal eutectic upon final cooling.

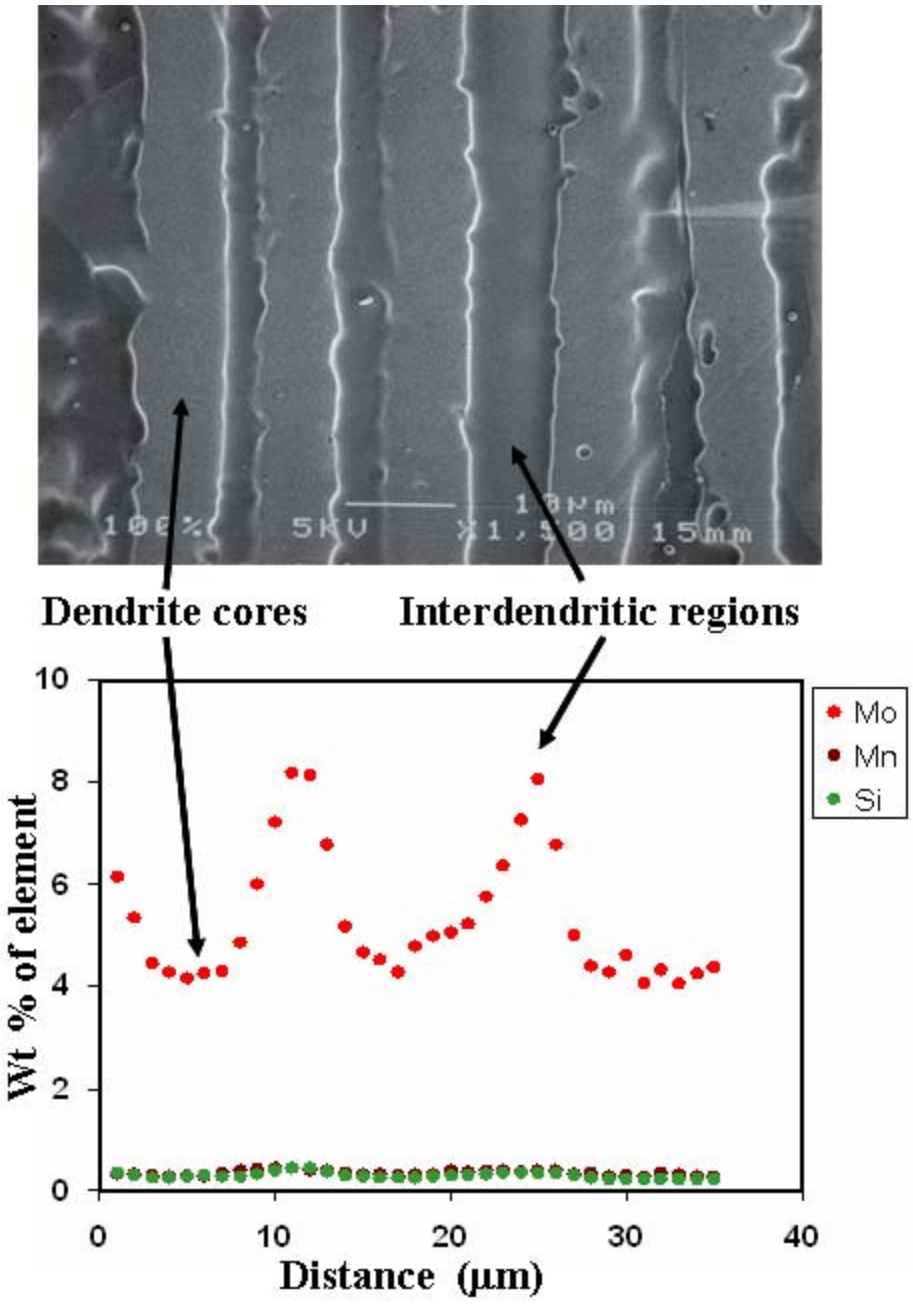

Figure 10 - SEM image of a dendritic as-welded AL6XN structure and a corresponding EPMA trace showing the segregation profile that commonly exist across dendrites. The dendrite cores are depleted in Mo.

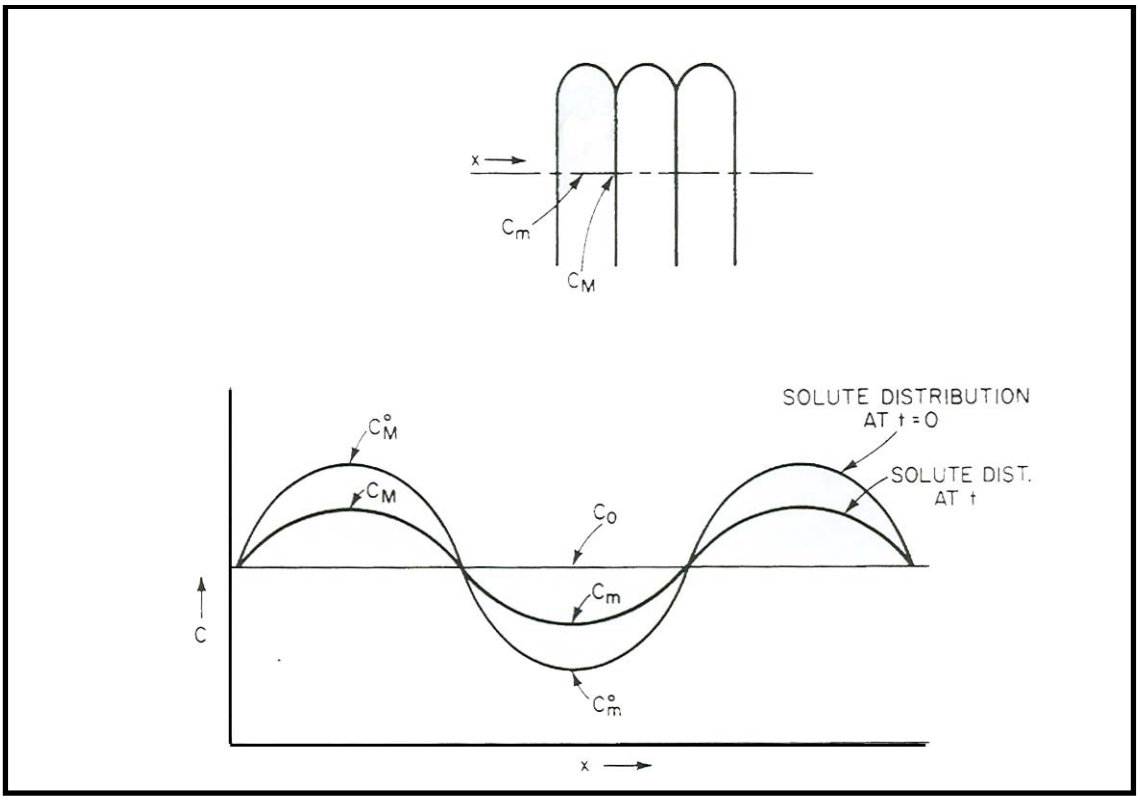

Figure 11 - Schematic representation of the concentration profile that exists across dendrite arms. There is a sinusoidal variation from the maximum to minimum concentration which decreases to the nominal composition as homogenization time is increased.

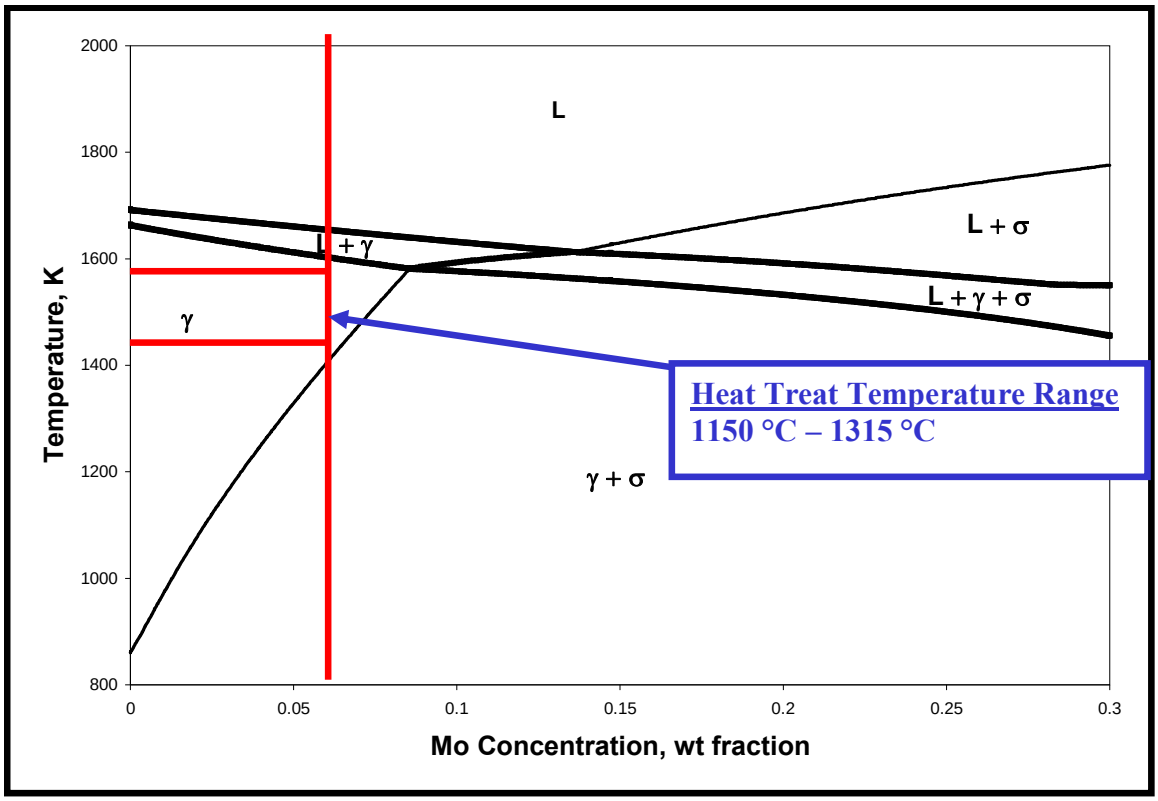

Figure 12 - CK3MCuN Pseudo-binary phase diagram showing the heat treatment temperature range that was selected for these alloys. The single phase region was selected to provide increased diffusion to aid homogenization and provide the potential to dissolve any secondary phase present.

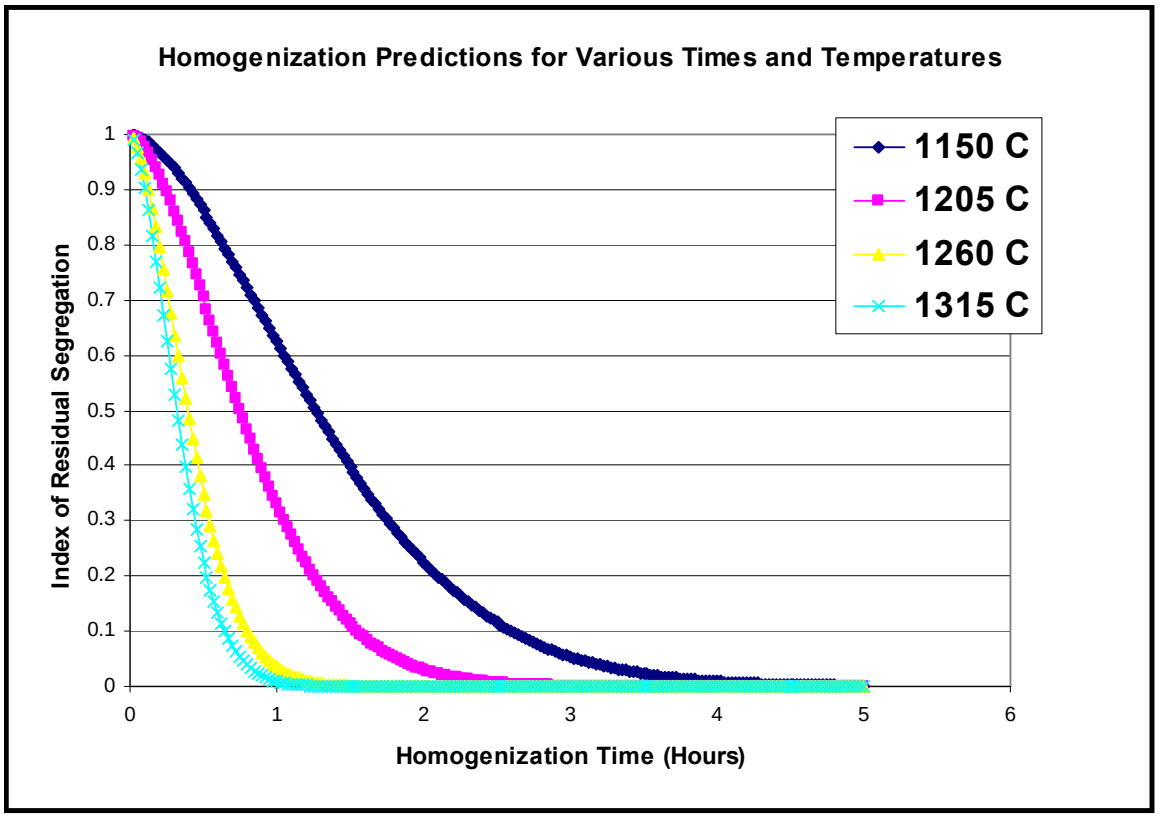

Figure 13 - Plot of index of residual segregation versus time showing that the amount of time to fully homogenize the structure decreases as the homogenization temperature increases. Full homogenization at 1150 °C requires 4 hours while homogenization at 1315 °C requires only 1 hour.

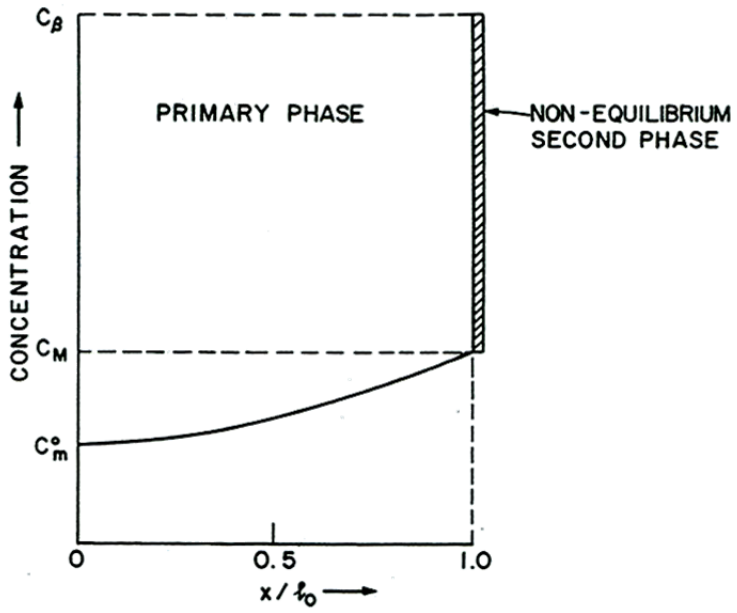

Figure 14 - Schematic representation of initial composition profile used in dissolution model.

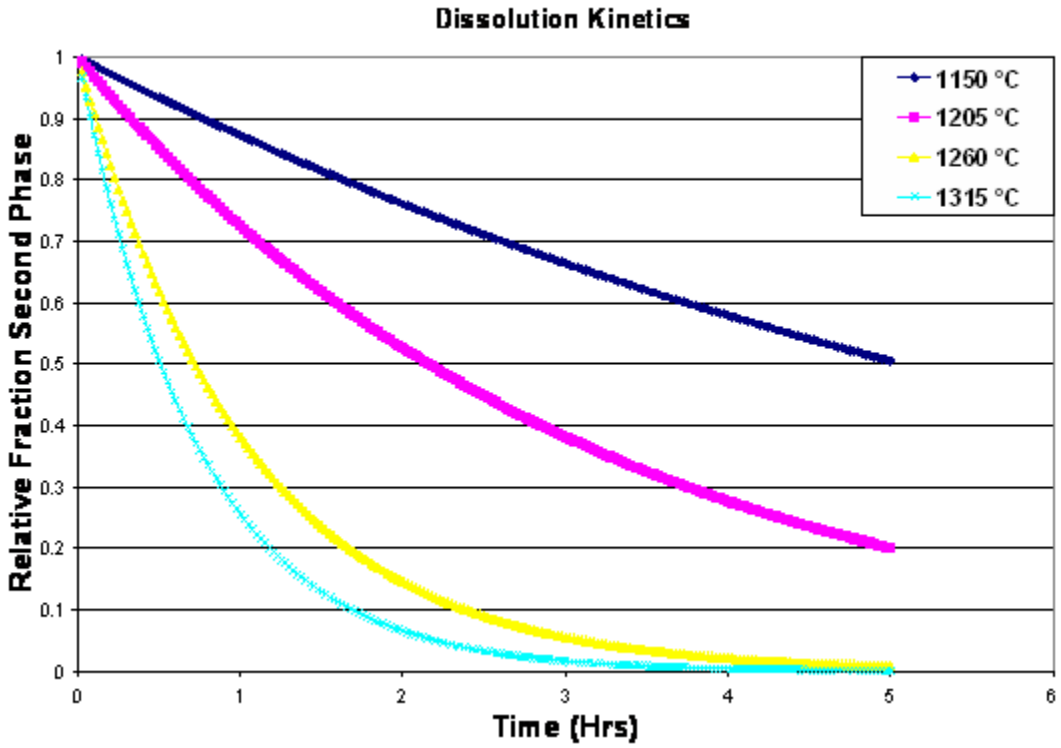

Figure 15 - Plot of relative fraction 2nd phase remaining versus dissolution heat treatment time. The amount of secondary phase decreases more rapidly with increasing temperature due to the increased solute diffusivity at elevated temperatures.

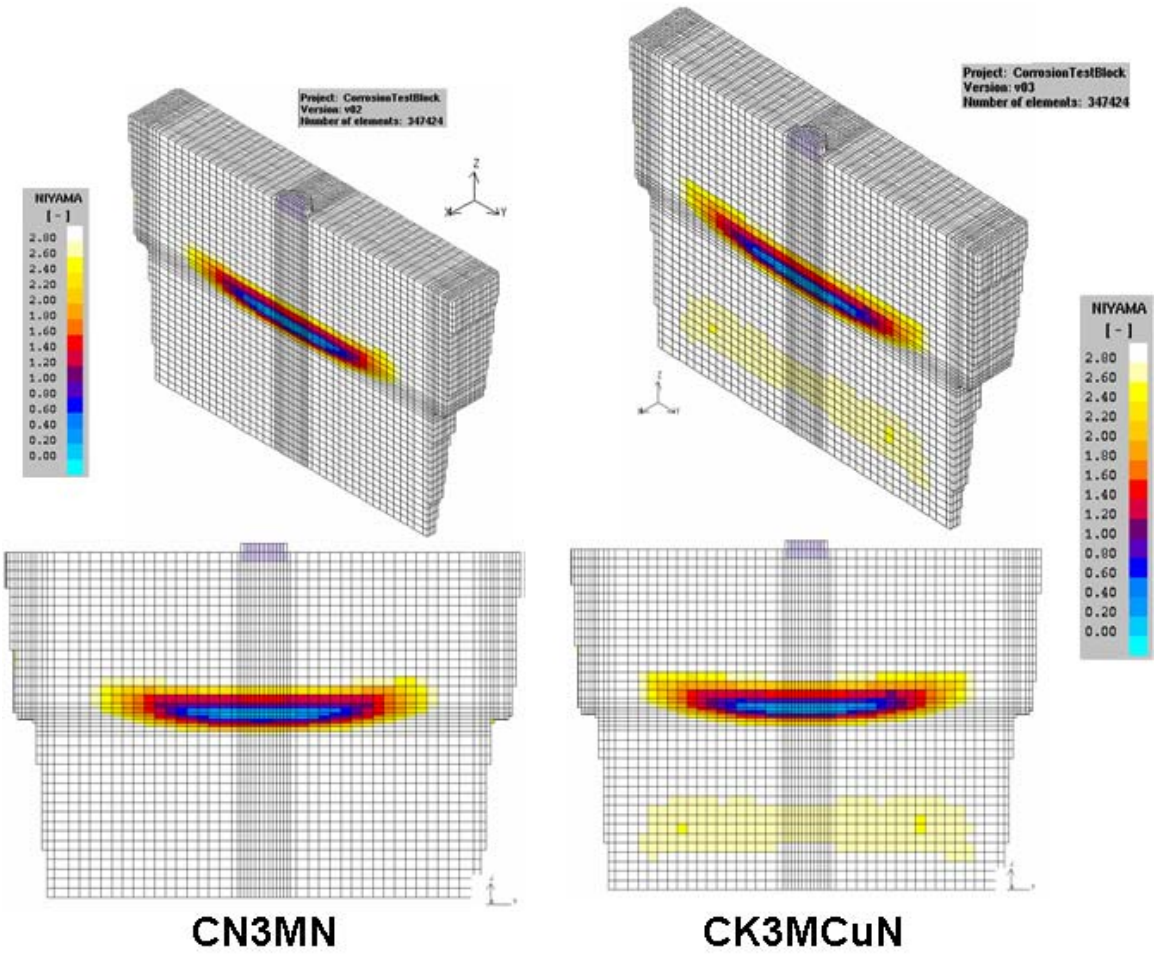

Figure 16 - Niyama simulation for CN3MN and CK3MCuN showing that the entire casting should be free of microporosity.

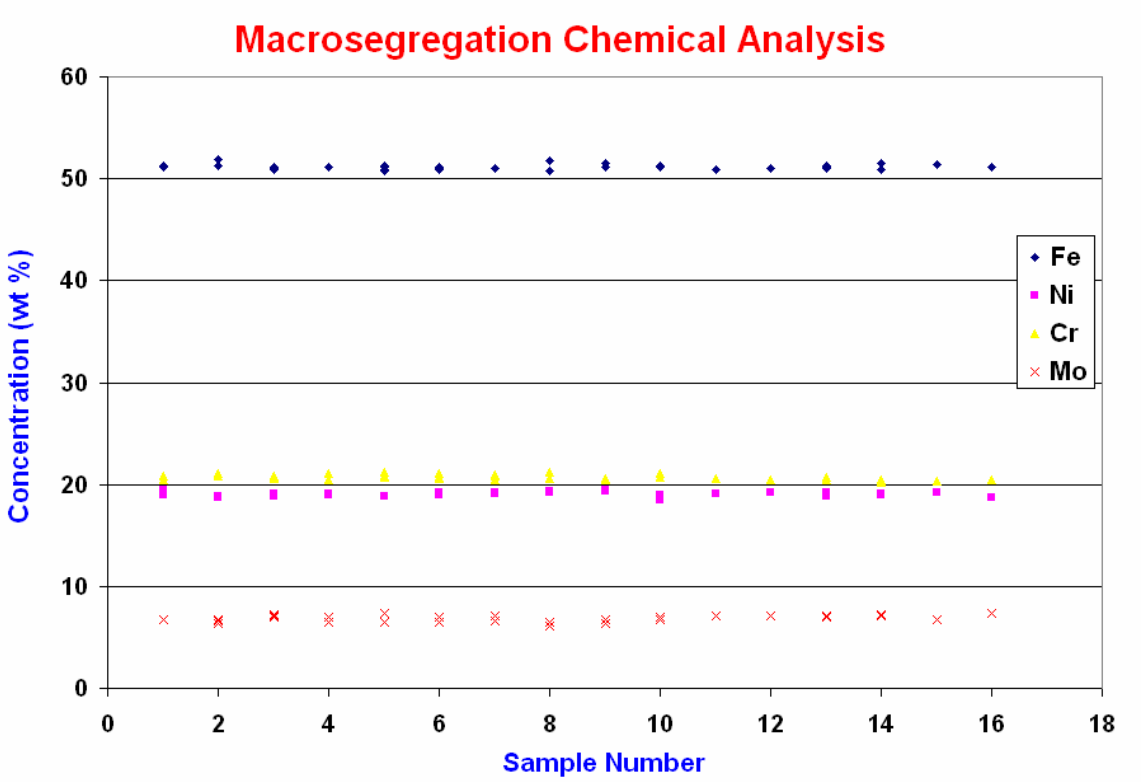

Figure 17 - Macrosegregation measurements performed on CK3MCuN bar where no significant change in chemical composition is observed along the length of the block.

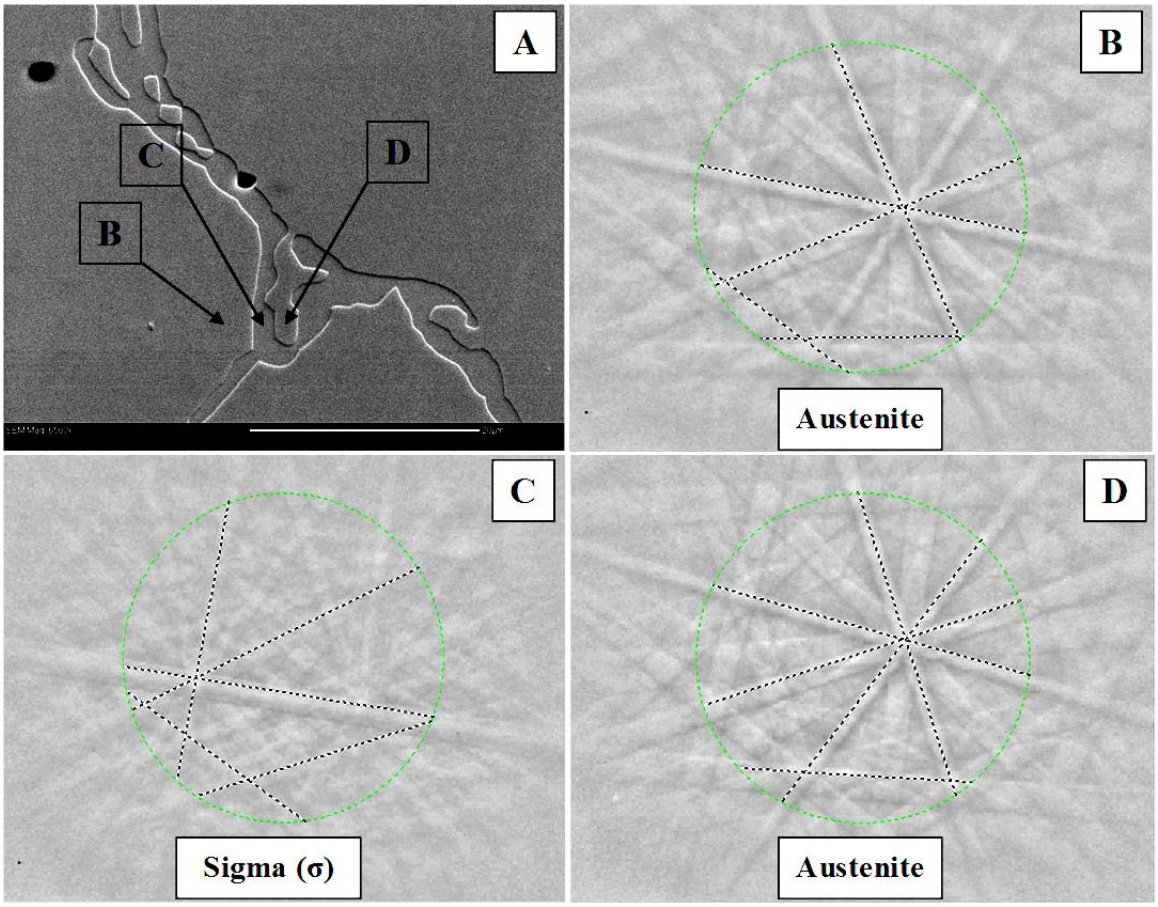

Figure 18 - (A) SEM micrograph of an (austenite + sigma) eutectic island inCK3MCuN after an 1150°C, 2 hour heat treatment showing regions where EBSD data was collected. EBSD pattern collected from (B) matrix which is indexed as austenite, (C) 2nd phase in eutectic island indexed as sigma phase. (D) Primary phase in eutectic island indexed as austenite.

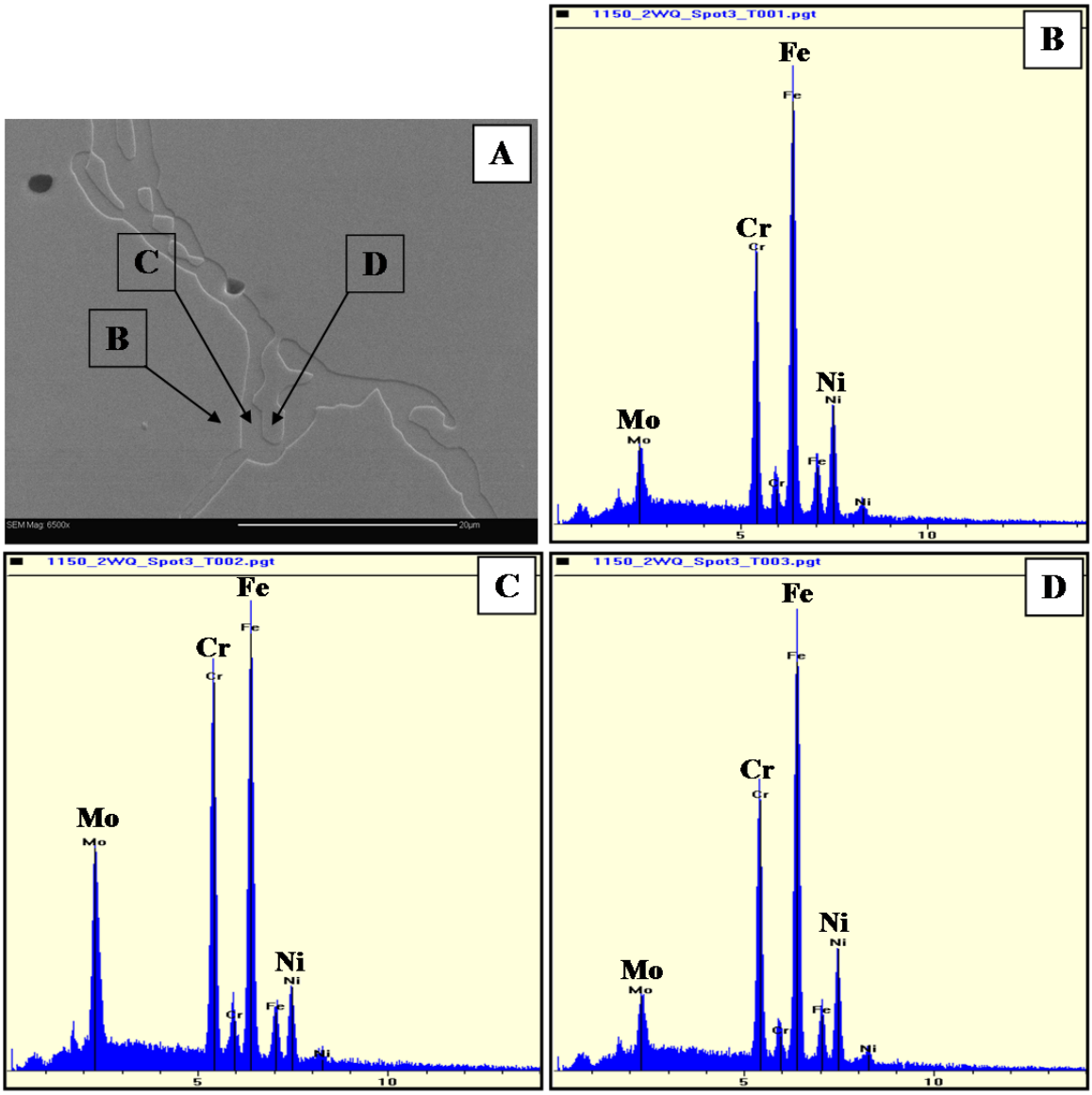

Figure 19 - (A) SEM micrograph of an (austenite + sigma) eutectic island inCK3MCuN after an 1150°C, 2 hour heat treatment showing regions where XEDS data was collected. XEDS data collected from (B) the austenitic matrix, (C) sigma phase in eutectic island, and (D) eutectic austenite.

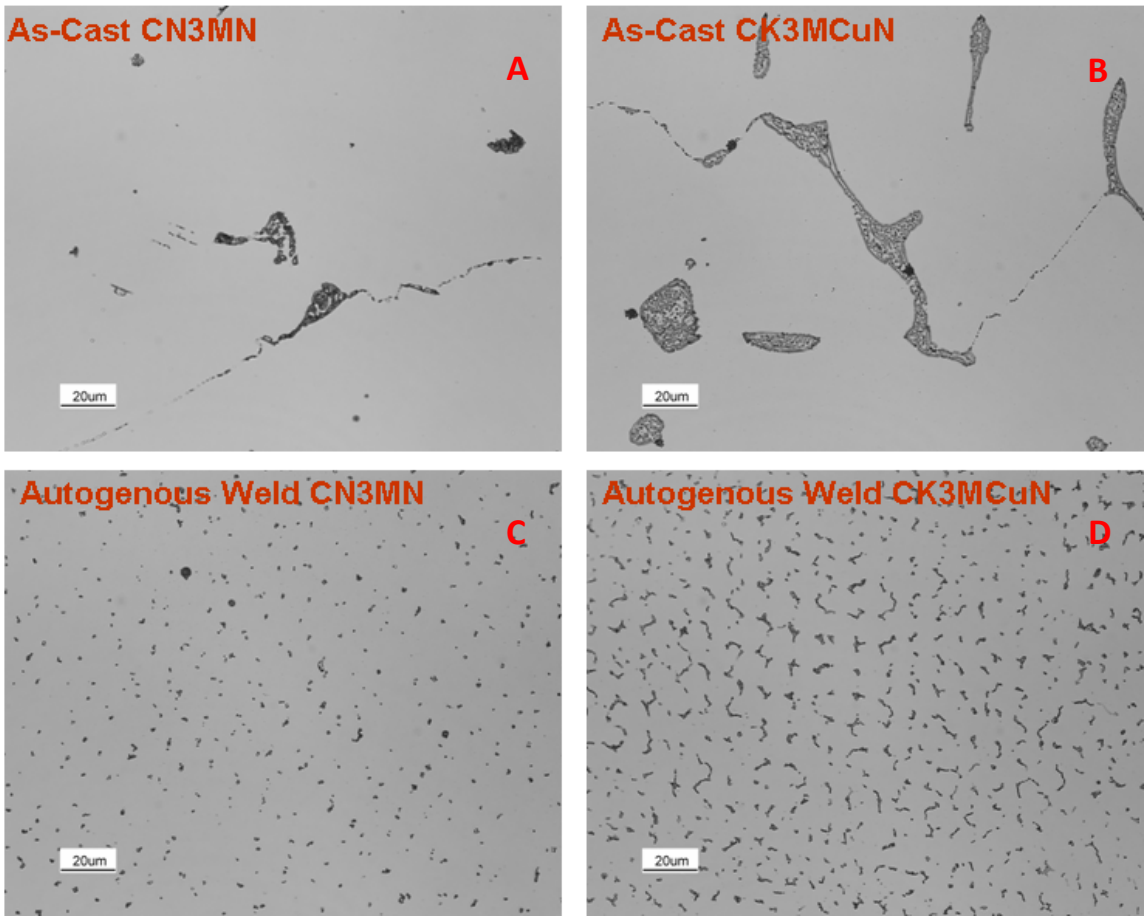

Figure 20 - LOM micrographs of as-cast and as-welded CN3MN and CK3MCuN showing the starting microstructure of austenite with interdendritic (austenite + sigma) eutectic islands.

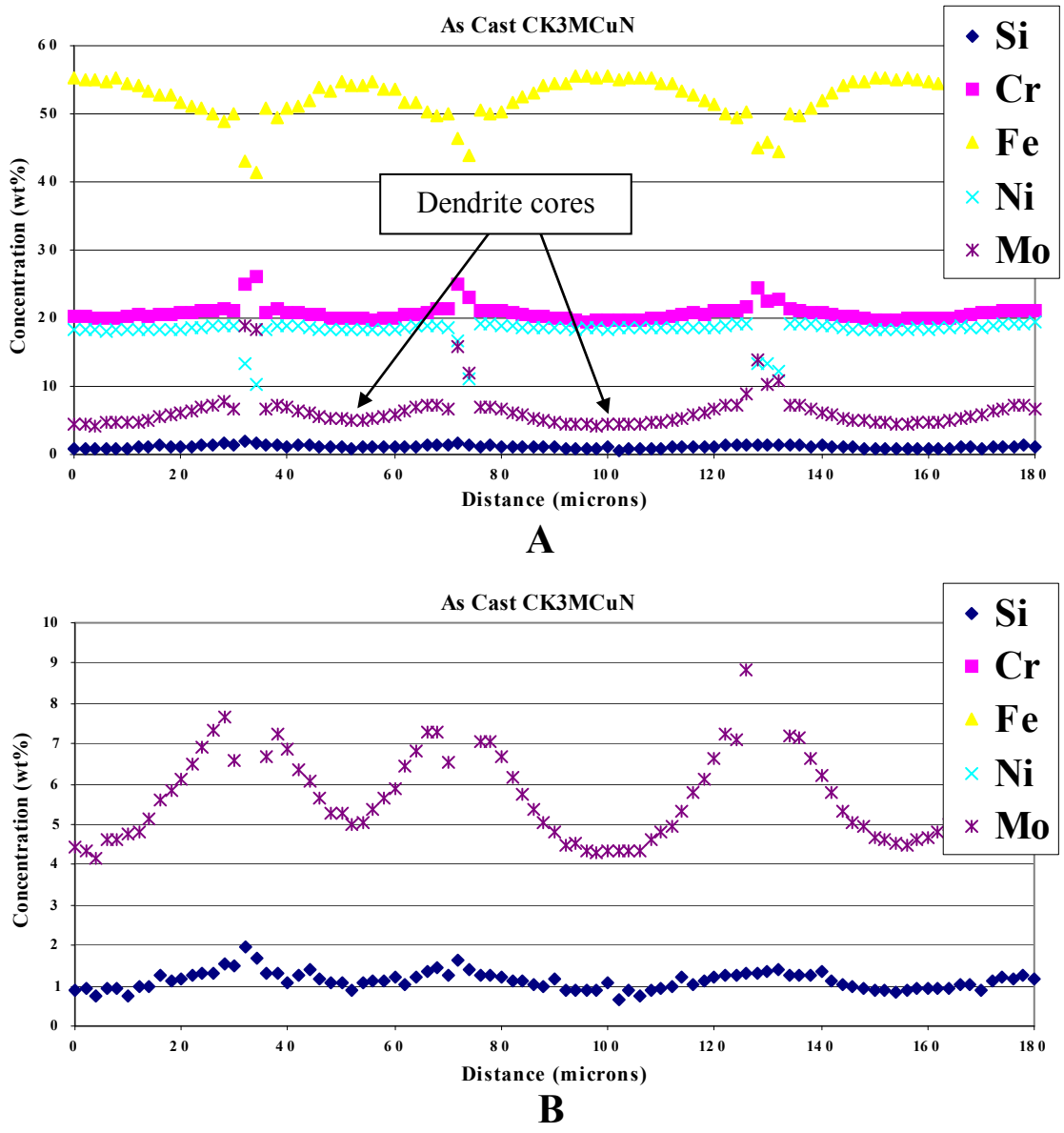

Figure 21 - A) EPMA trace across several dendrites in as-cast CK3MCuN showing significant microsegregation from the dendrite cores to interdendritic regions. B) Enlarged view of the 0-10 wt% region showing the variation of Mo as a function of distance.

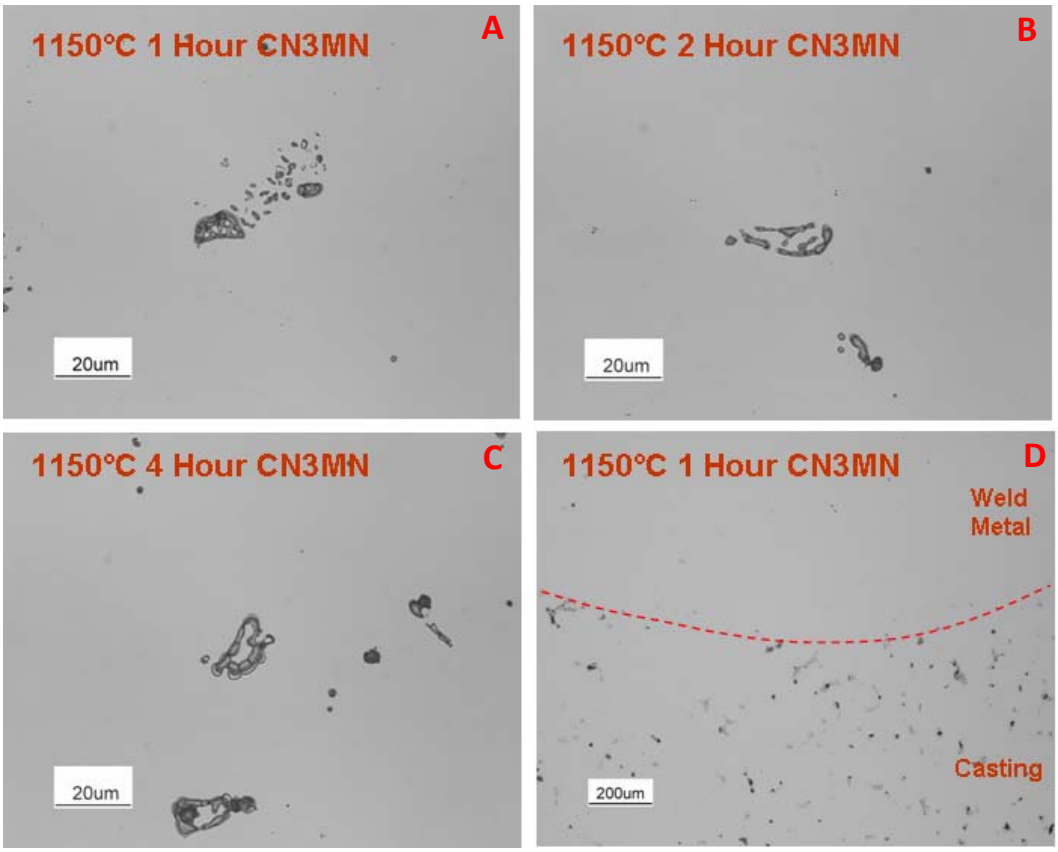

Figure 22 - LOM micrographs of CN3MN heat treated at 1150°C for 1, 2, and 4 hours. Only small amounts of dissolution are achieved in the cast material after 4 hours while near complete dissolution of the sigma phase occurs after only 1 hour in the weld due to the decreased dendrite arm spacing.

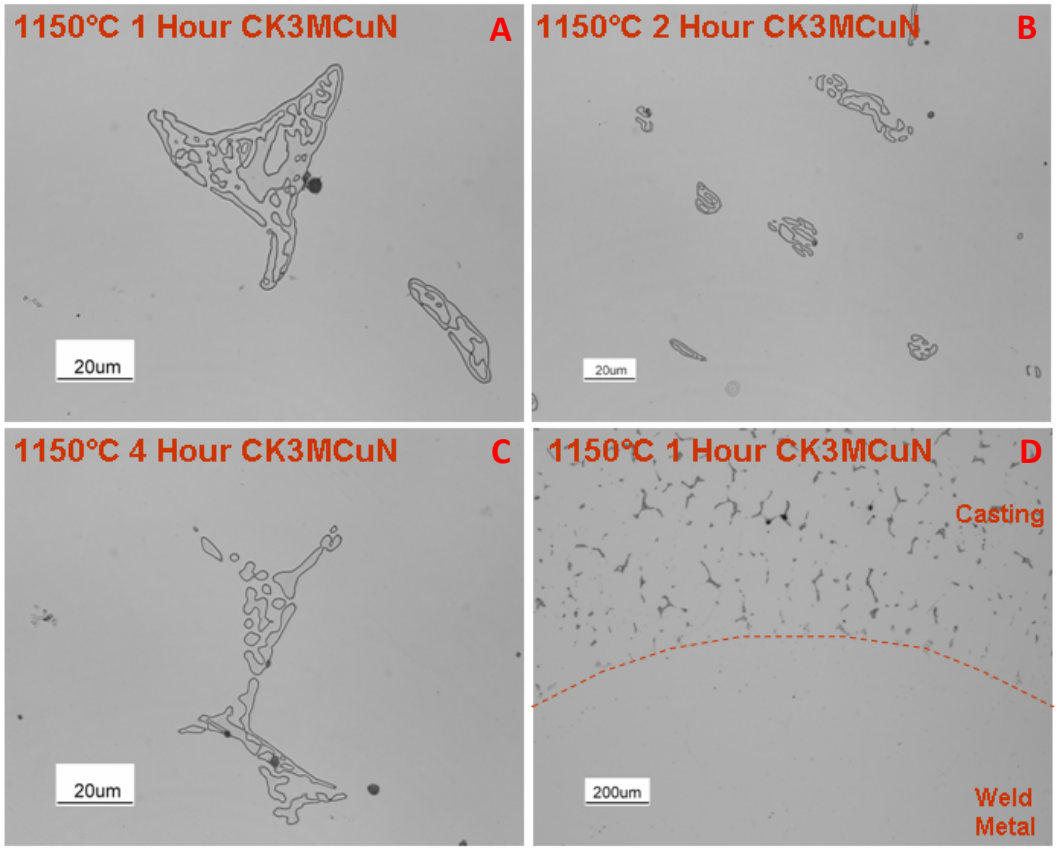

Figure 23 - LOM micrographs on CK3MCuN heat treated at 1150°C for 1, 2, and 4 hours. Only small amounts of dissolution are achieved in the cast material after 4 hours while near complete dissolution of the sigma phase occurs after only 1 hour in the weld due to the decreased dendrite arm spacing.

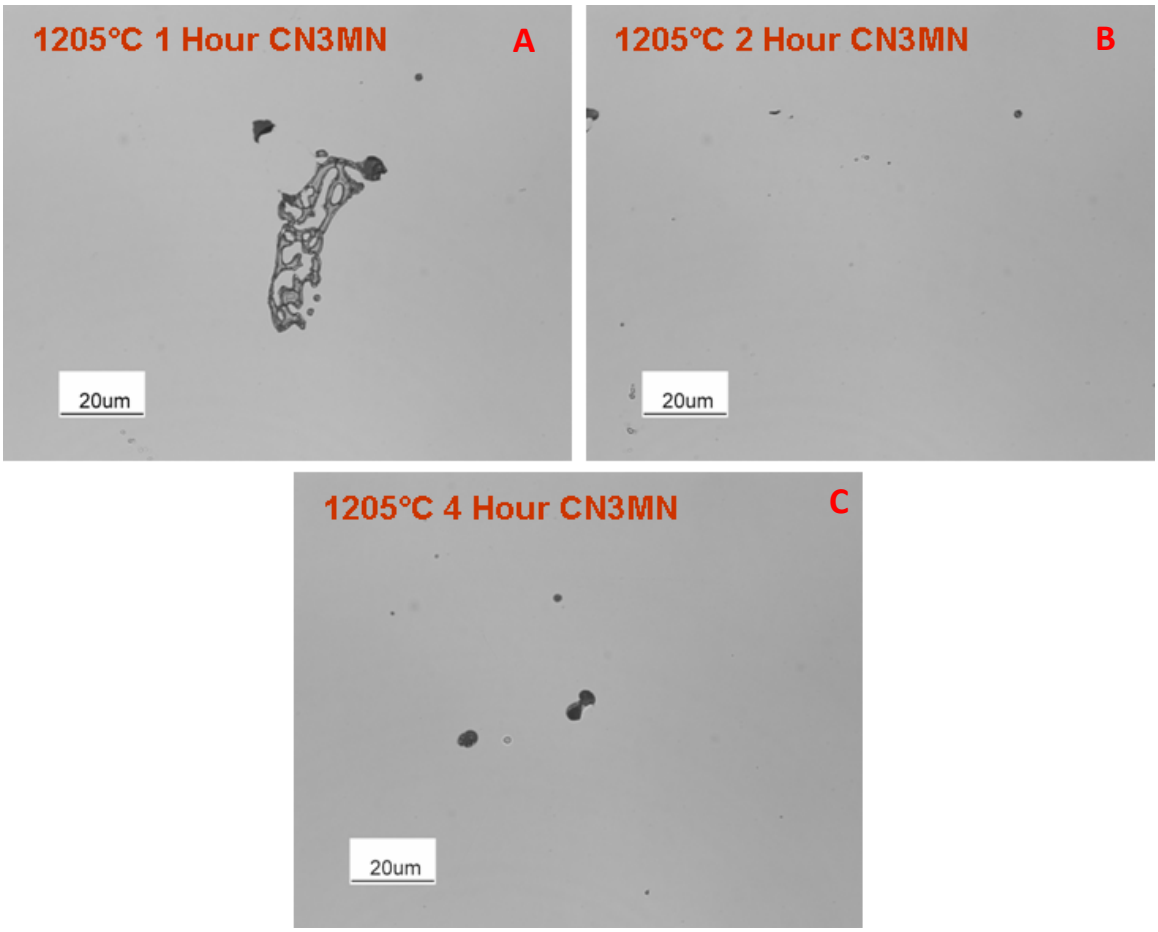

Figure 24 - LOM micrographs of CN3MN heat treated at 1205°C for 1, 2, and 4 hours. Significant dissolution seems to occur after 4 hours.

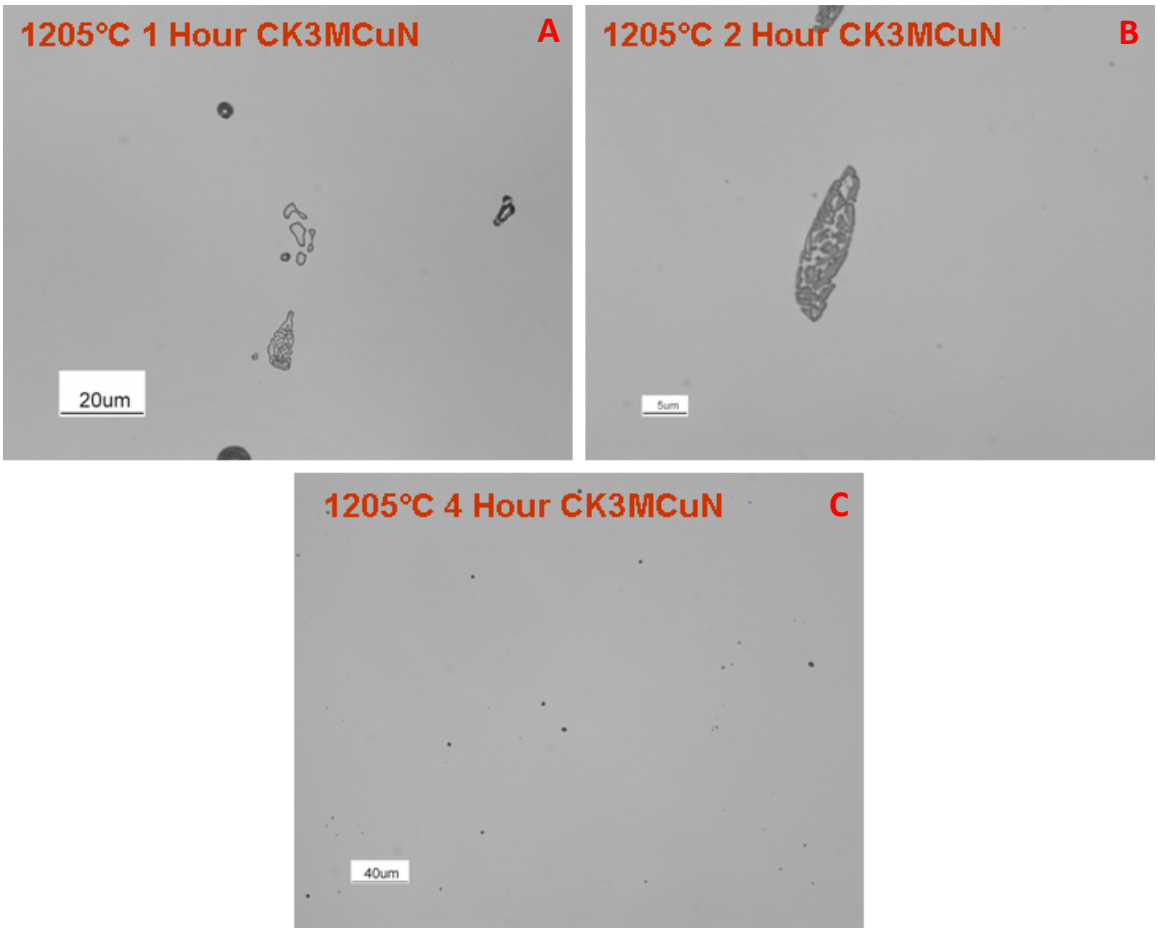

Figure 25 - LOM micrographs of CK3MCuN heat treated at 1205°C for 1, 2, and 4 hours. Significant dissolution seems to occur after 4 hours.

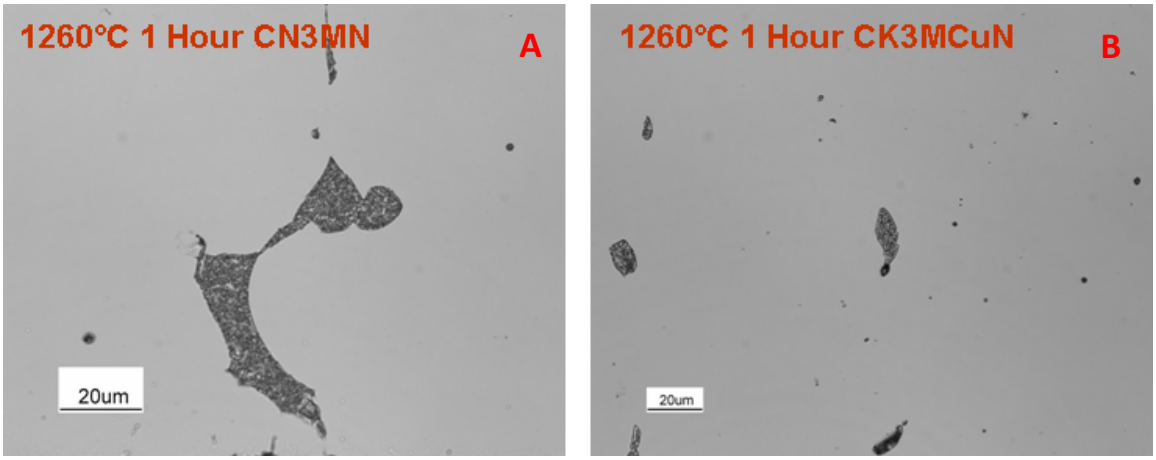

Figure 26 - LOM micrographs of CN3MN and CK3MCuN heat treated at 1260°C for 1 hour. Dissolution is not occurring at these temperatures because partial melting of the interdendritic regions is occurring.

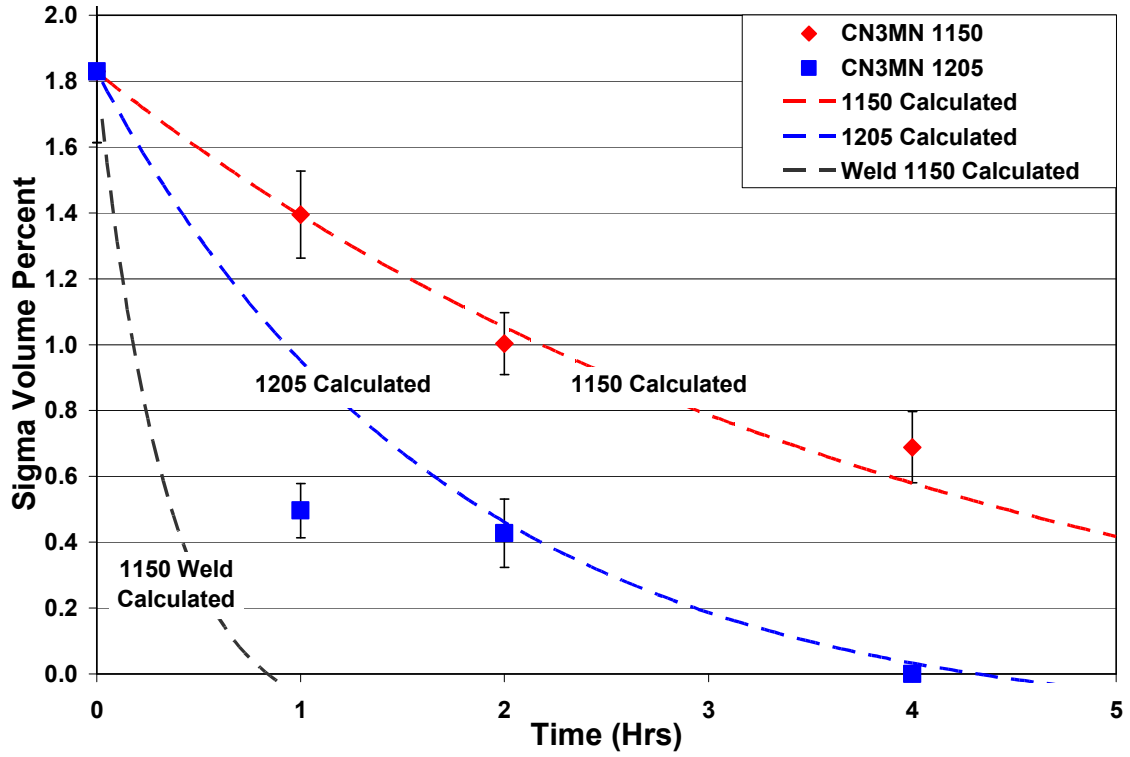

Figure 27 - Measured and calculated volume fraction sigma phase in CN3MN after heat treatment at 1150°C and 1205°C.

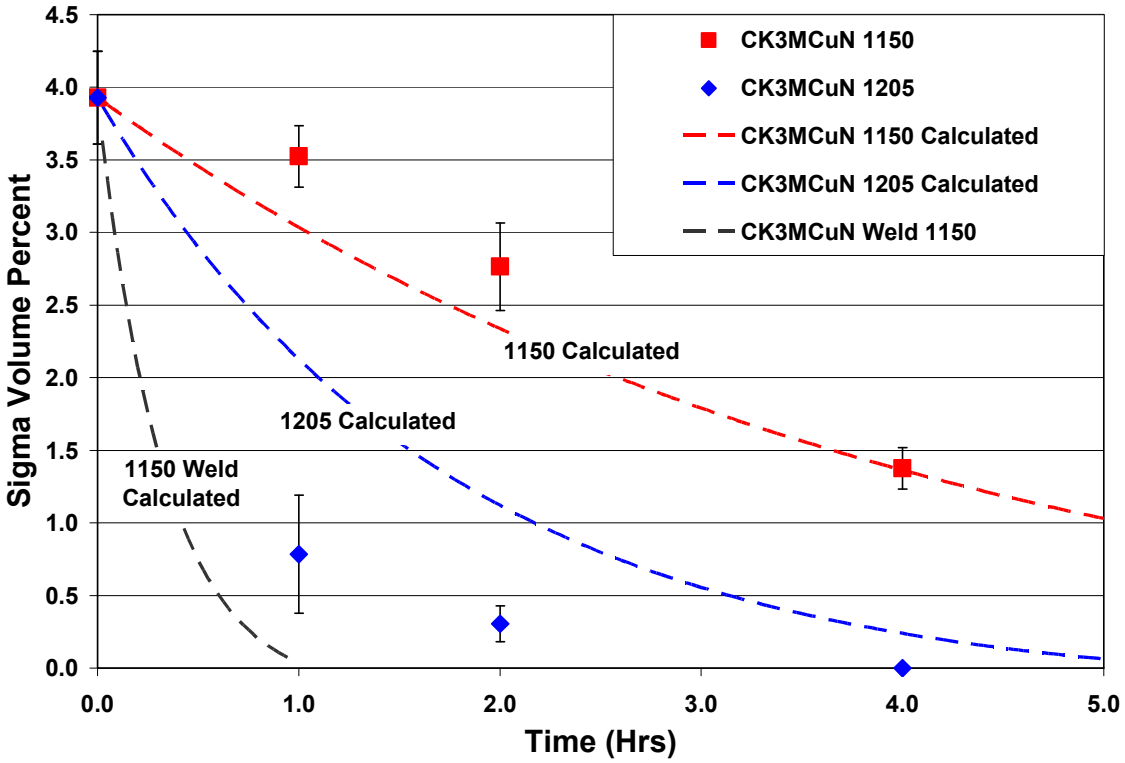

Figure 28 - Measured and calculated volume fraction sigma phase in CK3MCuN after heat treatment at 1150°C and 1205°C.

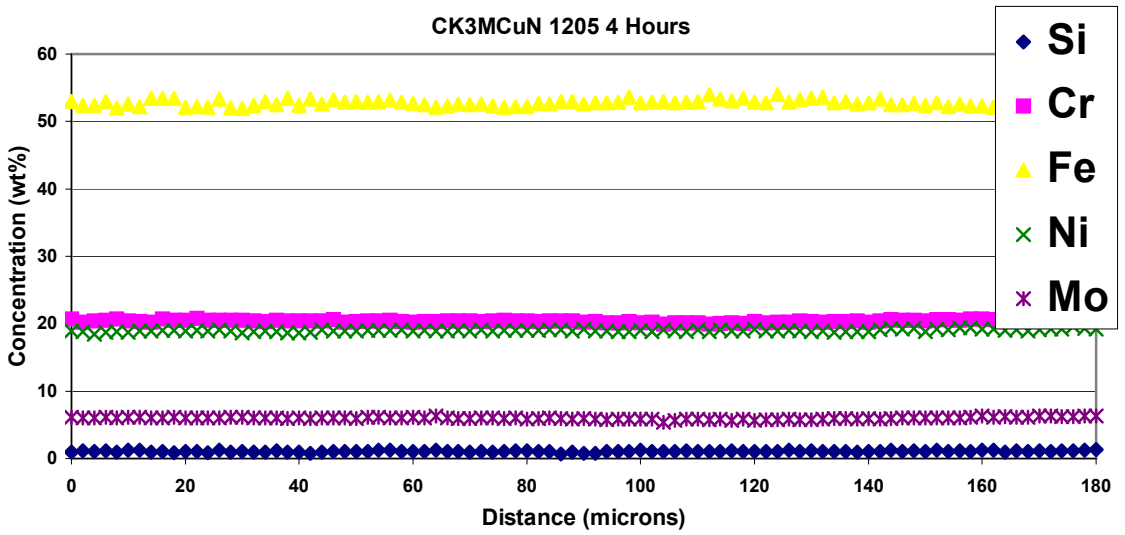

Figure 29 -EPMA trace across an austenite grain in CK3MCuN after 1205°C / 4 hour heat treatment showing little or no remnant microsegregation indicative of near complete homogenization.

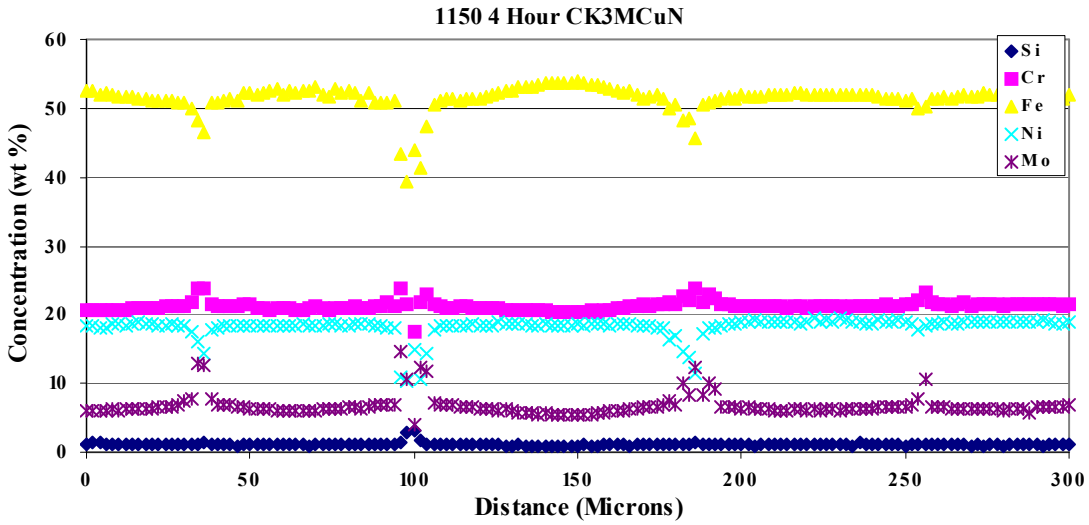

Figure 30 - EPMA trace across dendrites in CK3MCuN that have been heat treated at 1150 °C for 4 hours. The degree of microsegregation has only decreased slightly over the as-cast condition.

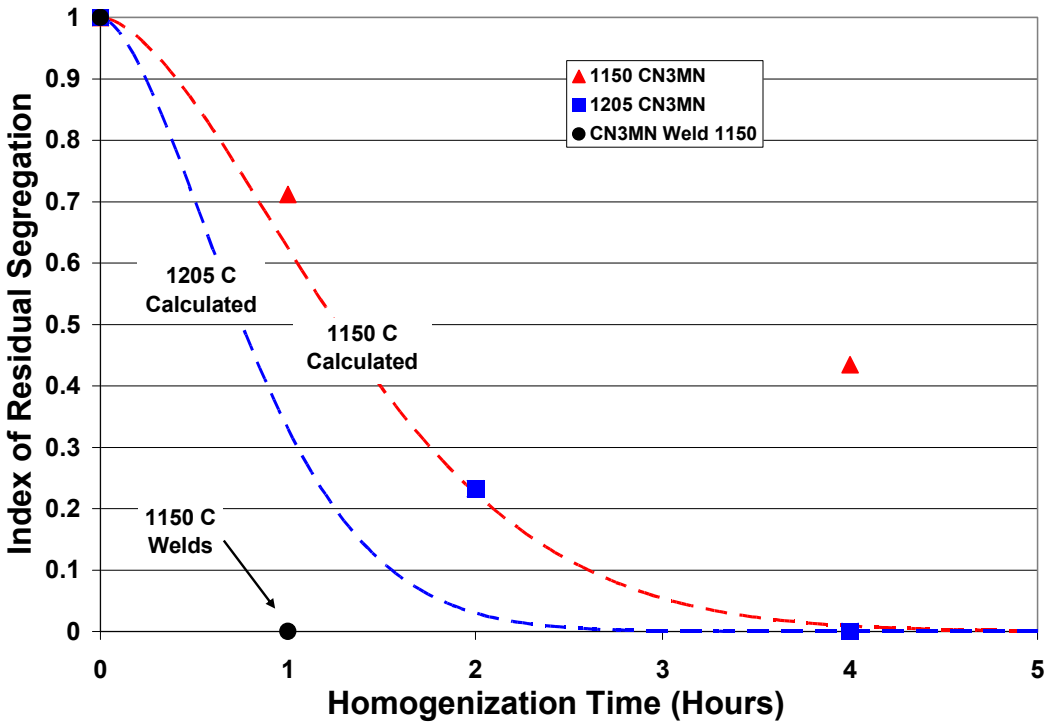

Figure 31 - Plot of experimental and calculated index of residual segregation for alloy CN3MN after homogenization heat treatments at 1150°C and 1205°C.

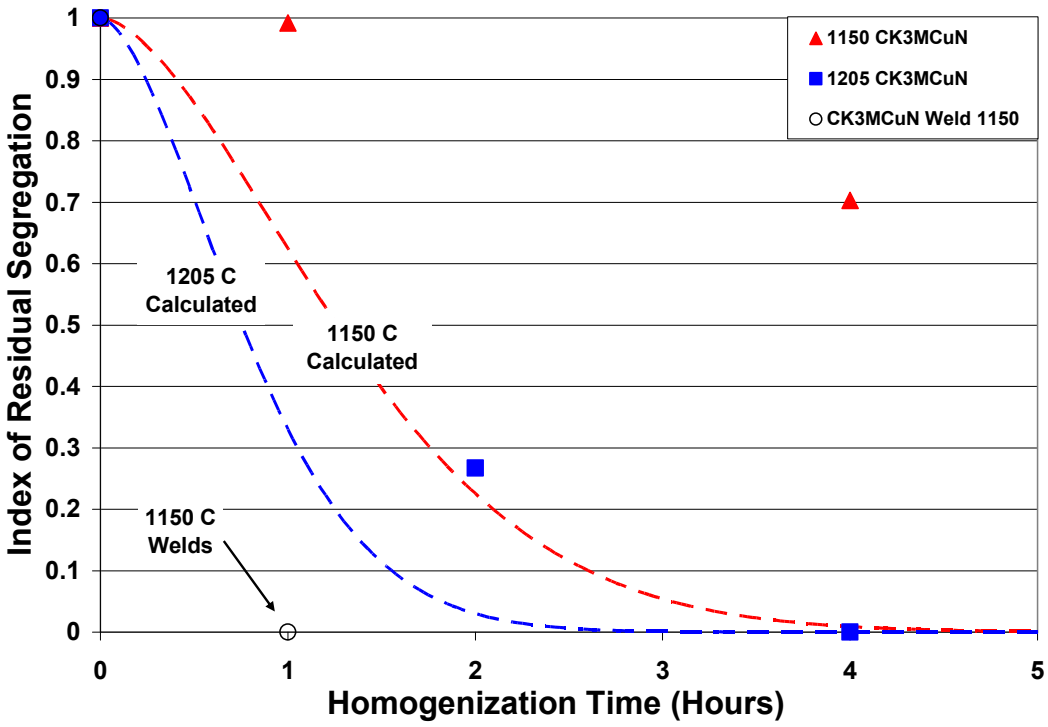

Figure 32 - Plot of experimental and calculated index of residual segregation for alloy CK3MCuN after homogenization heat treatments at 1150°C and 1205°C.

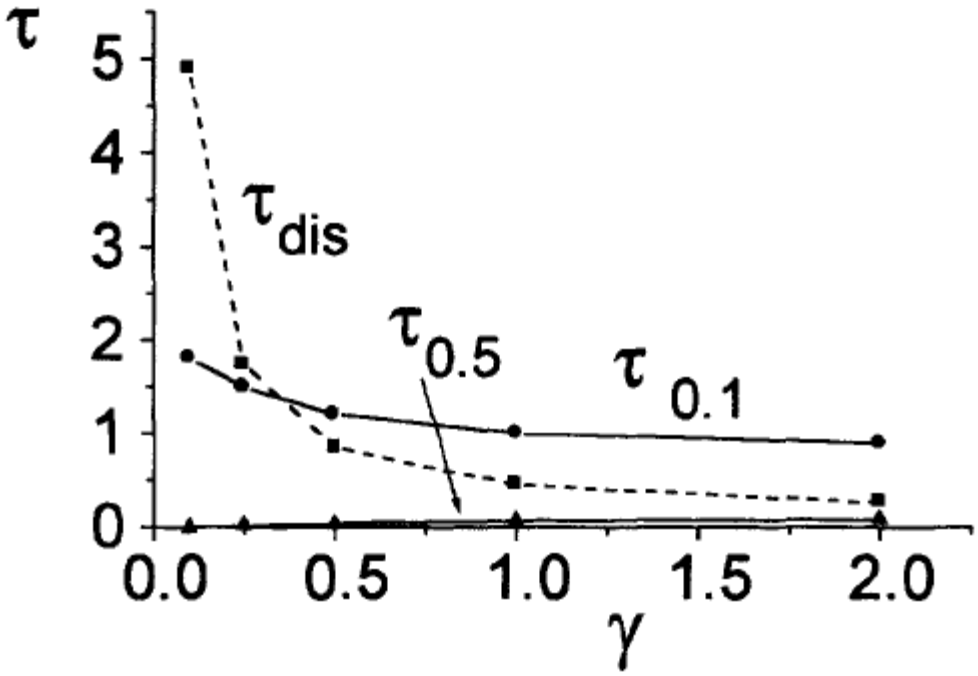

Figure 33 - Plot of dimensionless time, τ, versus supersaturation, γ, for dissolution and for near complete homogenization.

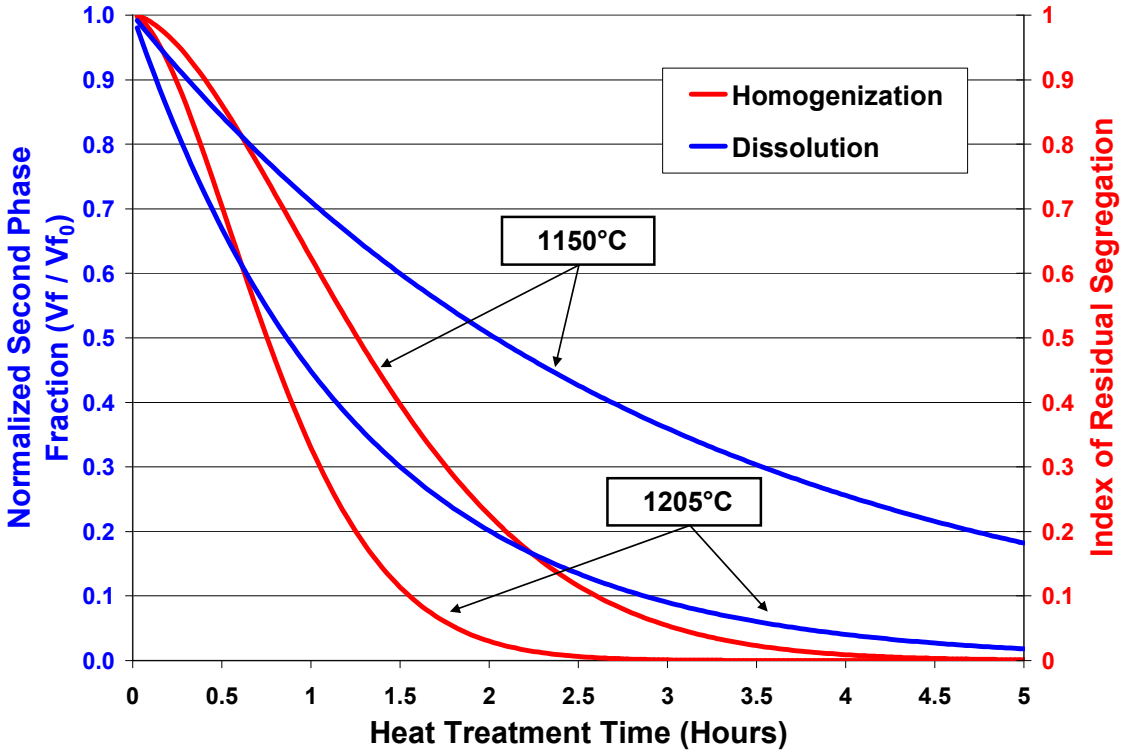

Figure 34 - Plot of homogenization versus dissolution kinetics showing that for a given temperature, the time required for homogenization is significantly shorter than for dissolution

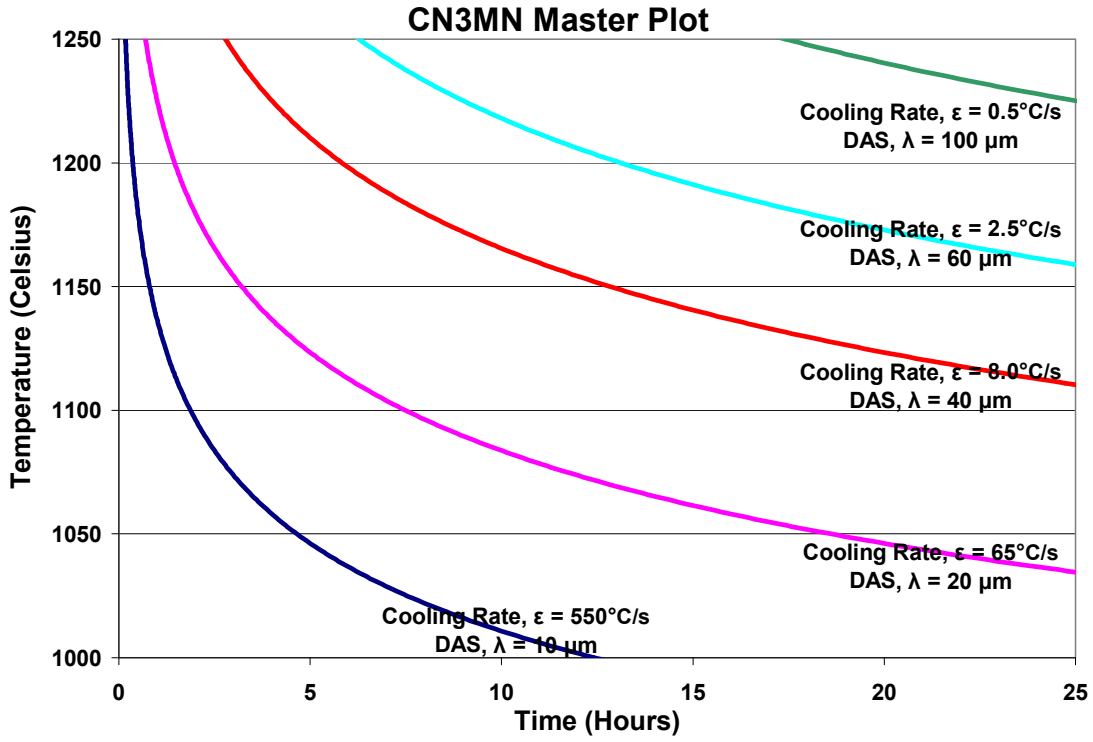

Figure 35 - Master heat treatment curve for various cooling rate / dendrite arm spacing combinations for CN3MN.

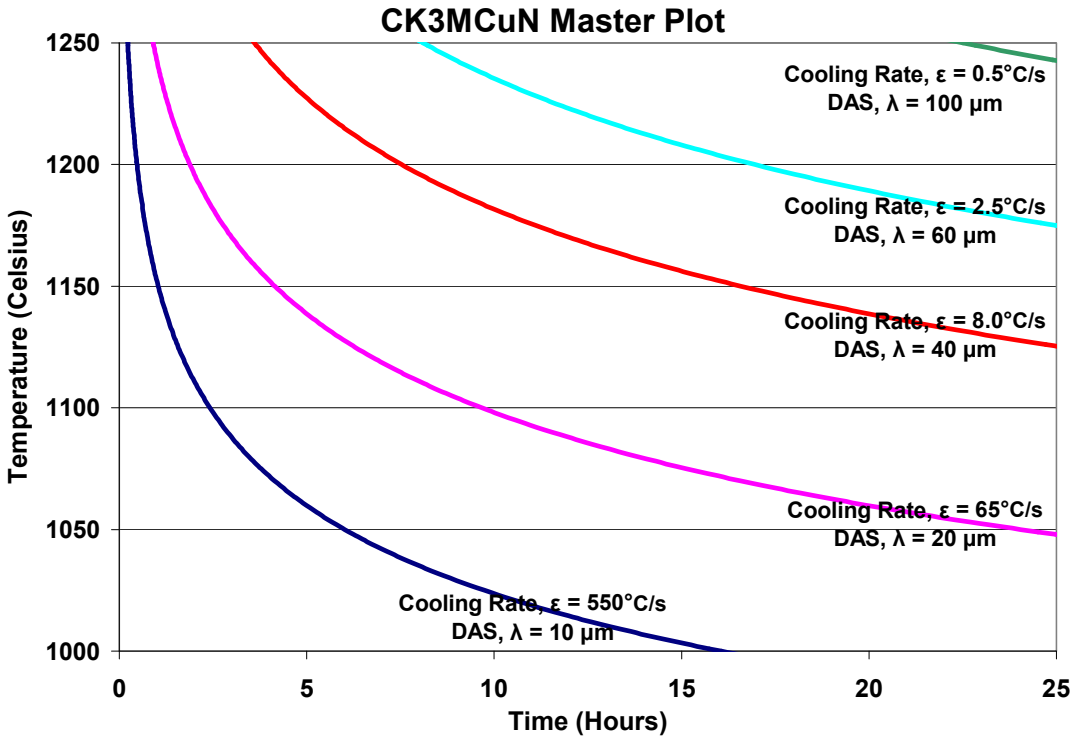

Figure 36 - Master heat treatment curve for various cooling rate / dendrite arm spacing combinations for CK3MCuN.

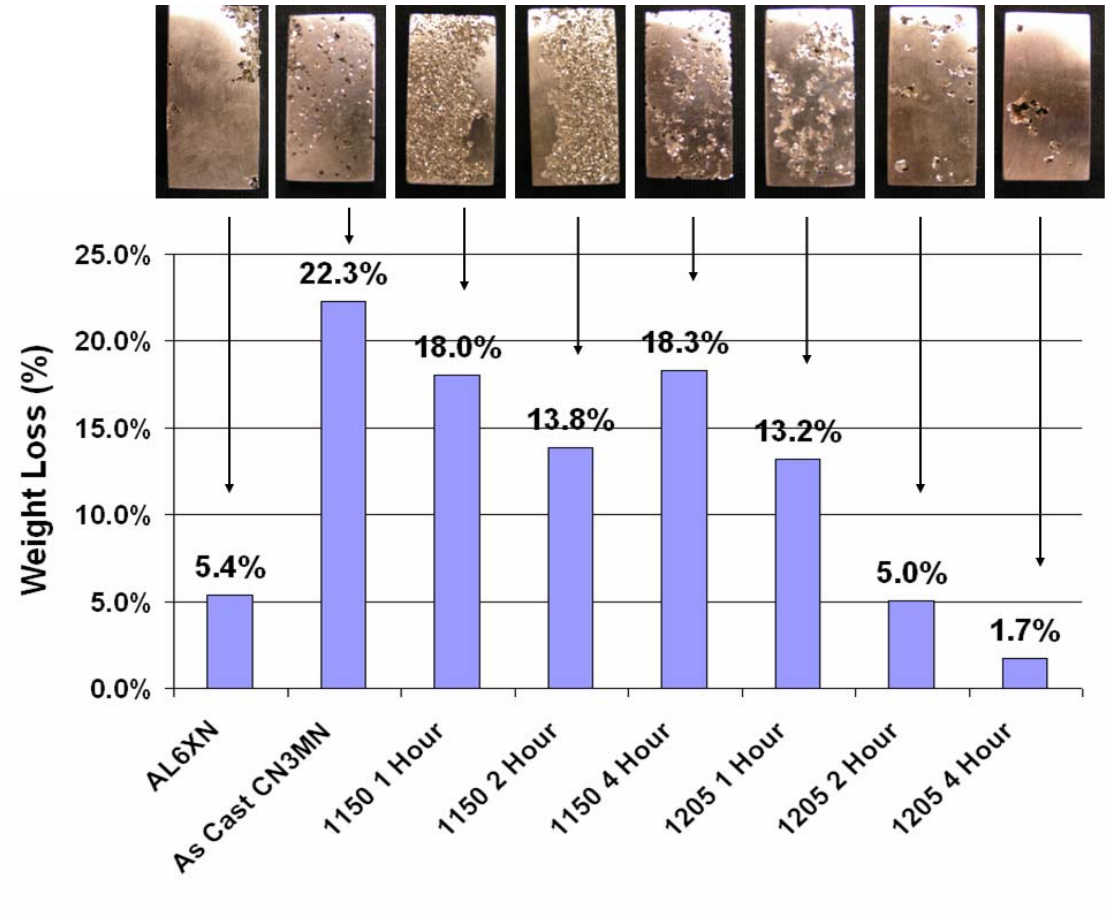

Figure 37 - Results of ASTM G48 Method A testing for CN3MN and its wrought counterpart AL6XN.

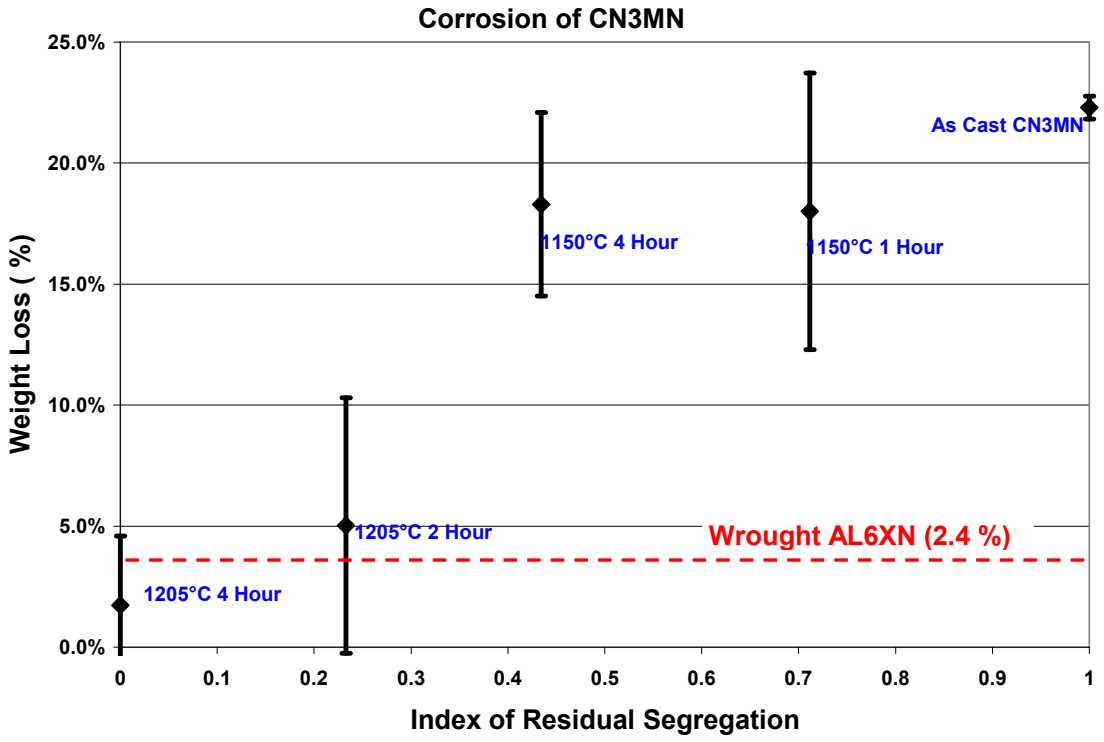

Figure 38 - Corrosion resistance as a function of achieved levels of homogenization in CN3MN after various heat treatments.

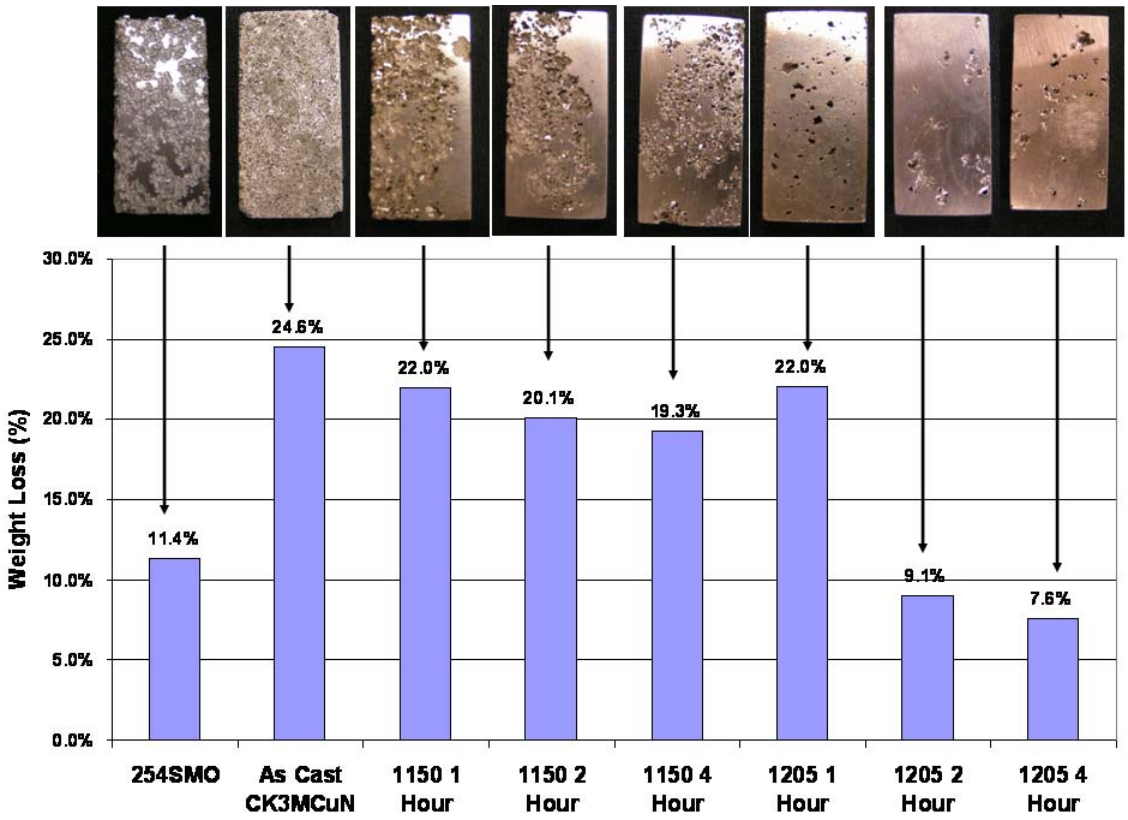

Figure 39 - Results of ASTM G48 Method A testing for CK3MCuN and its wrought counterpart 254SMO.

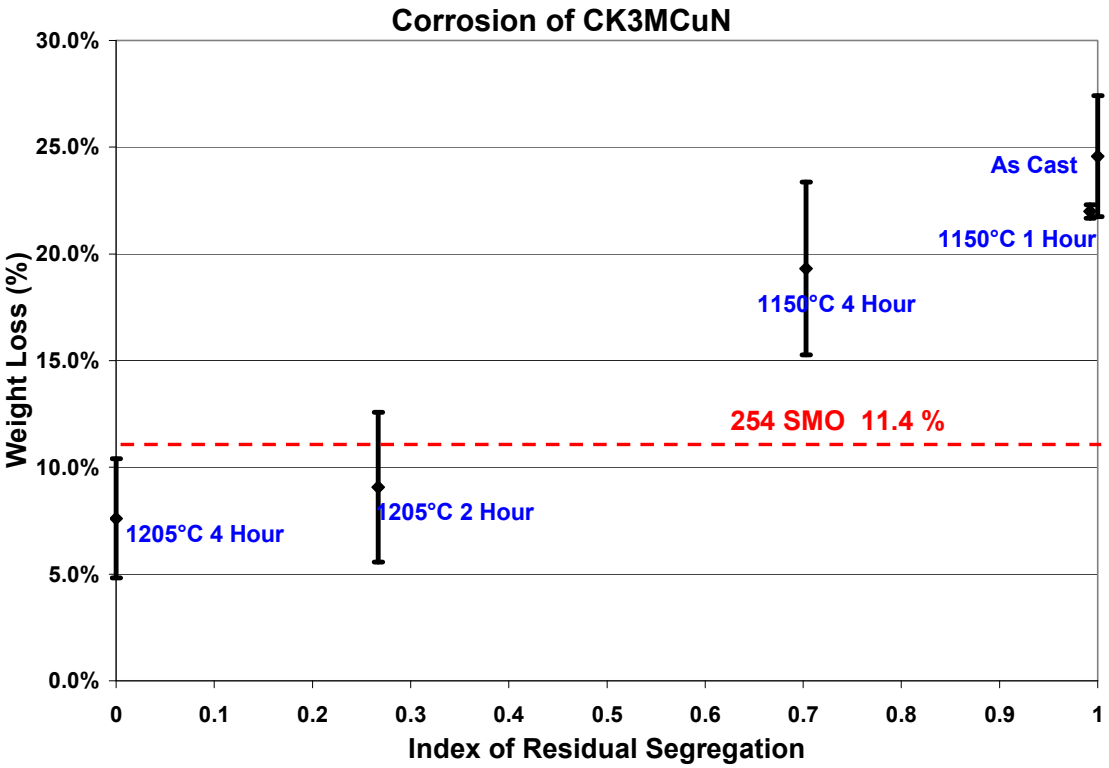

Figure 40 - Corrosion resistance as a function of achieved levels of homogenization in CK3MCuN after various heat treatments.

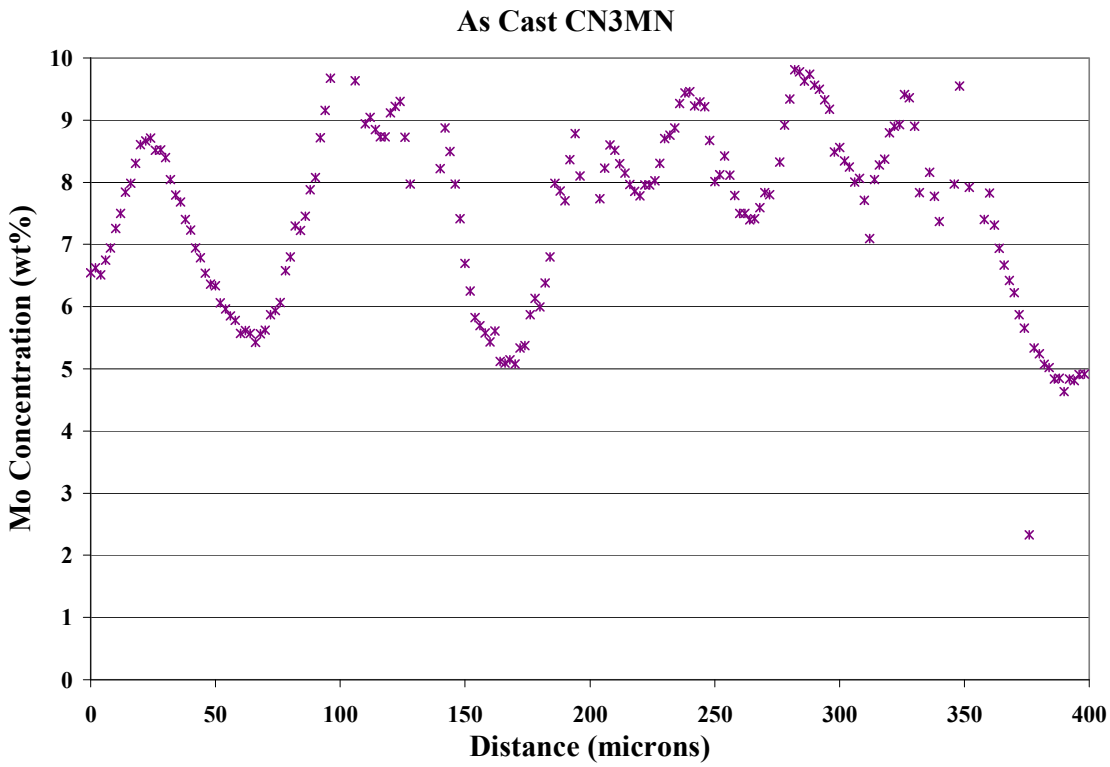

Figure 41 - Mo Concentration as a function of distance in As-Cast CN3MN

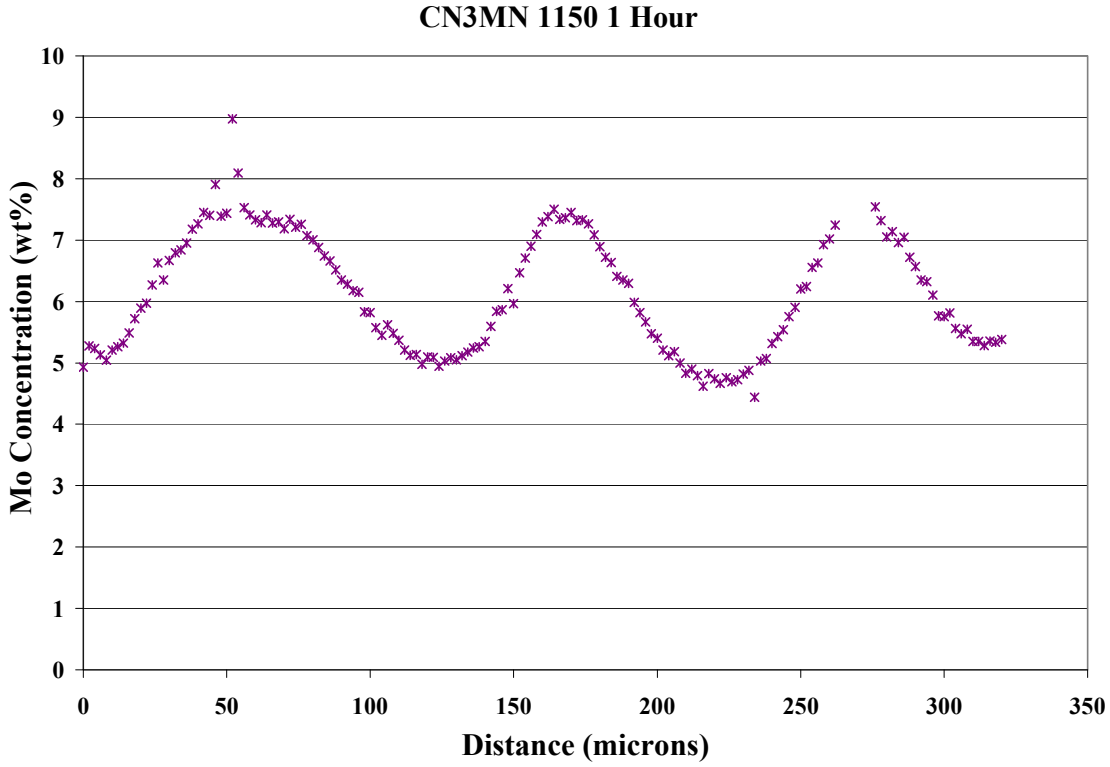

Figure 42 - Mo Concentration as a function of distance in CN3MN heat treated at 1150°C for 1 hour.

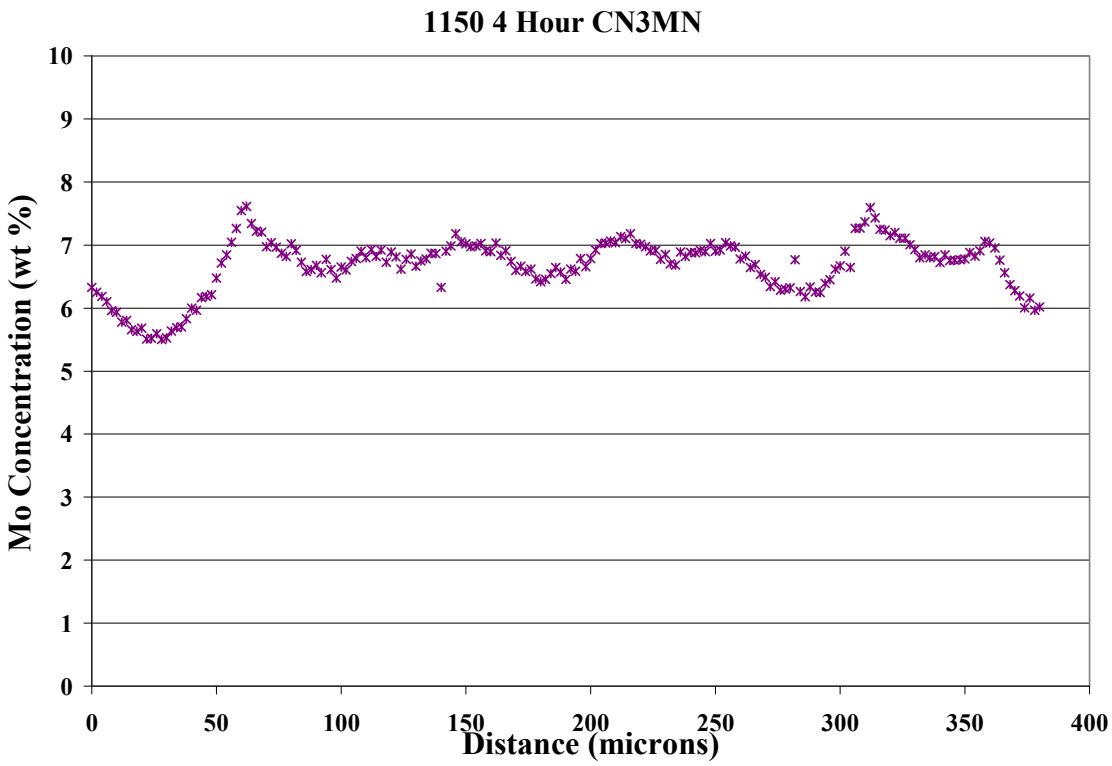

Figure 43 - Mo Concentration as a function of distance in CN3MN heat treated at 1150°C for 4 hours.

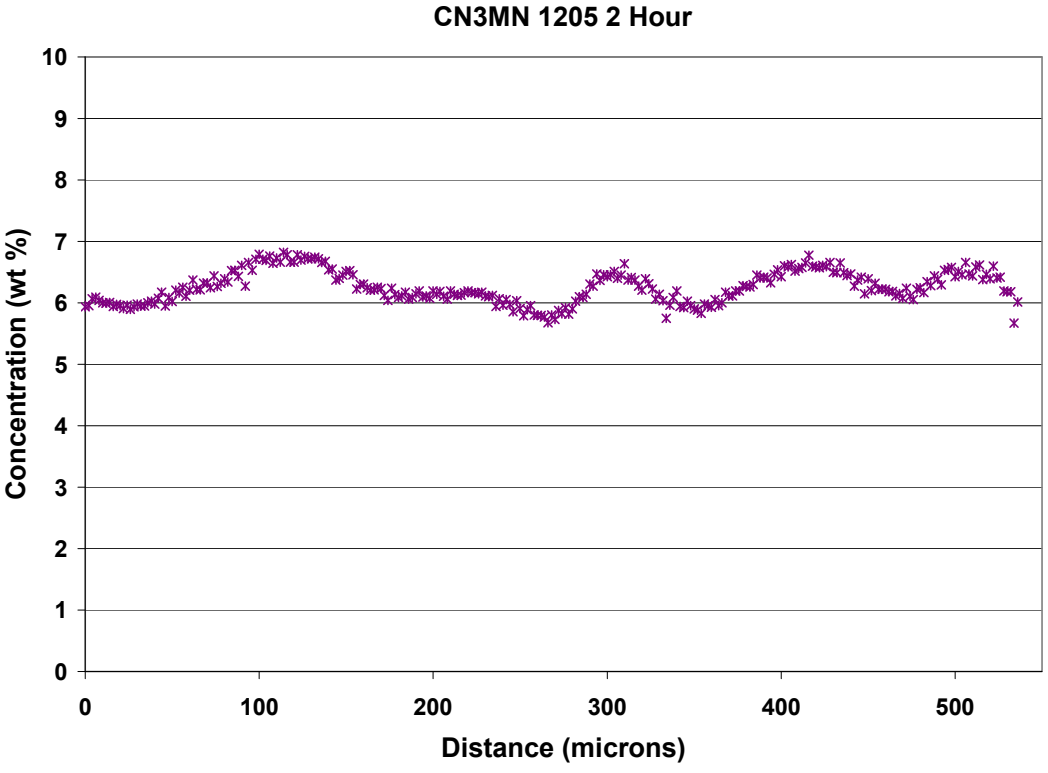

Figure 44 - Mo Concentration as a function of distance in CN3MN heat treated at 1205°C for 2 hours.

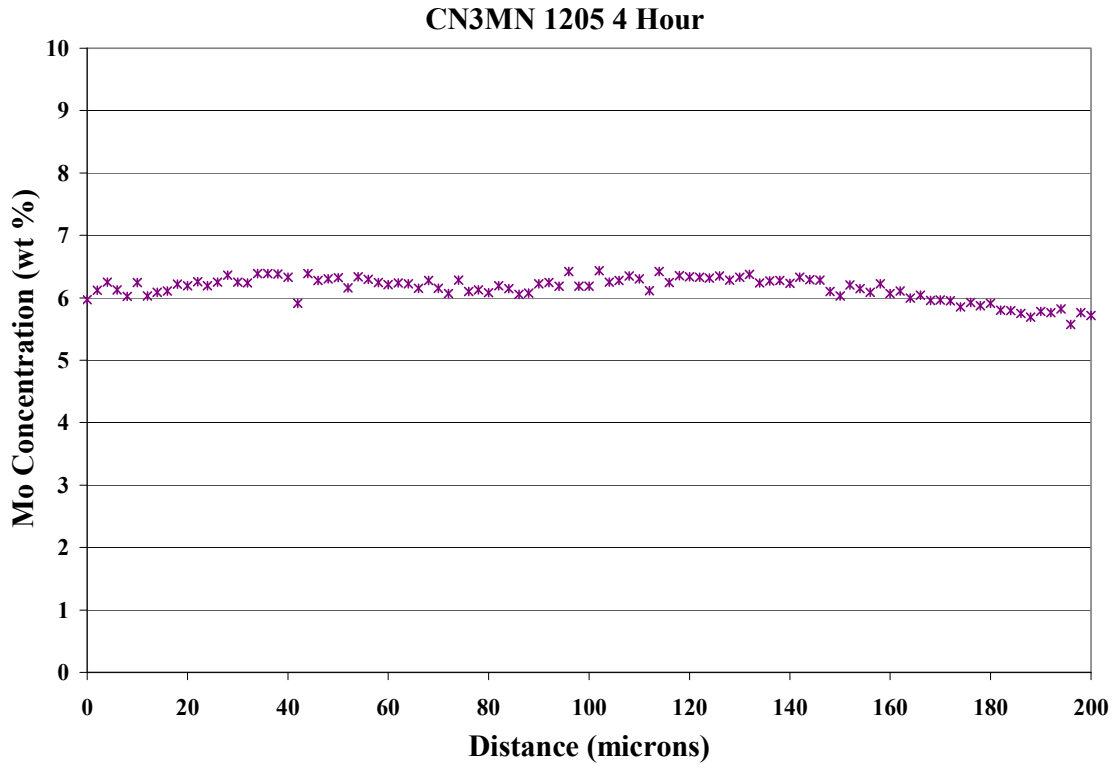

Figure 45 - Mo Concentration as a function of distance in CN3MN heat treated at 1205°C for 4 hours.

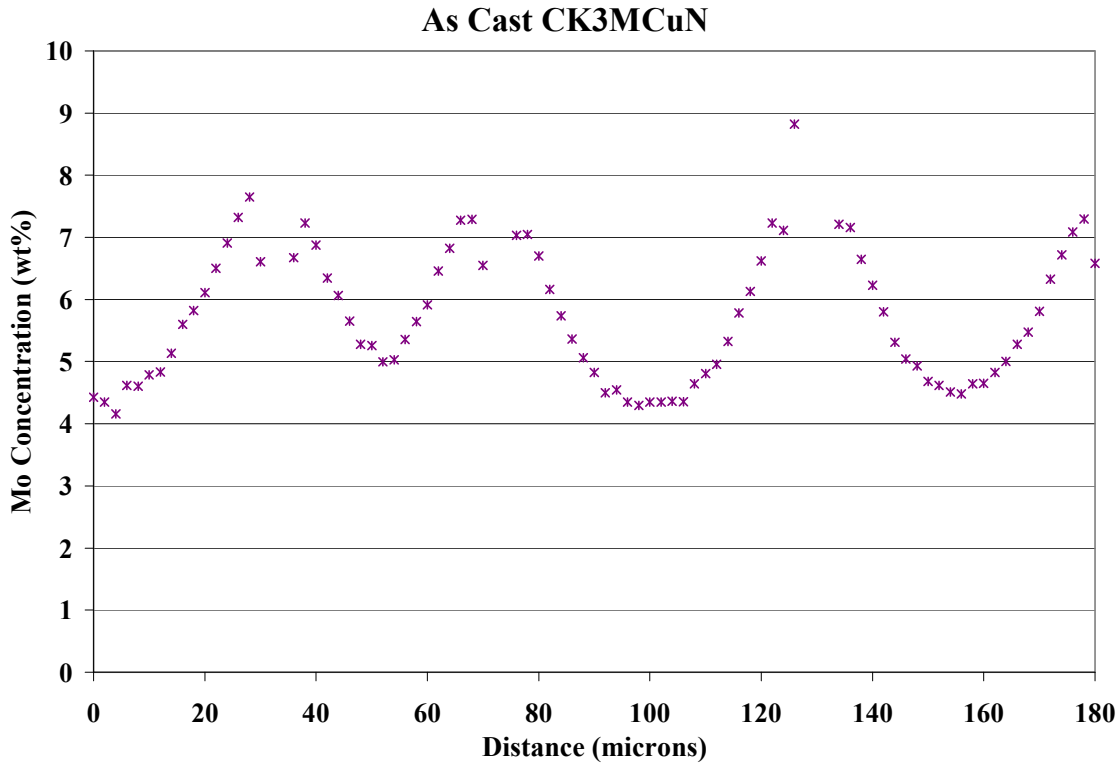

Figure 46 - Mo Concentration as a function of distance in As-Cast CK3MCuN

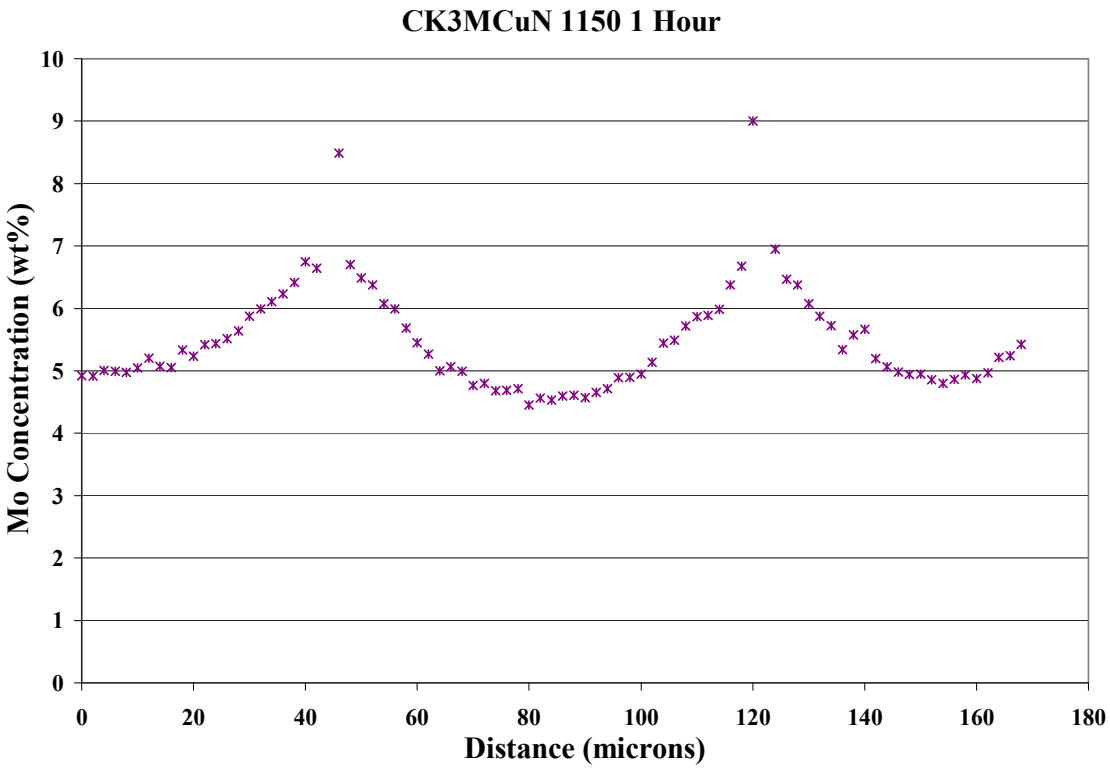

Figure 47 - Mo Concentration as a function of distance in CK3MCuN heat treated at 1150°C for 1 hour.

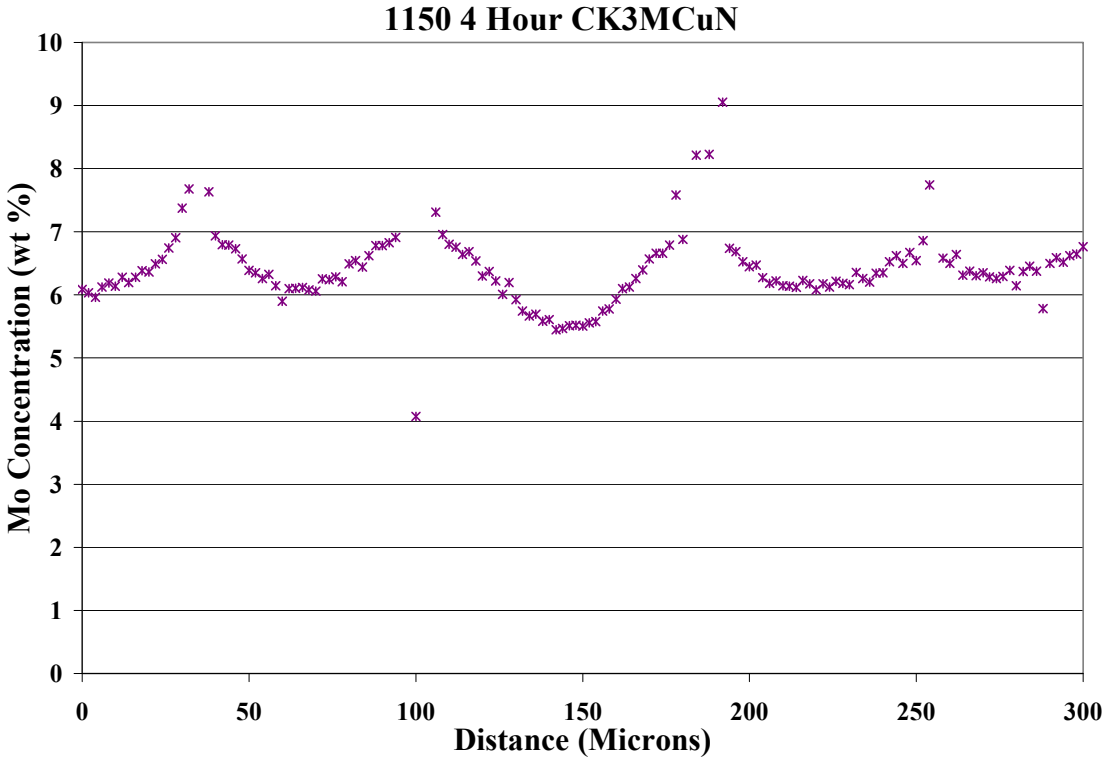

Figure 48 - Mo Concentration as a function of distance in CK3MCuN heat treated at 1150°C for 4 hours.

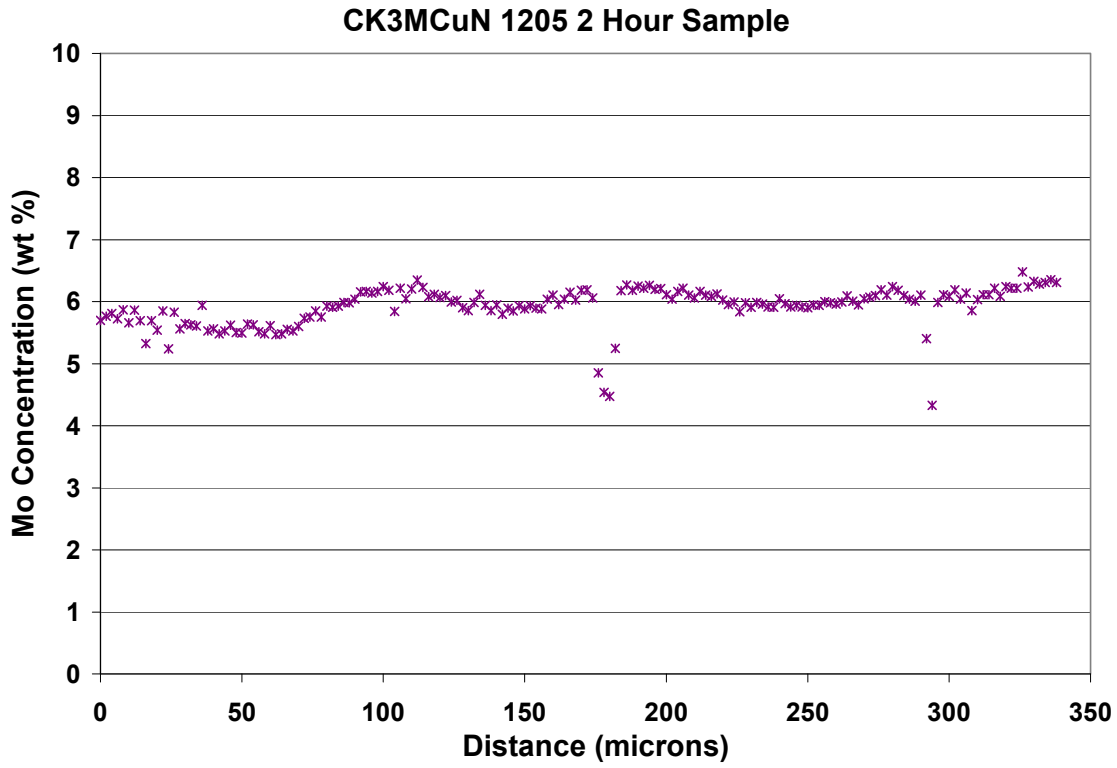

Figure 49 - Mo Concentration as a function of distance in CK3MCuN heat treated at 1205°C for 2 hours.

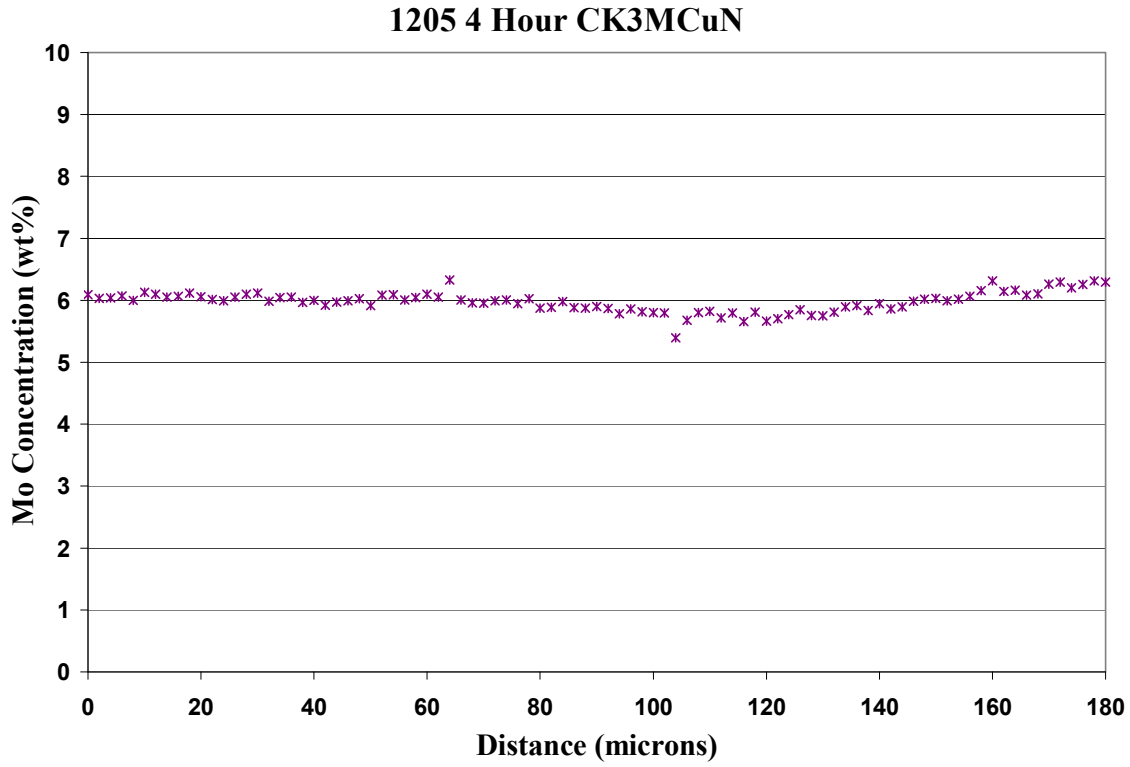

Figure 50 - Mo Concentration as a function of distance in CK3MCuN heat treated at 1205°C for 4 hours.

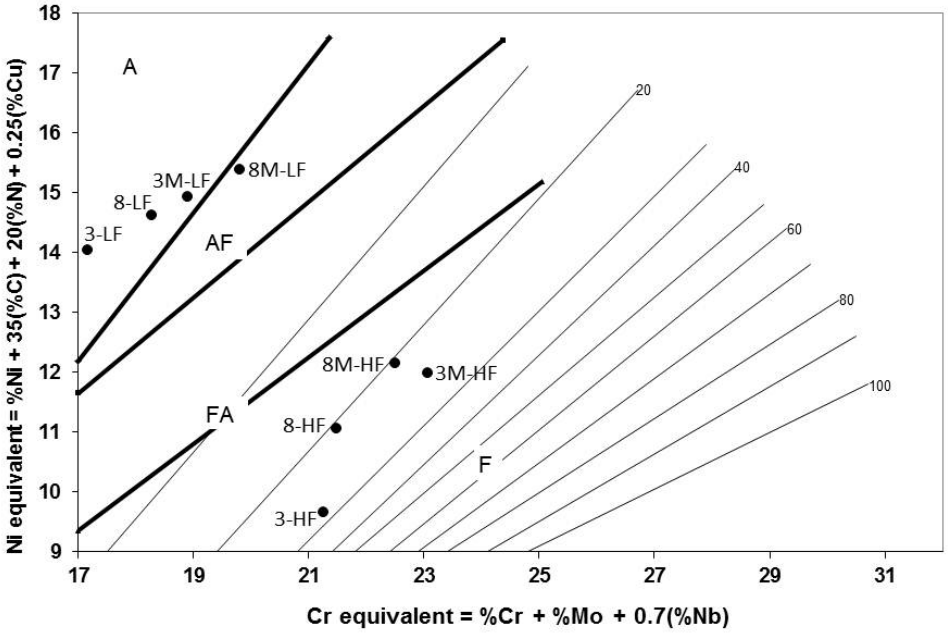

Figure 51 - WRC 1992 diagram with compositions input for cast stainless steel specimens

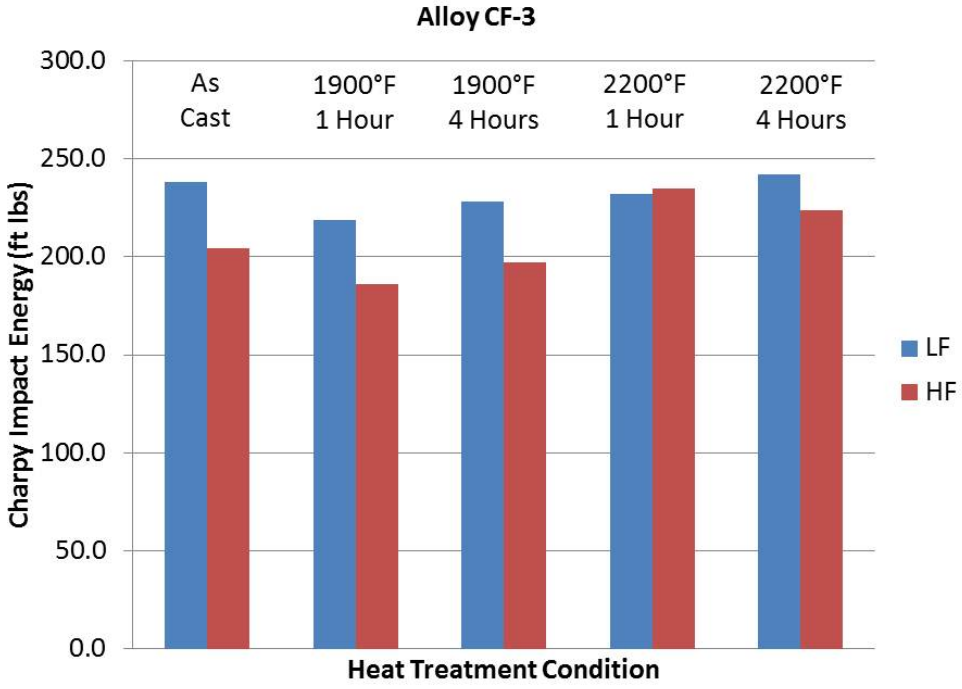

Figure 52 - Charpy impact energy for CF-3 alloy for both low and high ferrite in as cast and heat treated conditions

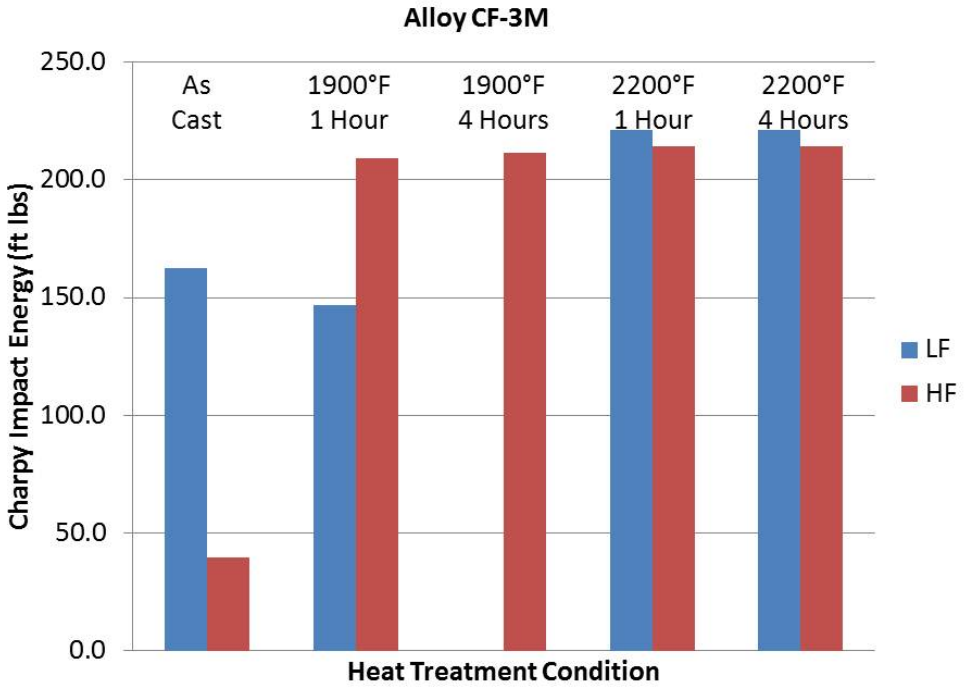

Figure 53 - Charpy impact energy for CF-3M alloy for both low and high ferrite in as cast and heat treated conditions

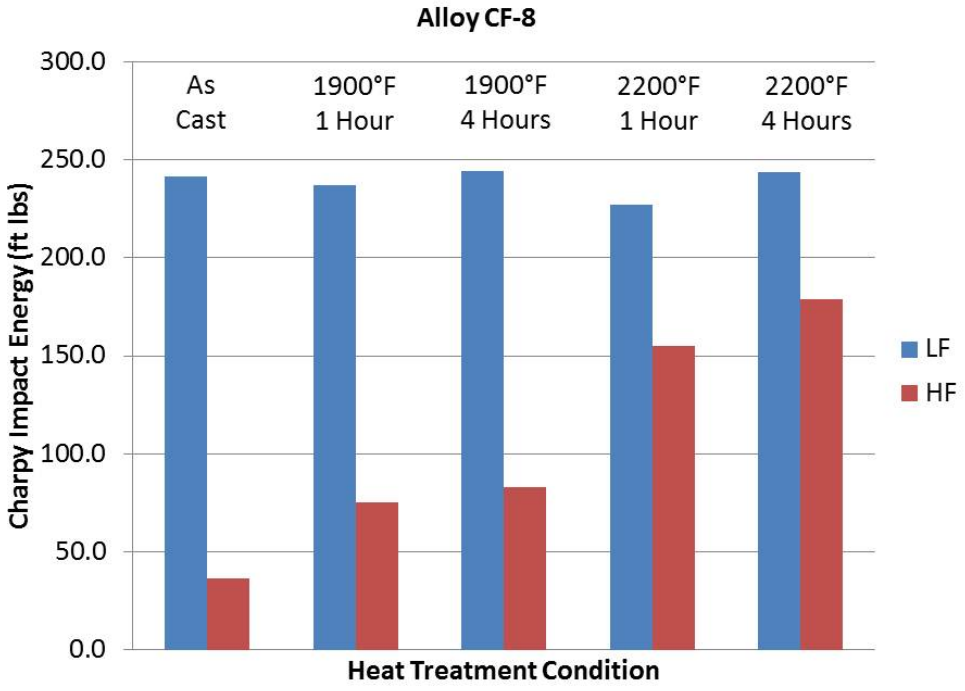

Figure 54 - Charpy impact energy for CF-8 alloy for both low and high ferrite in as cast and heat treated conditions

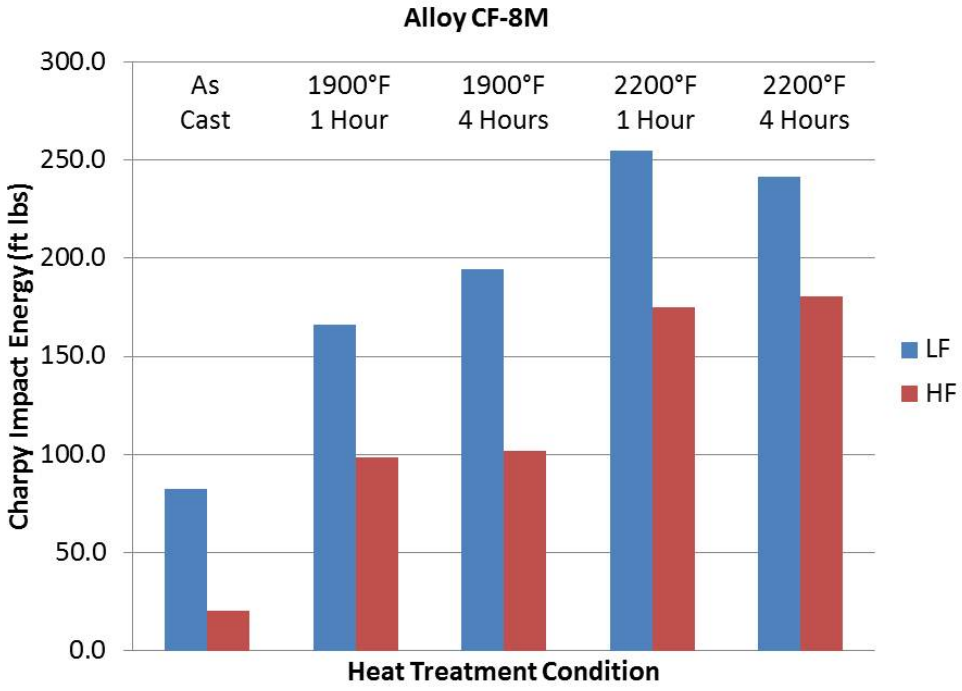

Figure 55 - Charpy impact energy for CF-8M alloy for both low and high ferrite in as cast and heat treated conditions

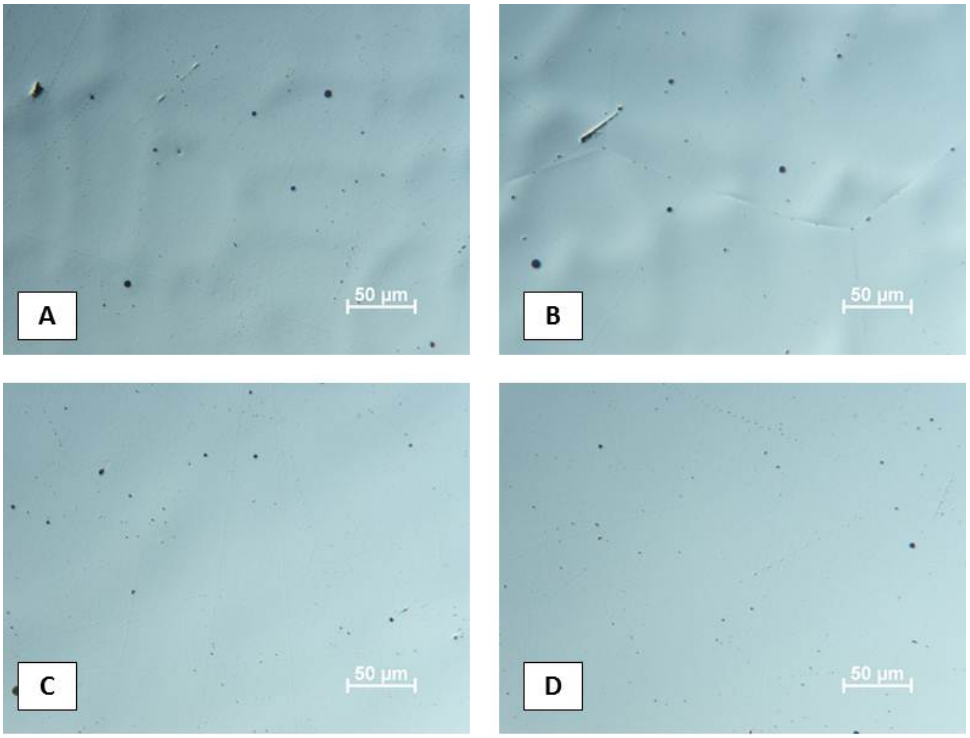

Figure 56 - Light optical photomicrographs of CF-3-LF alloy in (a) as cast condition, and heat treated for (b) 1900°F for 1 hour, (c) 2200°F for 1 hour, (d) 2200°F for 4 hours

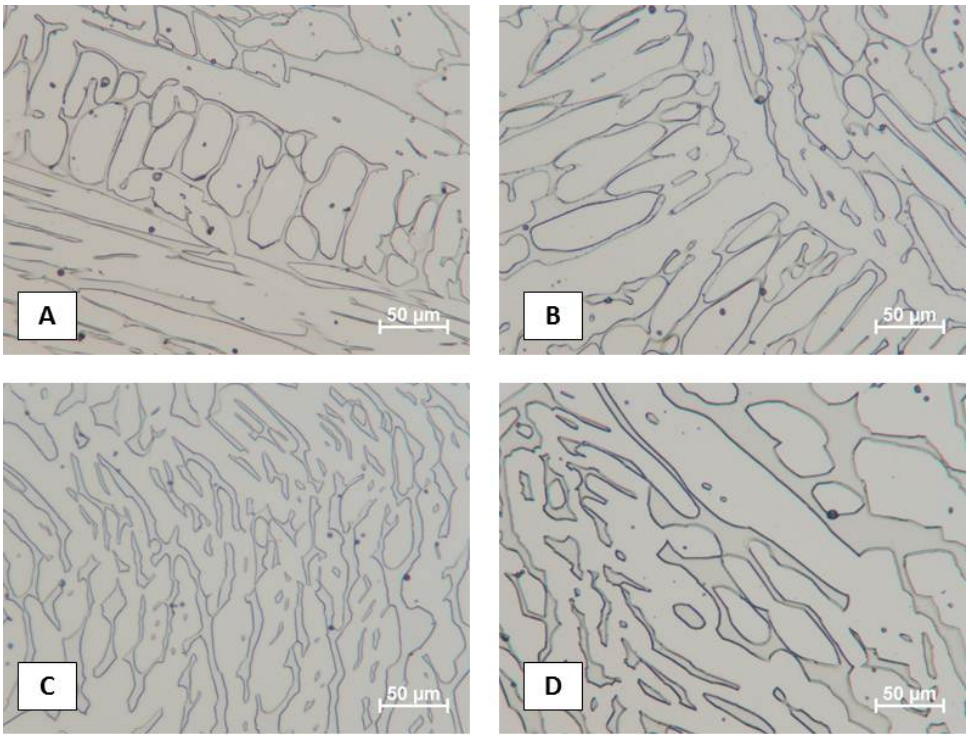

Figure 57 - Light optical photomicrographs of CF-3-HF alloy in (a) as cast condition, and heat treated for (b) 1900°F for 1 hour, (c) 2200°F for 1 hour, (d) 2200°F for 4 hours

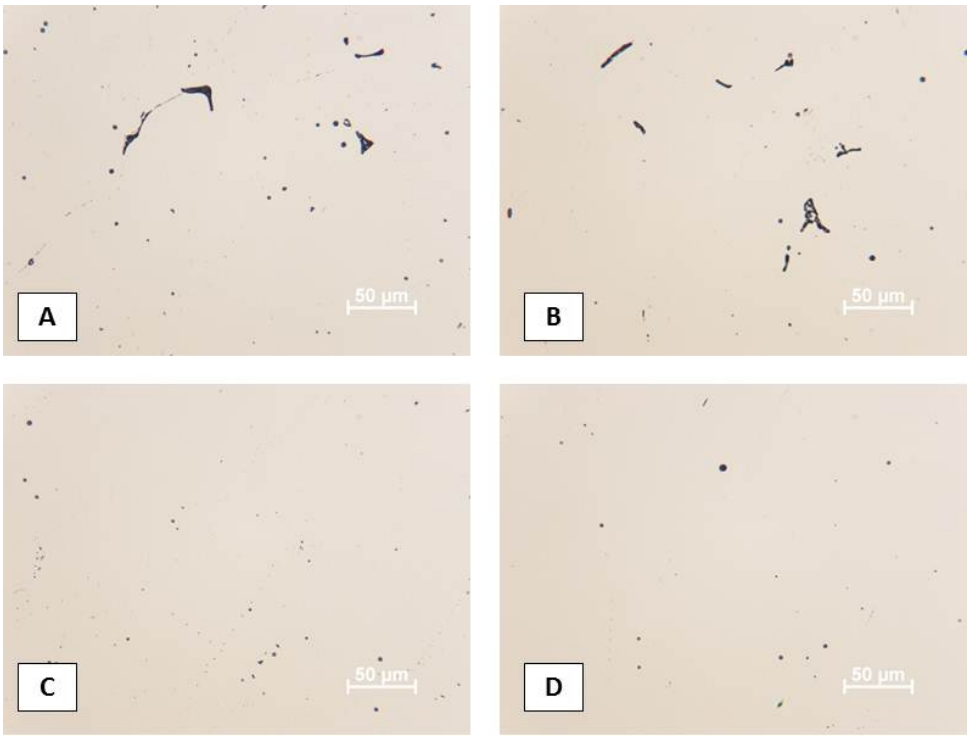

Figure 58 - Light optical photomicrographs of CF-3M-LF alloy in (a) as cast condition, and heat treated for (b) 1900°F for 4 hours, (c) 2200°F for 1 hour, (d) 2200°F for 4 hours

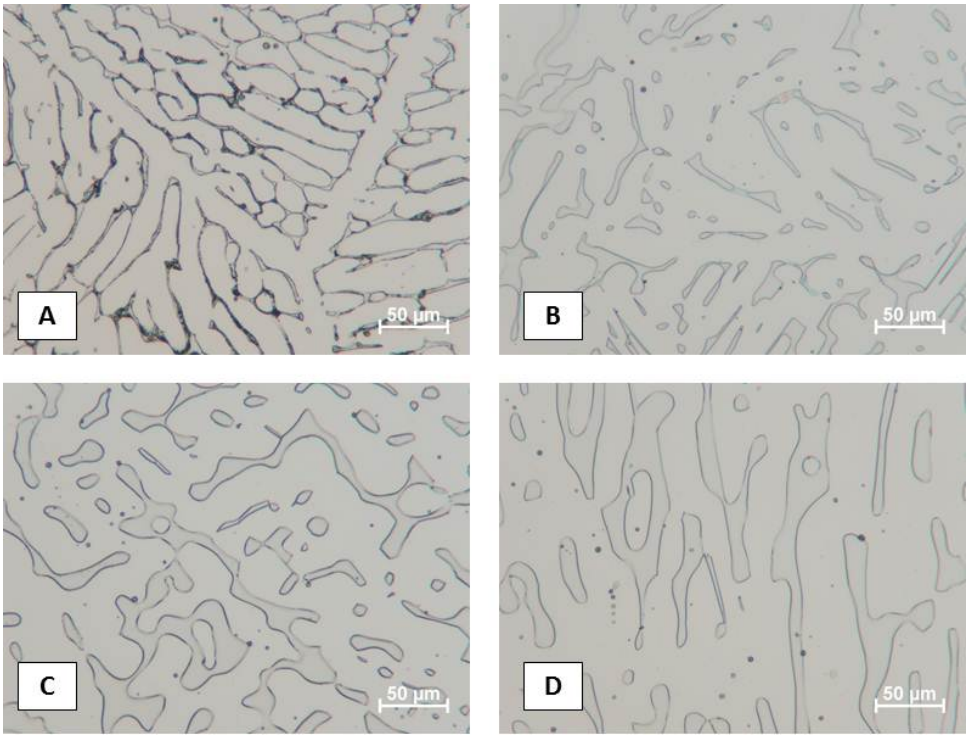

Figure 59 - Light optical photomicrographs of CF-3M-HF alloy in (a) as cast condition, and heat treated for (b) 1900°F for 4 hours, (c) 2200°F for 1 hour, (d) 2200°F for 4 hours

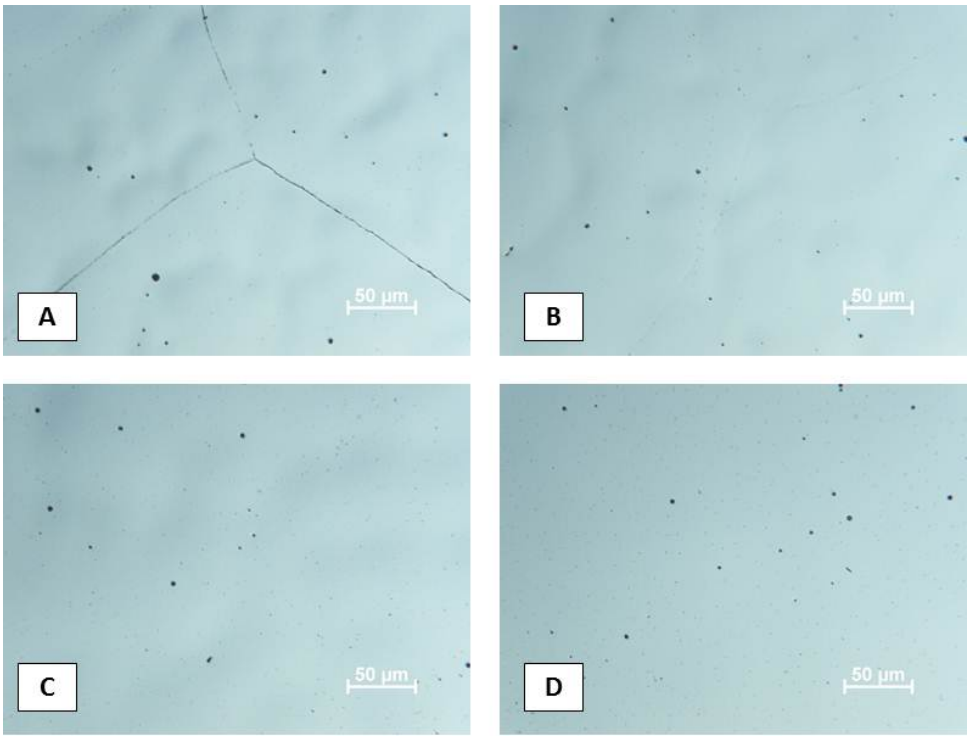

Figure 60 - Light optical photomicrographs of CF-8-LF alloy in (a) as cast condition, and heat treated for (b) 1900°F for 1 hour, (c) 2200°F for 1 hour, (d) 2200°F for 4 hours

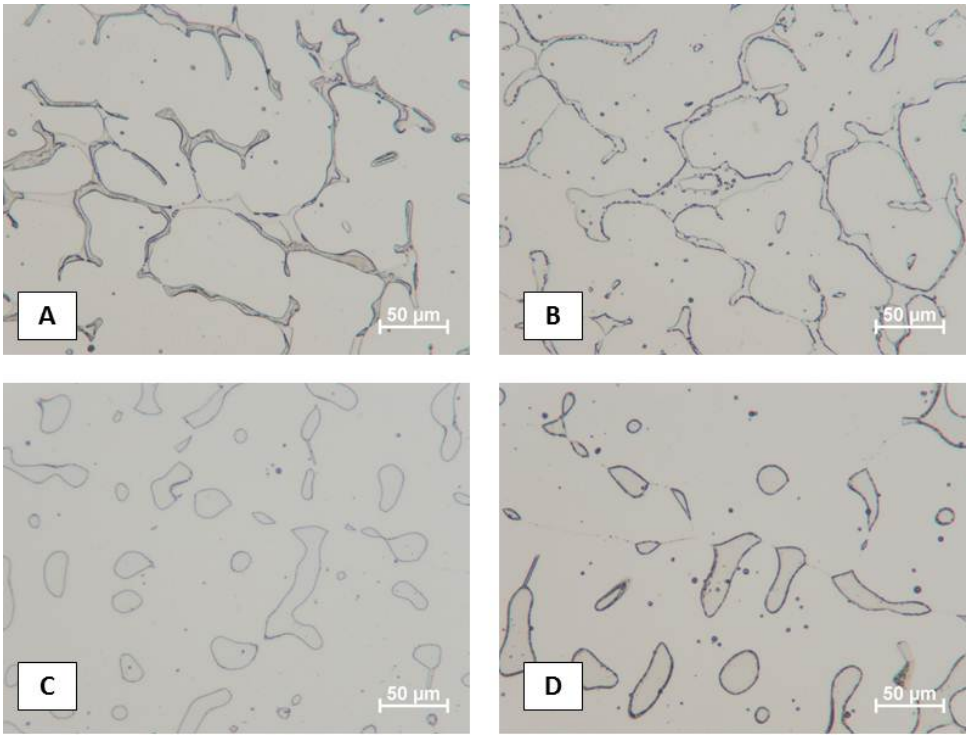

Figure 61 - Light optical photomicrographs of CF-8-HF alloy in (a) as cast condition, and heat treated for (b) 1900°F for 1 hour, (c) 2200°F for 1 hour, (d) 2200°F for 4 hours

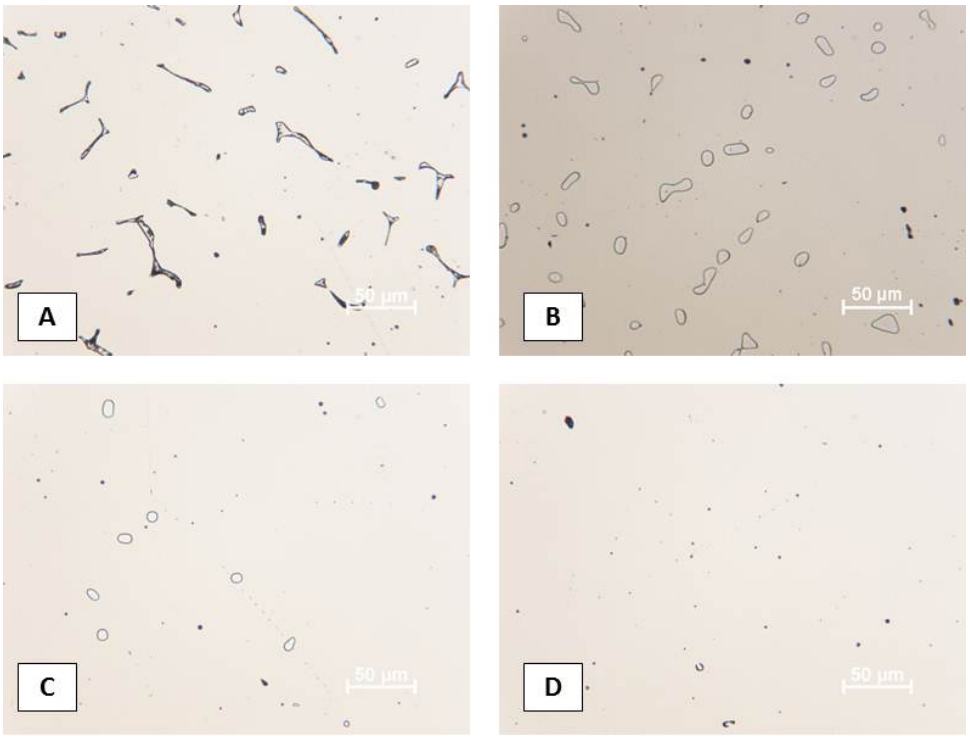

Figure 62 - Light optical photomicrographs of CF-8M-LF alloy in (a) as cast condition, and heat treated for (b) 1900°F for 4 hours, (c) 2200°F for 1 hour, (d) 2200°F for 4 hours

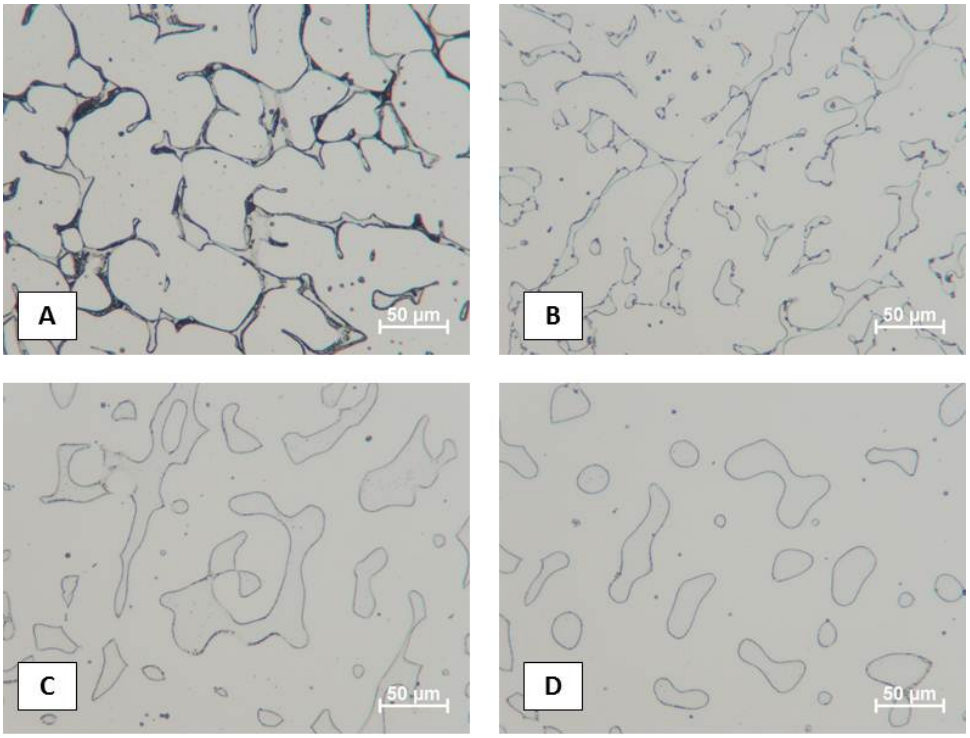

Figure 63 - Light optical photomicrographs of CF-8M-HF alloy in (a) as cast condition, and heat treated for (b) 1900°F for 4 hours, (c) 2200°F for 1 hour, (d) 2200°F for 4 hours

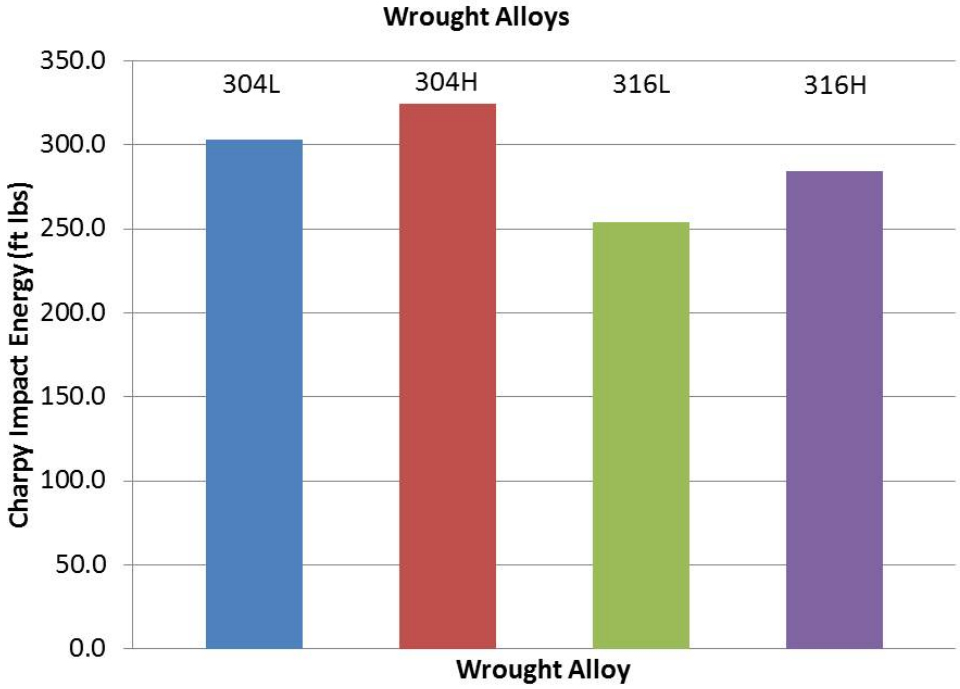

Figure 64 - Charpy impact energy for four wrought stainless steel counterparts

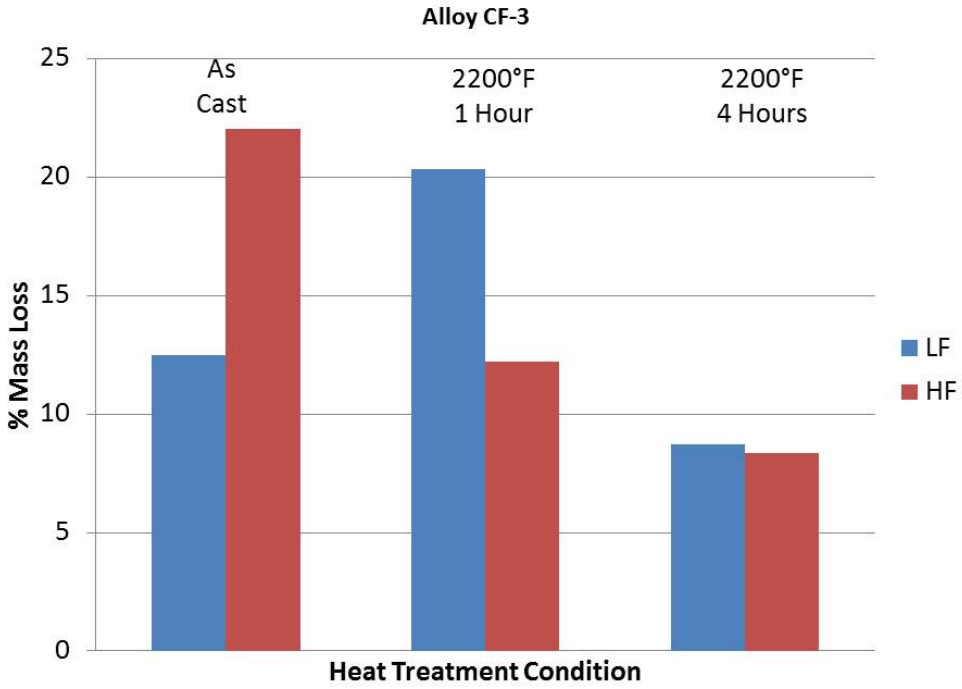

Figure 65 - Corrosion results for CF-3 alloy with both low and high ferrite in the as cast and heat treated conditions

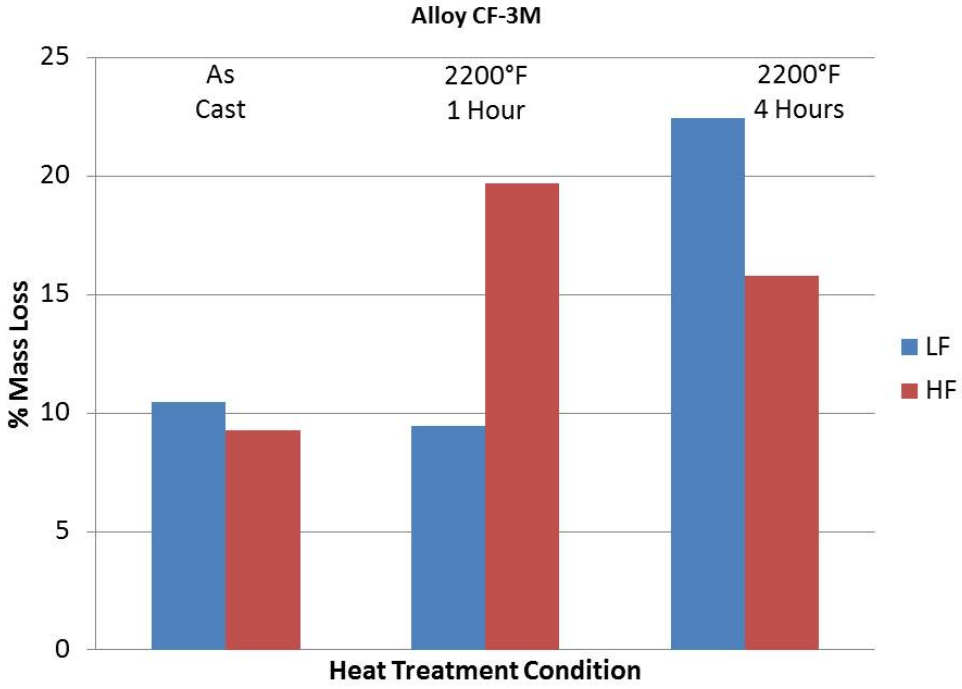

Figure 66 - Corrosion results for CF-3M alloy with both low and high ferrite in the as cast and heat treated conditions

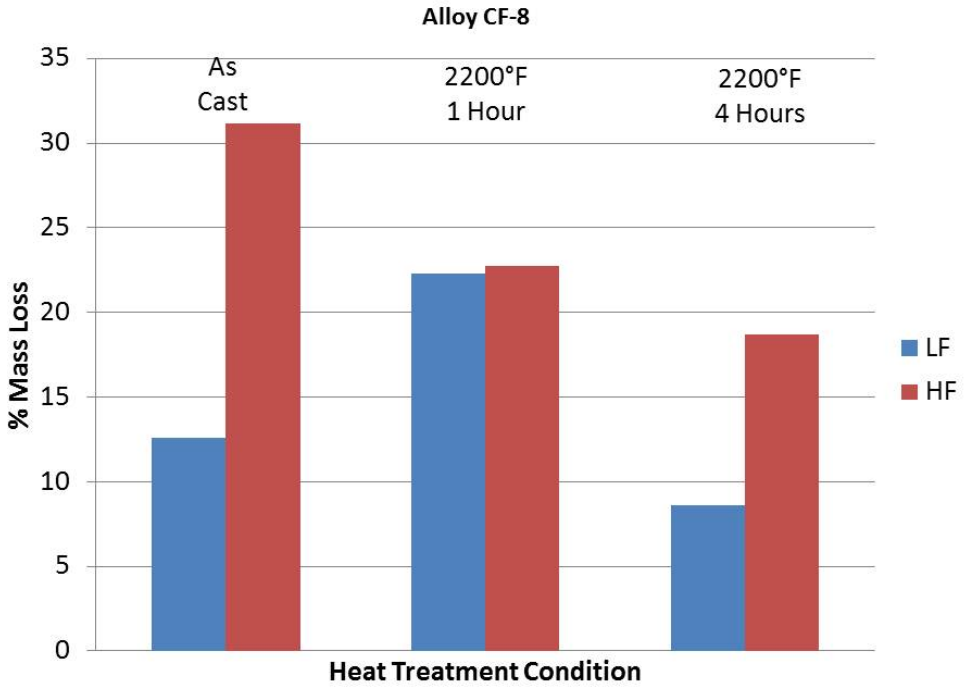

Figure 67 - Corrosion results for CF-8 alloy with both low and high ferrite in the as cast and heat treated conditions

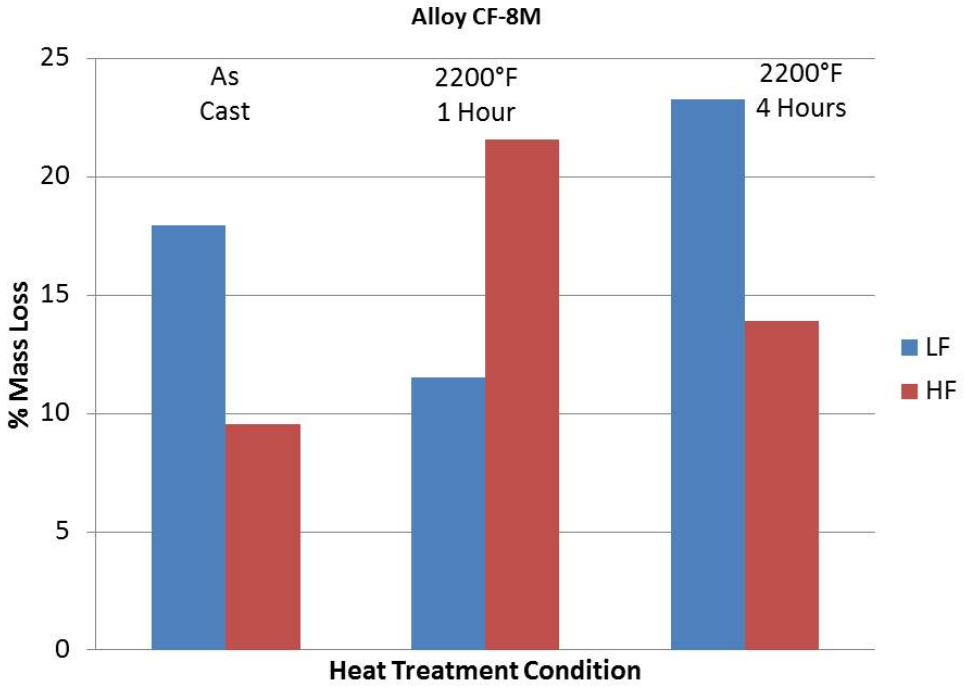

Figure 68 - Corrosion results for CF-8M alloy with both low and high ferrite in the as cast and heat treated conditions

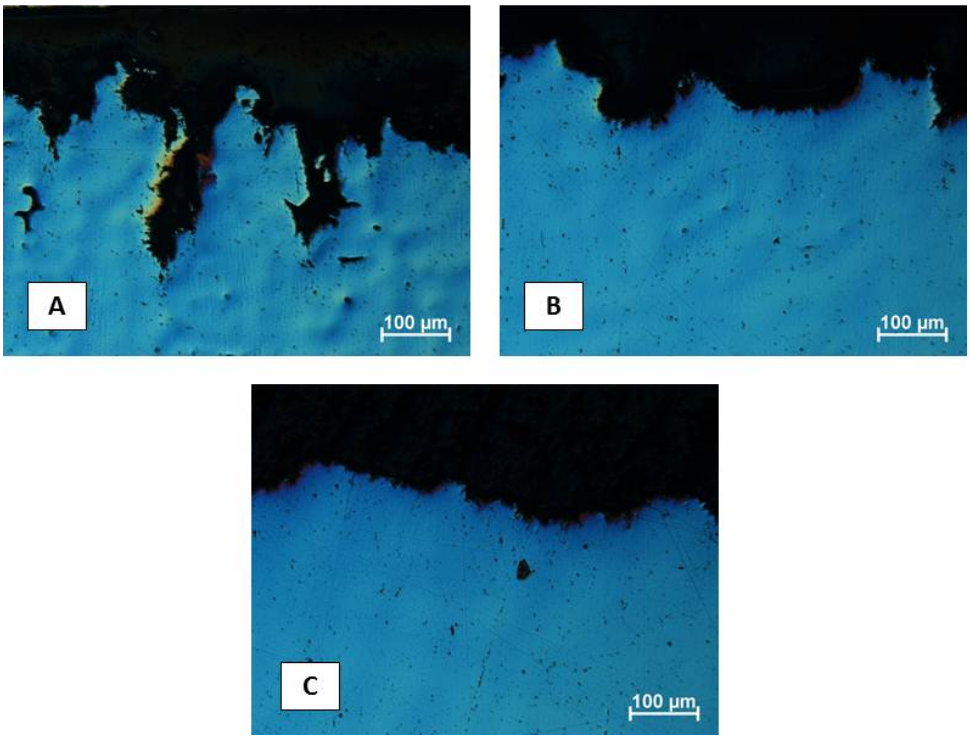

Figure 69 - Light optical photomicrographs of CF-8-LF alloy corrosion samples in (a) as cast condition and heat treated at (b) 2200°F for 1 hour and (c) 2200°F for 4 hours

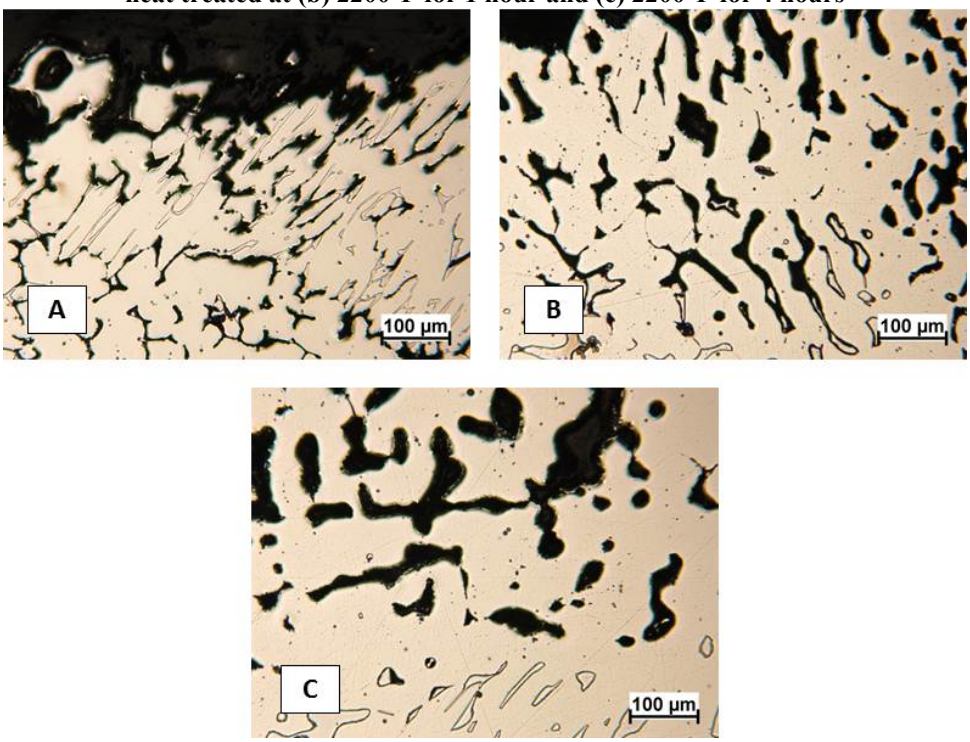

Figure 70 - Light optical photomicrographs of CF-8-HF alloy corrosion samples in (a) as cast condition and heat treated at (b) 2200°F for 1 hour and (c) 2200°F for 4 hours

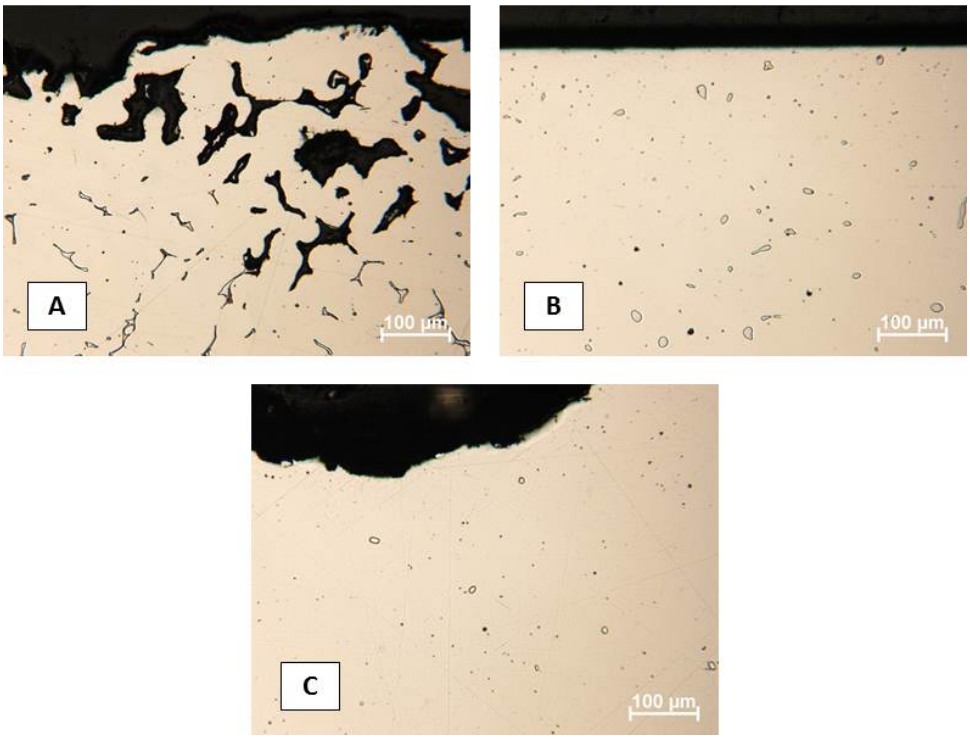

Figure 71 - Light optical photomicrographs of CF-8M-LF alloy corrosion samples in (a) as cast condition and heat treated at (b) 2200°F for 1 hour and (c) 2200°F for 4 hours

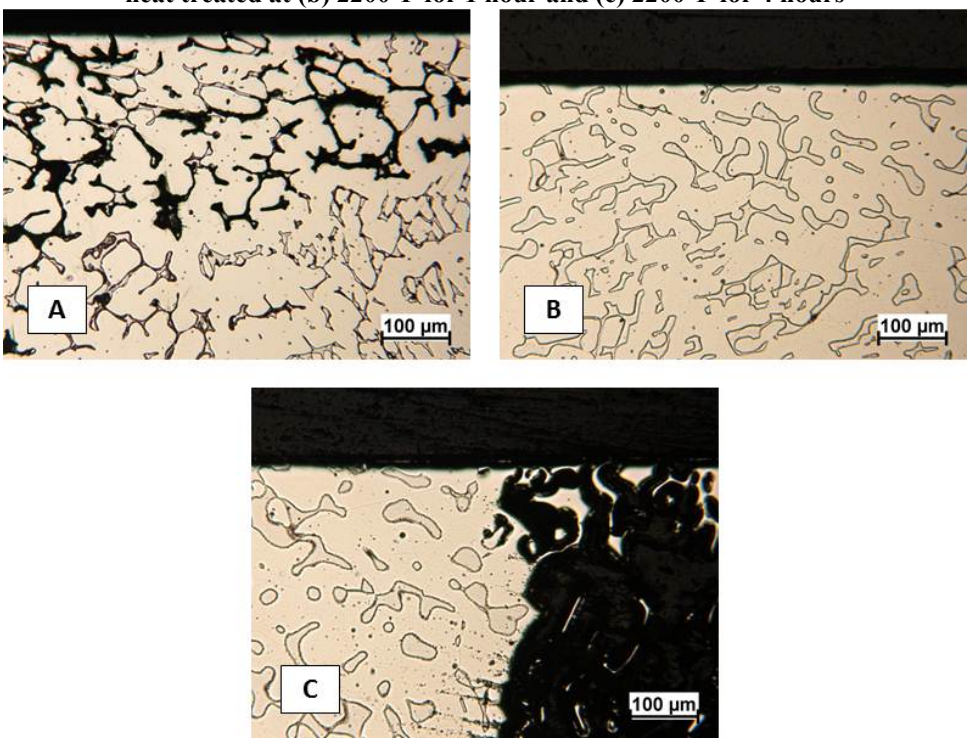

Figure 72 - Light optical photomicrographs of CF-8M-HF alloy corrosion samples in (a) as cast condition and heat treated at (b) 2200°F for 1 hour and (c) 2200°F for 4 hours

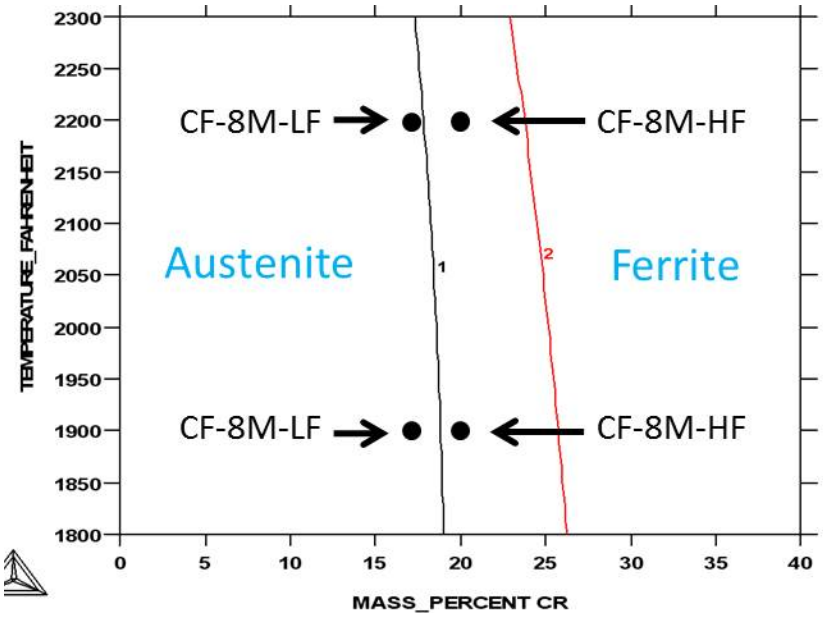

Figure 73 - High temperature region of a phase diagram computed in ThermoCalc showing austenite and ferrite phase fields with increasing Chromium concentration

References

[1] Halada, G.P. and Kim, D. (1996). Influence of nitrogen on electrochemical passivation of high-nickel stainless steels and thin molybdenum-nickel films. Corrosion 36-46.

[2] Brigham, R.J. (1974). Pitting and Crevice Corrosion of 18% Cr Stainless Steel. Materials Performance 29-31

[3] Garner, A. (1985). How Stainless Steel Welds Corrode. Met. Prog. 31

[4] Banovic, S. W., DuPont, J. N. and Marder, A. R. (2002). Dilution and microsegregation in dissimilar metal welds between super austenitic stainless steel and nickel base alloys. Science and Technology of Welding and Joining 374-383.

[5] Adams, K.D., DuPont, J.N., Marder, A.R. (2007). The Influence of Centerline Sigma (σ) Phase on the Through-Thickness Toughness and Tensile Properties of Alloy AL-6XN. Journal of Materials Engineering and Performance. 123-130

[6] Hulquist, G. and Leygraf, C. (1980). Thermal passivation of AISI 316 stainless steel in controlled vacuum. Journal of Vacuum Science and Technology 85-88.

[7] Oldfield, J. W., Lee, T. S., and Kain, R. M. The Role of Oxygen Reduction and Hydrogen Evolution in Crevice Corrosion of Stainless Steels. 89-105. 1987. Corrosion Chemistry Within Pits, Crevices, and Cracks. 10-1-1984.
Ref Type: Conference Proceeding

[8] Oldfield, J. W., Lee, T. S., and Kain, R. M. Avoiding crevice corrosion of stainless steels. 1985. Stainless Steels '84 [Eighty-Four], Proc. Conf.
Ref Type: Conference Proceeding

[9] Kain, R. M. (1979). Crevice Corrosion Resistance of Austenitic Stainless Steels in Ambient and Elevated Temperature Seawater. Corrosion 230-1-230-18.

[10] Clerbois, L., Heitz, E., Ijsseling, F. P., Rowlands, J. C. and Simpson, J. P. (1985). Principles for scaling of corrosion tests. Report prepared by the European Federation of Corrosion Working Party on \"Physicochemical methods of corrosion testing - fundamentals and applications\". British Corrosion Journal 107-115.

[11] Lee, T. S., Kain, R. M. and Oldfield, J. W. (1984). The effect of environmental variables on crevice corrosion of stainless steels in seawater. Materials Performance 9-15.

[12] Renner, M., Heubner, U., Rockel, M. B. and Wallis, E. (1986). Temperature as a pitting and crevice corrosion criterion in the ferric chloride test. Werkstoffe und Korrosion 183-190.

[13] Scheil, E. (1942). Unbroken series of solid solutions in the binary systems of the elements. Zeitschrift fuer Metallkunde 242-246.

[14] Gulliver, G. H. Metallic Alloys.

[15] Pfann, W. G. (1952). Principles of zone-melting. Journal of Metals 747-753.

[16] Malik, M. T., Bergner, D. and Kuhl, A. (1989). Interdiffusion of Mn and Mo in Austenitic Stainless Steels. Defect and Diffusion Forum 1293-1298.

[17] Brody, H. D. and Flemings, M. C. (1966). Solute redistribution in dendritic solidification. Transactions of the Metallurgical Society of AIME 615-624.

[18] Flemings, M. C. (1974). Solidification Processing. McGraw Hill Inc. 35.

[19] Susan, D. F., Robino, C. V., Minicozzi, M. J. and DuPont, J. N. (2006). A solidification diagram for Ni-Cr-Mo-Gd alloys estimated by quantitative microstructural characterization and thermal analysis. Metallurgical and Materials Transactions A: Physical Metallurgy and Materials Science 2817-2825.

[20] Perricone, M. J. and DuPont, J. N. (2006). Effect of composition on the solidification behavior of several Ni-Cr-Mo and Fe-Ni-Cr-Mo alloys. Metallurgical and Materials Transactions A: Physical Metallurgy and Materials Science 1267-1280.

[21] Saunders, N. Fe-Data Thermodynamic Database [3.0]. The Surrey Research Park . 2001. Ref Type: Computer Program

[22] Lundin, C, Wen, S, Liu, W, and Zhou, G. Systematic Microstructural and Corrosion Performance Evaluation of CK3MCuN and CN3MN High Molybdenum Stainless Steel Castings. Blair, Malcolm. A95. 2002. Steel Founder's Society of America.
Ref Type: Report

[23] Kattamis, T. Z. and Flemings, M. C. (1965). Dendrite morphology, microsegregation, and homogenization of low-alloy steel. Transactions of the American Institute of Mining, Metallurgical and Petroleum Engineers 992-999.

[24] Merz, G. D., Kattamis, T. Z. and Giamei, A. F. (1979). Microsegregation and homogenization of nickel-7.5 wt. % aluminum-2.0 wt. % tantalum dendritic monocrystals. Journal of Materials Science 663-670.

[25] Semiatin, S. L., Kramb, R. C., Turner, R. E., Zhang, F. and Antony, M. M. (2004). Analysis of the homogenization of a nickel-base superalloy. Scripta Materialia 491-495.

[26] Singh, S. N. and Flemings, M. C. (1969). Solution kinetics of a cast and wrought high strength aluminum alloy. Transactions of the American Institute of Mining, Metallurgical and Petroleum Engineers 1803-1809.

[27] Elmer, J. W., Allen, S. M. and Eagar, T. W. (1989). Microstructural development during solidification of stainless steel alloys. Metallurgical Transactions A: Physical Metallurgy and Materials Science 2117-2131.

[28] Carlson, K. D., Ou, S., Hardin, R. A. and Beckermann, C. (2002). Development of new feeding-distance rules using casting simulation: Part I. Methodology. Metallurgical and Materials Transactions B: Process Metallurgy and Materials Processing Science 731-740.

[29] Wright, S. I. (2000) Fundamentals of Automated EBSD. In: Electron Backscatter Diffraction in Materials Science (Schwartz, A. J., Kumar, M. and Adams, B. L., eds.), pp. 51-64. Kluer Academic / Plenum Publishers.

[30] Goldstein, J. I., Newbury, D. E., Echlin, P., Joy, D. C., Fiori, C. and Lifshin, E. (1981) Scanning Electron Microscopy and X-Ray Microanalysis.

[31] Sinder, M. and Pelleg, J. (2000). On homogenization of a binary alloy after dissolution of planar and spherical precipitates. Metallurgical and Materials Transactions A: Physical Metallurgy and Materials Science 1525-1530.

[32] Kim, S.H., Moon, H.K., Kang, T., Lee, C.S., (2003). Dissolution Kinetics of Delta Ferrite in AISI 304 Stainless Steel Produced By Strip Casting Process. Materials Science and Engineering A 390-398

[33] Sedriks, A.J., (1996). Corrosion of Stainless Steels. John Wiley & Sons.